Alisson Steffli Thill

Tuning the electronic and structural properties of cerium oxide nanoparticles for the H_2 production photocatalytic reaction

UFRGS
UNIVERSIDADE FEDERAL
DO RIO GRANDE DO SUL

Porto Alegre, RS - Brazil
July, 2018

Alisson Steffli Thill

Controle das propriedades estruturais e eletrônicas de nanopartículas de óxido de cério para a reação fotocatalítica de produção de H_2

Dissertação realizada sob a orientação do Prof. Fabiano Bernardi e coorientação do Prof. Sérgio Ribeiro Teixeira e apresentada ao Instituto de Física da UFRGS, em preenchimento parcial dos requisitos para a obtenção do título de Mestre em Física.

Universidade Federal do Rio Grande do Sul – UFRGS
Instituto de Física
Programa de Pós-Graduação

Orientador: Prof. Dr. Fabiano Bernardi
Coorientador: Prof. Dr. Sérgio Ribeiro Teixeira

Porto Alegre, RS - Brasil
Julho de 2018

Acknowledgements

I wish to acknowledge my parents, Gelson and Lisete, who never stopped encouraging, supporting and investing in my formation, being always by my side and helping when I needed them most.

To my girlfriend, Catiane, who played a vital role helping in completing this stage of my life through her encouragement, support, love and patience.

To my aunt, Susana, who spared no effort to help me when I needed it.

To Prof. Fabiano Bernardi for its guidance, patience and for contributing immensely to my learning through his teachings and corrections.

To Prof. Sérgio Teixeira for its cosupervision.

To Prof. Fernanda Poletto and Francielli Lobato from IQ-UFRGS for synthesizing the samples used in this work.

To Prof. Edmar Soares from UFMG for collaborating with the XPS and UPS measurements presented in this work.

To Maurício Vaz for collaborating with the H_2 evolution photocatalytic activity measurements.

To my friends and colleagues that contribute to my knowledge through rich discussions.

And also to all who have contributed in some way to my formation, I leave my sincere and deep thanks.

Moreover, I thank to LNLS for providing access to the Brazilian Synchrotron in order to perform the X-ray absorption measurements presented in this work.

To CNANO for providing the XRD measurements presented in this work.

To Prof. Fabiano S. Rodembusch from IQ-UFRGS for providing access to the UV-Vis spectrophotometer in order to perform the UV-Vis measurements.

To Central Analítica (IQ-UFRGS) for providing the FTIR measurements presented in this work.

To CESUP-UFRGS for providing access to its high-performance computing environment, where the DFT calculations presented in this work were run.

And to CNPq for the Master fellowship that helped to become this work possible.

"To explain all nature is too difficult a task for any one man or even for any one age. Tis much better to do a little with certainty & leave the rest for others that come after than to explain all things by conjecture without making sure of any thing."

- Isaac Newton

Abstract

The photocatalytic water splitting reaction showed to be a promising process to obtain renewable and clean energy, but the efficiency reached in this process is still low and must be improved to be viable. Considering this, the research on improving the efficiency of photocatalysts has attracted a strong interest in the past last years. Cerium oxide (CeO_{2-x}, $0 < x < 0.5$) is a material recently investigated as a possible photocatalyst to obtain H_2 from H_2O. In this work, cerium oxide nanoparticles with high surface area ($104 < S_{BET} < 201$ m^2/g), high pore volume ($32 < V < 132$ mm^3/g) values, wide range of diameter ($2 < d < 90$ nm) and O vacancies population ($0.05 < x < 0.46$) were applied to the H_2 production photocatalytic reaction. The nanoparticles presented activity of up to 10 times higher than the commercial cerium oxide standard. UV-Vis, X-ray Diffraction, X-ray Absorption Spectroscopy, X-ray Photoelectron Spectroscopy, Ultraviolet Photoelectron Spectroscopy and Fourier Transform Infrared measurements were performed aiming to elucidate these results and to determine the main structural and electronic properties that can improve the H_2 production photocatalytic reaction. It was obtained that the band gap energy depends on the nanoparticle synthesized and can be as low as 2.73 eV. The Ce 4f orbital occupation and the structural disorder presented by the nanoparticles is directly related with the band gap energies obtained. Density Functional Theory (DFT) calculations were performed to obtain the relation between the band structure (DOS) and the O vacancy population in order to explain the dependence of the band gap energy with the Ce 4f orbital occupation. Moreover, the O vacancies population at the surface have a very different effect depending on the presence or absence of mesopores, where a lower O vacancy population at the surface is better (worse) to the photocatalytic activity in the presence (absence) of mesopores. Furthermore O vacancies population at the surface plays a more fundamental role on the photocatalytic activity than the band gap energies for the samples presenting mesopores. The results allowed shedding light on the improvement of the properties of cerium oxide nanoparticles applied to optimize the H_2 production photocatalytic activity.

Key-words: H_2 production, cerium oxide, DFT, XAS, XPS, UPS, UV-Vis, Rietveld.

Resumo

A reação fotocatalítica de separação da água mostrou-se um processo promissor para obter energia limpa e renovável, porém a eficiência alcançada nesse processo ainda é baixa e precisa ser melhorada para se tornar viável. Considerando isso, estudos sobre a melhoria da eficiência dos fotocatalisadores tem atraído forte interesse dos pesquisadores nos últimos anos. O óxido de cério (CeO_{2-x}, $0 < x < 0{,}5$) é um material recentemente investigado como possível fotocatalisador para obter H_2 a partir da H_2O. Neste trabalho, nanopartículas de óxido de cério com alta área superficial ($104 < S_{BET} < 201$ m^2/g), altos valores de volume de poro ($32 < V < 132$ mm^3/g) e amplo intervalo de diâmetro ($2 < d < 90$ nm) e população de vacâncias de O ($0{,}05 < x < 0{,}46$) foram aplicadas na reação fotocatalítica de produção de H_2. As nanopartículas apresentaram atividades até 10 vezes maiores do que o padrão comercial de óxido de cério. Medidas de UV-Vis, difração de raios x (XDR), espectroscopia de absorção de raios x (XAS), espectroscopia de fotoelétrons excitados por raios x (XPS), espectroscopia de fotoelétrons excitados por ultravioleta (UPS) e infravermelho com transformada de Fourier (FTIR) foram realizadas com o objetivo de elucidar esses resultados e determinar as principais propriedades estruturais e eletrônicas que melhoram a reação fotocatalítica de produção de H_2. É observado que o valor de energia de gap depende da nanopartícula sintetizada e chega a valores pequenos, onde o menor valor encontrado é de 2,73 eV. A ocupação do orbital 4f do Ce e a desordem estrutural apresentadas pelas nanopartículas são diretamente relacionadas com os valores de energia de gap obtidos. Cálculos da teoria do funcional da densidade (DFT) foram realizados para obter a relação entre a estrutura de bandas eletrônicas (DOS) e a população de vacâncias de O com o objetivo de explicar a dependência do valor de energia de gap com a ocupação do orbital 4f do Ce. Além disso, a população de vacâncias de O na superfície tem um efeito na atividade fotocatalítica dependente da presença ou ausência de mesoporos, onde uma baixa população de vacâncias de O na superfície é melhor (pior) para a atividade fotocatalítica na presença (ausência) de mesoporos. Adicionalmente, a população de vacâncias de O na superfície desempenha um papel mais importante na atividade fotocatalítica do que os valores de energia de gap para as amostras com a presença de mesoporos. Os resultados permitiram elucidar as propriedades necessárias para otimizar a atividade fotocatalítica de produção de H_2 pelas nanopartículas de óxido de cério sintetizadas.

Palavras-chaves: produção de H_2, óxido de cério, DFT, XAS, XPS, UPS, UV-Vis, Rietveld.

Contents

List of symbols

Å	Angstrom
V vs. NHE	Volts versus Normal Hydrogen Electrode
λ	Radiation wavelength
$h\nu$	Photon energy
E_k	Kinetic energy
E_b	Binding energy
ϕ_s	Sample's work function
ϕ_a	Analyser's work function
λ_{IMFP}	Inelastic mean free path
j	Total angular momentum number
l	Orbital angular momentum number
s	Spin orbital angular momentum number
μ	Absorption coefficient
$\Delta\mu_0$	Absorption edge height
I	Intensity
k	Wavenumber
m	Electron mass
E	Energy
$\chi(k)$	EXAFS oscillations
G	Green's function
$\hat{\epsilon}$	Polarization vector
τ	Complete scattering operator
ρ	Electronic density
$E[\rho]$	Total energy functional

$\hat{E}_k$	Kinetic energy operator
$\hat{U}$	Potential energy operator
$\hat{V}$	Electron-electron interaction energy operator
ψ	Wave function
ϵ_i	Energy eigenvalue of the electron i
$E_{xc}[\rho]$	Functional that contains the exchange and correlation energies
U_{eff}	Hubbard parameter
E_g^D	Direct band gap energy
E_g^I	Indirect band gap energy
χ^2	*Chi* squared factor, indicating the quality of the fitting result
R_{wp}	Weighted profile factor, indicating the quality of the fitting result
R_{exp}	Expected weighted profile factor, indicating the quality of the fitting result
R^2	R squared factor, indicating the quality of the fitting result
Ξ	Ce(III) fraction
Ξ^{XRD}	Ce(III) fraction obtained by X-ray Diffraction analysis
Ξ^{XANES}	Ce(III) fraction obtained by X-ray Absorption Near Edge Structure analysis
Ξ^{XPS}	Ce(III) fraction obtained by X-ray Photoelectron Spectroscopy analysis
σ^2	Debye-Waller factor

1 Introduction

The world is preparing to face a major energy crisis in the next decades [1,2]. Since the world population is growing and the fossil fuels, which is the main energy source nowadays, inevitably is running out, new renewable and sustainable energy sources must be developed in order to supply the world's energy consumption in the near future. Moreover, the scientific community alerts that the use of the fossil fuels and other energy sources that liberate CO_2 to the atmosphere contributes to the increase of the greenhouse effect and, therefore, to the global warming [3]. In order to maintain the earth as a place where society can live in the future, replacement of the energy sources as fossil fuels for renewable and sustainable energy sources is mandatory and needs to be done immediately.

The energy that reaches the Earth's surface from the Sun in one hour is higher than the world's energy consumption in one year [3]. For that reason, the Sun can be seen as a great energy source. The effective conversion of this energy for society is a good alternative that can overcome the imminent energy crisis. There are many ways to utilize the solar energy. The H_2 production from the photocatalytic water splitting reaction is being studied in the last decades as a promising form to utilize the solar energy aiming to produce a renewable and sustainable fuel [4–9]. Several works can be found in the literature that investigate more efficient and economic ways to store and transport H_2 in order to become practicable in the use of this compound as a fuel [10–13]. However, the efficiency of the H_2 production from the photocatalytic water splitting reaction is still low and needs improving to be viable.

In the literature, several works can be found which investigate the structural, electronic and morphological properties of different phocatalysts, aiming to improve the efficiency of the photocatalytic water splitting reaction. The main properties which can interfere in the efficiency of this photocatalytic reaction are the electronic band gap energy, surface area, particle size, control of the structural defects and oxygen vacancy population. Among the photocatalysts studied are TiO_2 [14], $SrTiO_3$ [15], $NiTa_2O_6$ [16] and CeO_2 [17].

The cerium oxide is widely used currently in several fields of knowledge such as catalysis, fuel cells, and optics [18–21]. The main characteristic which makes it of great interest is the facility in creating and eliminating oxygen vacancies at the surface in a reversible way. Moreover, cerium oxide has attracted great attention in the last years for energy applications, like H_2 production. In a previous work [22], the possibility to tune the particle size, surface area, oxygen vacancy population and surface morphology of cerium oxide nanoparticles by changing the synthesis parameters was demonstrated. The possibility to tune these properties makes these cerium oxide nanoparticles a promising system to be applied for the H_2 production reaction. The main goal of this work is to investigate the cerium oxide nanoparticles obtained in the previous work applied to the H_2 production

photocatalytic reaction in order to determine the structural and electronic properties that improve the efficiency of this reaction.

The second chapter of this Master thesis is dedicated to present the main motivations of this work, an overview of the basis and current studies about the H_2 production from a photocatalytic reaction. The third chapter covers the physical phenomena and theoretical bases of the main methods of analysis used in this work. The fourth chapter describes the experimental and theoretical procedures and the data analysis used in each step of the work. The fifth chapter is dedicated to present and discuss the results obtained from the data analysis and theoretical calculations performed. The sixth and last chapter is dedicated to present the conclusions of the work and perspectives.

2 World Energy Demand Issue and the H_2 Production as a Promising Solution

2.1 The Importance of the Energy Renewable Sources and the Global Warming Issue

The world energy demand has rapidly increased in the last decades. From 1973 to 2015 the world total energy consumption doubled, from about 1.95×10^{20} J to about 3.9×10^{20} J [1]. The projection for the world total energy consumption in 2050, based on the current energy consumption, is alarming. Nocera [2] explains that even with extreme conservation procedures of energy consumption, the world total energy consumption in 2050 will double in comparison with the world total energy consumption of 2015. Moreover, even by considering the total amounts of possible energy sources like biomass, nuclear, wind and hydroelectrics, sustaining this quantity of energy consumption is impracticable. Currently, the energy sources most used in the world are the fossil fuels [1,3]. The major problem of this source is that it is finite and the current patterns of energy consumption and growth are not long term sustainable. It is hard to predict when the fossil fuels will be exhausted. If the lifetime of a fuel reserve, defined as the known accessible amount divided by the rate of present use decreases, the fuel price increases, then the demand falls and previously more expensive alternating energy sources enter into the market. This economic behaviour tends to make the original energy source last longer than the indication obtained by calculation considering only the accessible amount. [3]. However, the exhaustion of the fossil fuels is inevitable and, for that reason, this kind of energy source must be replaced by sustainable and renewable energy sources.

Moreover, the emissions caused by the combustion of fossil fuels worsen the negative consequences of the greenhouse effect. The greenhouse effect [3] is responsible to maintain the Earth's average surface temperature higher than the temperature of the outer atmosphere and enables the several needed conditions for the emergence and maintenance of life. This effect can be easily explained in six steps as shown in Figure 2.1.1. Some amount of the Sun's radiation reaching the Earth is reflected back into space or absorbed by the atmosphere. Another amount of Sun's radiation passes through the atmosphere reaching the Earth's surface that warms up by absorption of this radiation. Therefore, the Earth's surface heated by the Sun's radiation emits infrared radiation approximately as a black body at 250 K. Some amount of this infrared radiation is absorbed in the atmosphere by the greenhouse gases, like CH_4 and CO_2. The infrared radiation is absorbed when the electromagnetic radiation resonates with the natural mechanical vibrations of these

molecules. The absorption of the infrared radiation by the greenhouse gases present in the atmosphere, that occurs with the incoming solar radiation and with the outgoing heat radiation, increases the Earth's surface temperature. This increase in the Earth's surface temperature is called the greenhouse effect, as the comparison with a glass of an horticultural glasshouse. It works in a similar way by absorbing infrared radiation, including that is emitted from objects inside the glasshouse during the full day, and allows the rest of incoming solar radiation to be transmitted during daytime. This effect, because of the glass, maintains the temperature inside the greenhouse above the ambient temperature outside, which is the main purpose of horticultural glasshouse in middle and higher latitude countries.

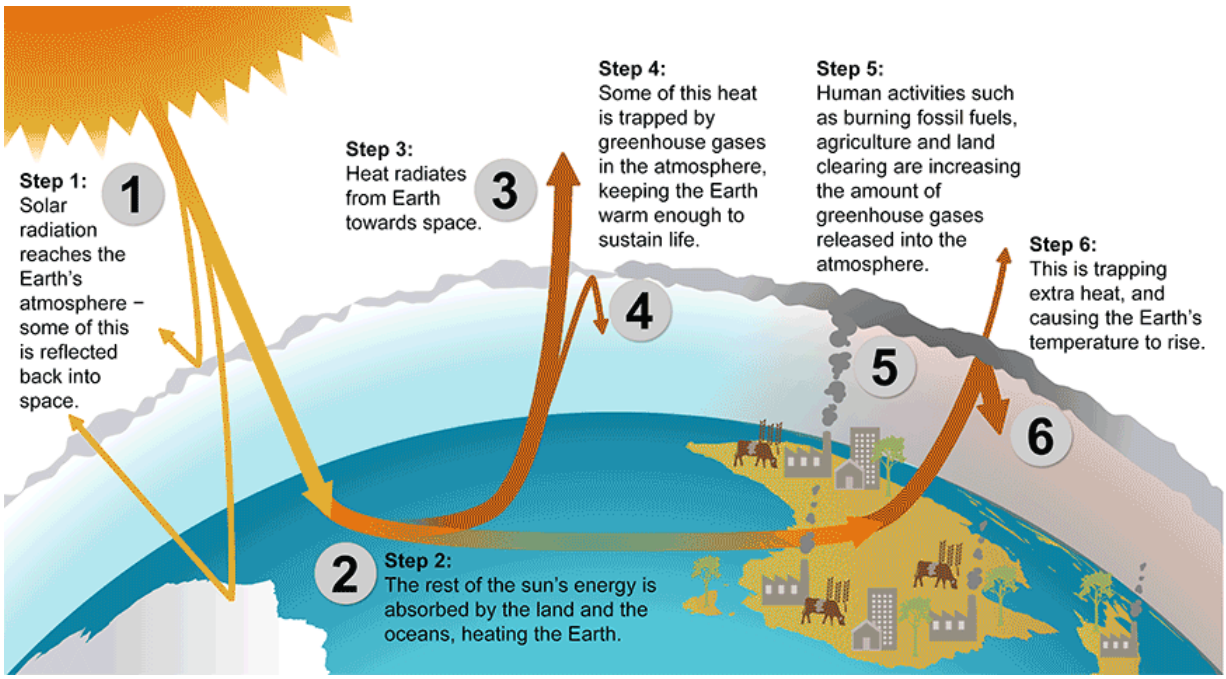

Figure 2.1.1 – Schematic representation of the greenhouse effect in six steps. Figure obtained from [23].

Measurements of the amount of gas trapped in polar ice show that the concentration of greenhouse gases in the atmosphere, mainly CO_2, has increased significantly since the Industrial Revolution in the 18^{th} century. Figure 2.1.2(a) shows the CO_2 concentration in parts per million (ppm) since the beginning of Industrial Revolution. The more recent information about this concentration shown in Figure 2.1.2(a) is obtained from direct measurements at stations such as Mauna Loa in Hawaii and Cape Grim in Tasmania [3]. It is possible to observe that the global average atmospheric concentration of CO_2 increased from 280 ppm in 1800 to 380 ppm in 2005 and is still increasing. This increase in the atmospheric concentration of CO_2 makes the greenhouse effect more intense, absorbing more infrared radiation, therefore, causing an increase in the temperature on the Earth's surface, that is known as global warming. Figure 2.1.2(b) presents the global average temperature anomaly as a function of the year since 1850. The temperature anomaly is the

difference between the average temperature in a determined year and the average temperature recorded in the period from 1961 to 1990. It is possible to observe that in the last decades the global average temperature has increased showing that the global warming is indeed occurring. The global warming is undesirable as it induces a climate change, which affects, for example, the *El Niño* phenomenon in an unpredictable way [24], threatens life in the Arctic lakes [25] and changes the precipitation frequency and intensity [26] that can affect agriculture. Figure 2.1.2(c) presents the rapidly decrease on the extension of Arctic sea ice in the last decades due to the climate change caused by the increase of the global average temperature. Moreover, the increase of the CO_2 concentration in the atmosphere also causes the acidification of the oceans. The oceans have absorbed part of the emitted CO_2 molecules since the 18^{th} century. This natural process reduced the greenhouse gas levels in the atmosphere and decreased some of the negative impacts of global warming since the Industrial Revolution. However, the absorption of CO_2 molecules by the oceans has a significant impact in the chemistry of the seawater causing the oceans to become 26 % more acid. If this acidification process continues, it could affect fundamental biological and chemical processes of the oceans in the next decades [27]. In other words, a climate change can bring dangerous consequences for ecosystems, food and health of the world's population.

Presently, the scientific community agrees that the recent increases in the CO_2 and CH_4 concentrations in the atmosphere and in the temperature are due to human activity. One way to conclude that the increase in the CO_2 concentration is due to human activity is by monitoring the C^{13}/C^{12} concentration ratio, where C^{13} and C^{12} are the two stable carbon isotopes. Since the beginning of the Earth, atmospheric CO_2 has been formed from the combustion of plant material in biomass, fossil fuels, from volcanic and other emissions from the subterranean. Plants preferentially absorb C^{12}, so the C^{13}/C^{12} ratio is reduced in plants and therefore in fossil fuels, if compared with the C^{13}/C^{12} ratio in the atmosphere. In volcanic and other emissions from subterranean Earth there is no preferential increase in the proportion of the C^{12} and therefore no change in the C^{13}/C^{12} ratio in the atmosphere is expected. However, measurements show that the C^{13}/C^{12} ratio in the atmosphere has been decreasing, showing that the additional C^{12} comes from the fossil fuels combustion and forest burning [3]. A similar analysis of carbon isotopes is used to study CH_4 emissions into the atmosphere from biological and fossil sources. Therefore, aiming to stabilize the greenhouse gases concentration in the atmosphere at a level that would prevent and mitigate dangerous anthropogenic climate changes, scientists have been concerned in the last decades to develop sustainable and renewable energy sources that do not emit greenhouse gases [28].

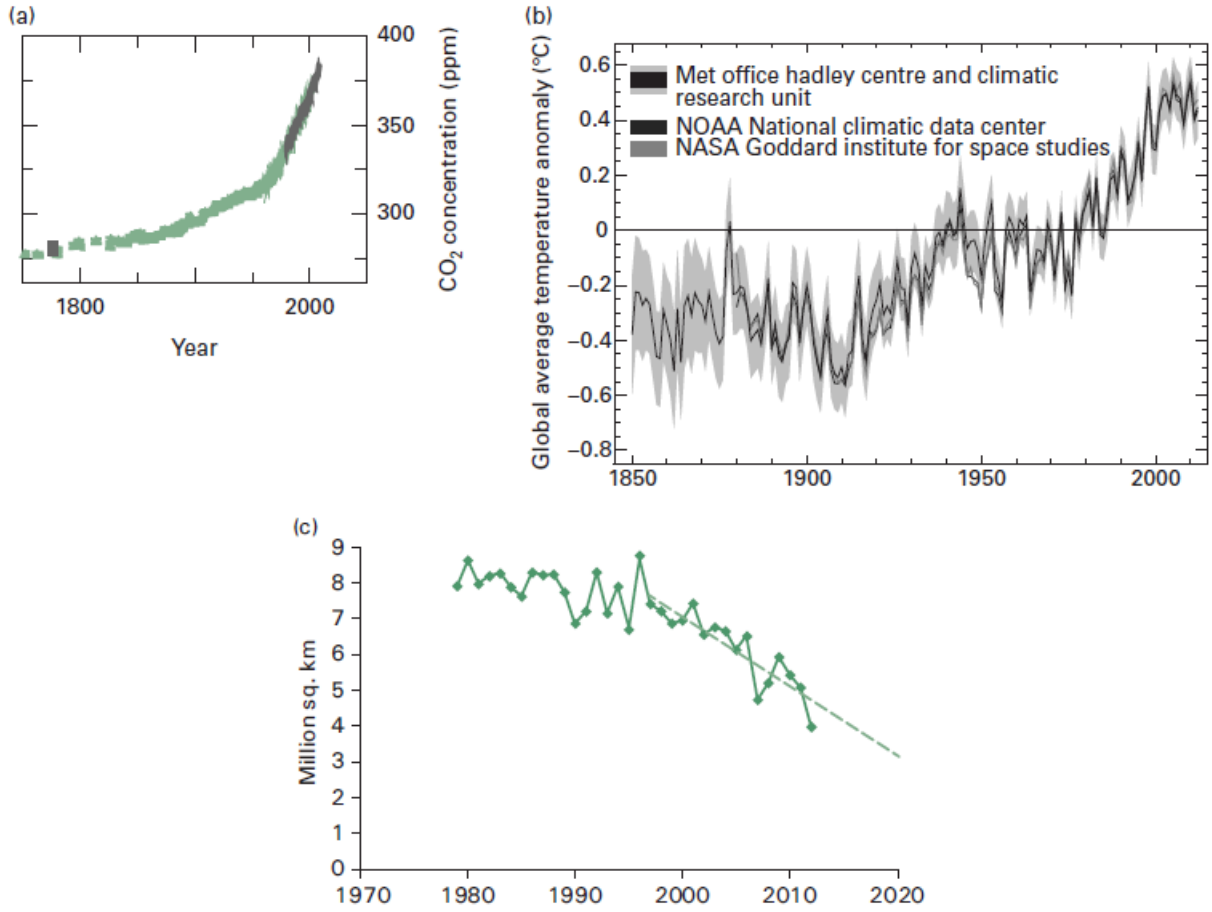

Figure 2.1.2 – (a) CO_2 concentration as a function of the year from the 18^{th} century to 2005. (b) Global average temperature anomaly as a function of the year from 1850 to 2012. (c) Extension of Arctic sea ice from 1979 to 2012 (measurement performed in semptember every year). Figure obtained from [3].

2.2 The Sun as a Promising Energy Source and the Photocatalytic Water Splitting Reaction

The previous section showed that the fossil fuels have their days counted as energy sources and the best options to replace them are sustainable and renewable energy sources. Figure 2.2.1 presents the natural energy flux that occurs on Earth. It is possible to observe that the available renewable sources are the solar radiation, geothermal activity and gravitation (orbital motion). Furthermore, one can notice that the energy magnitude of the solar radiation is 4000 times higher than the magnitude from geothermal activity and 40000 times higher than that associated to the orbital motion. Moreover, as presented in the previous section, the world total energy consumption in 2015 was about 3.9×10^{20} J [1]. For comparison purpose, the solar energy that reaches the Earth's surface in 1 hour is around 4.3×10^{20} J (120000 TWh), as presented in Figure 2.2.1. Around 80000 TWh of this solar energy is destined to the process of sensible heating, like solar water heaters and

solar dryers, over 40000 TWh is destined to the latent heat of water evaporation process, about 300 TWh is destined to the kinetic energy of the wind and wave turbines and 100 TWh is destined to the photon absorption processes in photovoltaic panels, for example. Therefore, an efficient use of the solar radiation energy can be the solution for the world energy supply in the next decades, which makes the Sun the most promising sustainable and renewable energy source.

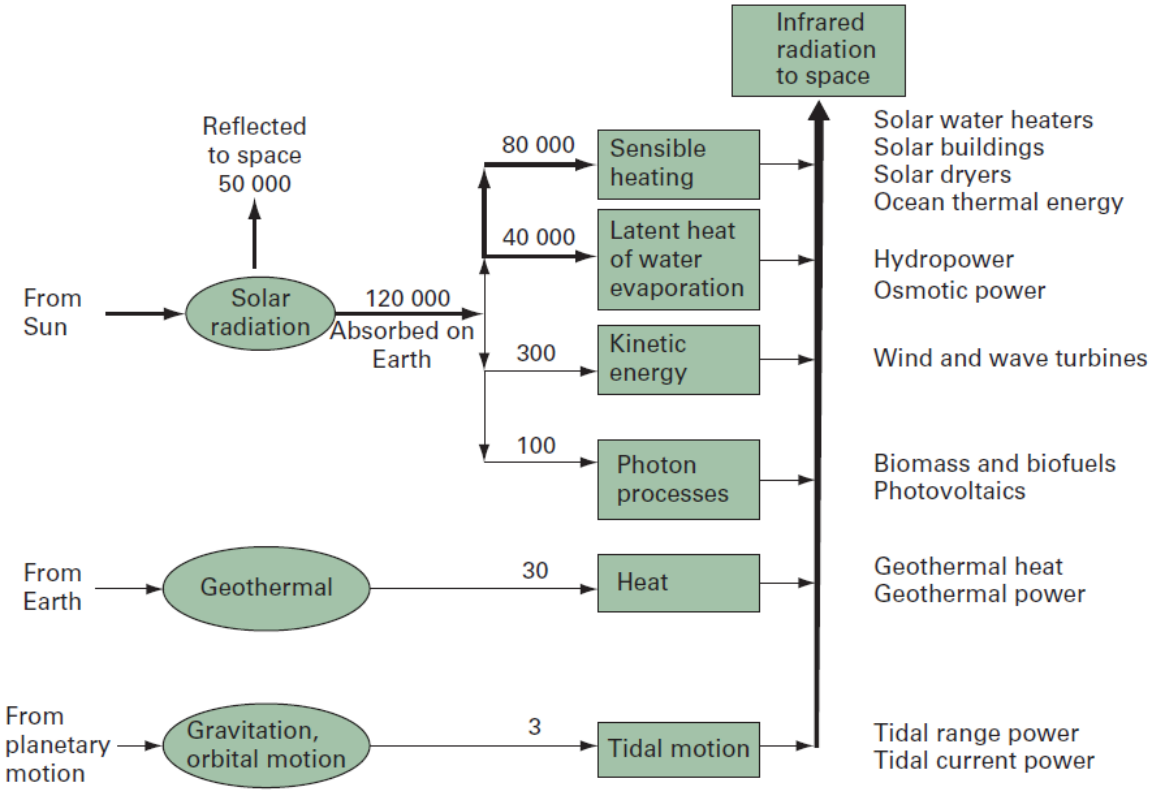

Figure 2.2.1 – Renewable energy systems on Earth. The numbers represent the energy in terawatts.hour (10^{12} Wh) corresponding to each process. Figure obtained from [3].

There are many different ways to utilize the solar energy. One of the most studied ways is to use the solar energy to produce electricity by using photovoltaic conversion systems, [29]. However, the world's societies cannot operate effectively with energy provided only for electricity, it requires some kind of fuel as well [4]. A good candidate for fuel source, that is sustainable and renewable, obtained from solar energy and that the scientific community dedicated great attention in the most recent years, is the H_2 [4–9]. Moreover, there are several works discussing and investigating different forms to store hydrogen in a safe and viable way [10–13]. For general use in small quantity, it is possible to store hydrogen in compressed gas or liquid form. The compressed hydrogen gas is reliable, has an indefinite storage time, easy to use and has accessible cost, but it has a low storage density which depends on its pressure. The liquid hydrogen has a higher density than the compressed hydrogen gas, which allows light, compact vehicular storage and

efficient delivery. The main disadvantage of the liquid hydrogen storage is the high cost to maintain it at cryogenic temperatures. Another way to store hydrogen is using a storage material. An optimum hydrogen storage material must have high volumetric hydrogen storage capacity, fast absorption kinetics, near room temperature and ambient pressure operation, low weight and low cost. The promising kind of material for this application are the metal hydrides. It is able to reversibly bind and store large quantities of hydrogen and, when necessary, individual molecules can be released.

A very promising method to obtain hydrogen utilizing the solar energy is the photocatalytic water splitting reaction. Fujishima and Honda observed the water splitting reaction for the first time in 1972 with photoelectrolysis using TiO_2 as photoelectrode and Pt as counter electrode [30]. Figure 2.2.2 presents the electrochemical cell used by Fujishima and Honda aiming to obtain H_2 and O_2 from water [30]. This cell consists in a TiO_2 photoelectrode connected with a Pt counter electrode through an external circuit, where both TiO_2 and Pt electrodes are in contact with water. When the surface of TiO_2 photoelectrode was irradiated with UV light, electron-hole pairs were generated. At the Pt counter electrode, the photogenerated electrons reduced water to form H_2 while holes oxidized water on the TiO_2 electrode to form O_2. From this discovery, numerous scientists have extensively studied photocatalytic water splitting reaction utilizing semiconductor photocatalysts aiming to improve the efficiency of the reaction. However, the efficiency is still low and should be optimized.

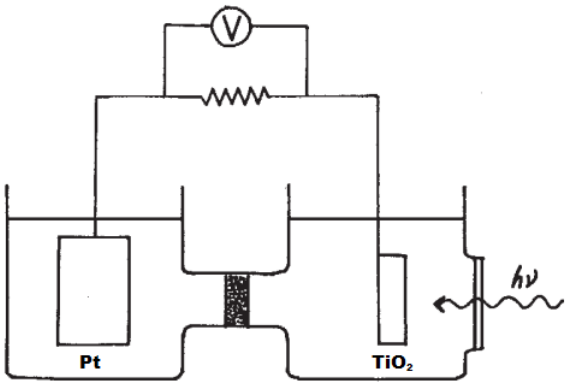

Figure 2.2.2 – Schematic representation of the electrochemical cell used by Fujishima and Honda. Figure adapted from [30].

The photocatalytic water splitting reaction is illustrated by Figure 2.2.3 and can be described as [31]:

$$2\gamma \longrightarrow 2e^-_{CB} + 2h^+_{VB} \text{ (Photon induced the } e^-/h^+ \text{ pairs generation)}$$

$$H_2O + 2h^+ \longrightarrow 2H^+ + \tfrac{1}{2}O_2 \text{ (Water oxidation half reaction)}$$

$$2H^+ + 2e^- \longrightarrow H_2 \text{ (Proton reduction half reaction)}$$

$$H_2O + 2\gamma \longrightarrow H_2 + \tfrac{1}{2}O_2 \text{ (Net overall water splitting)}$$

$$V^{\circ}_{rev} = 1.23\,V \text{ (Standard reversible potential)}$$

where γ represents a photon, e^- an electron, h^+ a hole and V°_{rev} the standard reversible potential. A solution containing water and the photocatalyst is irradiated with solar energy. The photons that have energy higher or equal to the photocatalyst band gap energy can be absorbed by the photocatalyst. In this case, electrons in the valence band are promoted to the conduction band and holes are left in the valence band of the semiconductor. In other words, electron-hole pairs are created in the photocatalyst. The holes (h^+) are responsible to perform the water oxidation half reaction, producing oxygen gas (O_2). The electrons (e^-) are responsible to perform the proton (H^+) reduction half reaction, producing hydrogen gas (H_2). Therefore, photocatalytic water splitting reaction consists in utilizing the solar radiation to split the water molecule aiming to obtain hydrogen and oxygen gases by using a semiconductor photocatalyst.

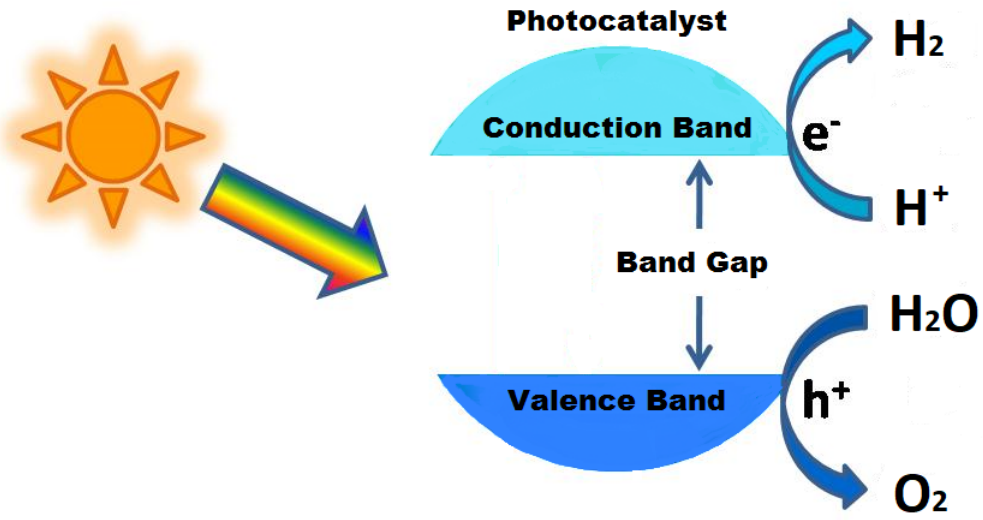

Figure 2.2.3 – Schematic representation of the photocatalytic water splitting reaction using a semiconductor photocatalyst.

In order to improve the efficiency of the photocatalytic water splitting reaction there are three main properties of the photocatalyst that should be optimized [31, 32]. Firstly, the energy position of the valence and conduction bands of the semiconductor and its band gap energy play a very important role for an efficient absorption of photons and, consequently, to perform the water splitting reaction. In order for the reaction to be thermodynamically possible, a condition must be met: the energy position of the bottom of the conduction band of the semiconductor has to be lower (more negative) than the redox potential of H^+/H_2 (0 V vs. NHE), while the energy position of the top of the valence band of the semiconductor has to be higher (more positive) than the redox potential of

O_2/H_2O (1.23 V vs. NHE). Figure 2.2.4 presents the energy position of the top of the valence band and bottom of the conduction band of several semiconductor materials. Moreover, as the water splitting reaction presents a standard reversible potential of 1.23 V, the semiconductor must have a minimum band gap energy of 1.23 eV for the occurrence of the reaction. However, the higher the band gap energy of the semiconductor the higher the energy of the photons needed to generate the electron-hole pairs that are used in the proton reduction and water oxidation reactions. The solar spectrum comprises the electromagnetic spectrum from the more energetic X-rays to long-wavelength radio waves. The shape of the solar spectrum is quite similar to a blackbody spectrum for an effective temperature near 5800 K, which presents a maximum intensity near to 480 nm [29]. Figure 2.2.5 presents the solar spectrum from around 200 nm to 2300 nm wavelength, which can be divided in infrared, visible and ultraviolet regions, measured outside the atmosphere and at Earth's surface. For the solar spectrum measured outside the atmosphere, the infrared region (radiation wavelength higher than 700 nm) constitutes 52 % of the solar spectrum and corresponds to photons with an energy lower than 1.8 eV. The visible region (radiation wavelength between 400 nm and 700 nm) constitutes 43 % of the solar spectrum and corresponds to photons with an energy between 1.8 eV and 3.1 eV. The ultraviolet region (radiation wavelength lower than 400 nm) constitutes 5 % of the spectrum and corresponds to photons with an energy higher than 3.1 eV [3]. For the solar spectrum measured at Earth's surface, the visible region is more intense than the infrared region due to the absorption of infrared radiation by the molecules present in the atmosphere. Therefore, in order to improve the photon absorption of the photocatalyst used in the photocatalytic water splitting reaction and utilize the solar energy in an efficient way, it is important to use a semiconductor photocatalyst that presents a band gap energy lower than 3.1 eV. In Figure 2.2.4 it is possible to observe a wide range of band gap energies of the materials. Some of the presented materials have a band gap energy higher than 1.23 eV, but do not present the valence or conduction band at the energy position that met the thermodynamic condition that enabled the water splitting reaction (CdSe, MoS_2, WO_3, Fe_2O_3). However, oxide materials allow shifting the energy position of the conduction and valence bands by changing the pH of the medium and, therefore, enables the reaction occurrence [33, 34]. Gratzel [33] studied a colloidal semiconductor of TiO_2 that is excited by a short laser pulse in order to generate electron-hole pairs and to reduce the methylviologen (MV^{2+}). It demonstrated a possibility of changing the position of the TiO_2 conduction band by altering the pH of the colloidal semiconductor, which improved the MV^{2+} reduction.

The second main property needed for the photocatalysts consists in an efficient separation of the electron-hole pair created [32]. The e^- (h^+) should migrate to the active reaction sites without being recombined with another h^+ (e^-). The crystalline quality of the photocatalyst plays a major role in the photocatalytic activity because its defects,

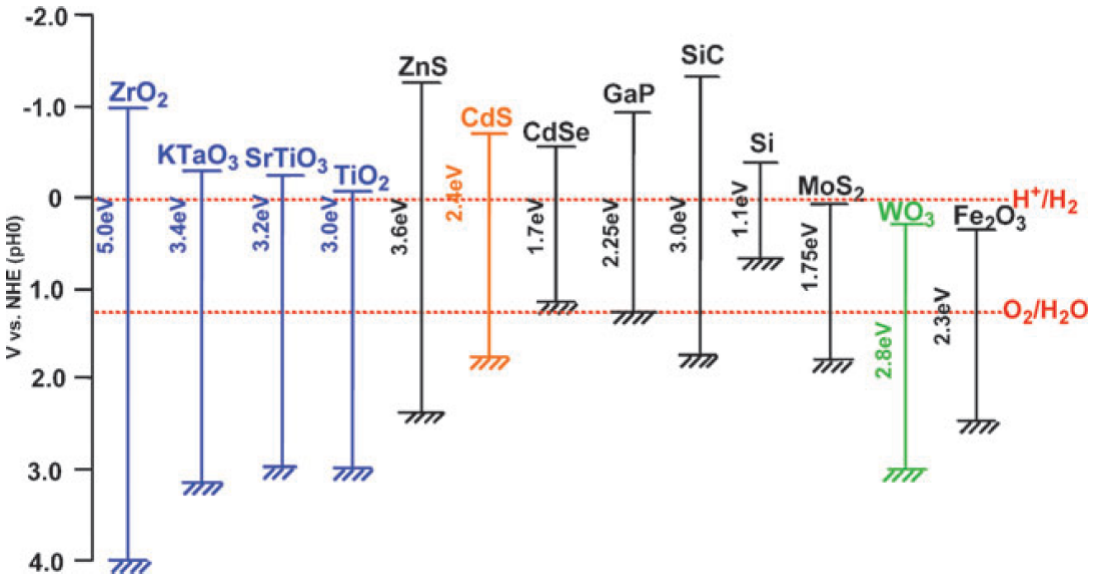

Figure 2.2.4 – Comparison between the energy position of the top of the valence band and bottom of the conduction band of several semiconductor materials and the redox potentials of water splitting. The band gap energy of each material is presented as well. Figure obtained from [32].

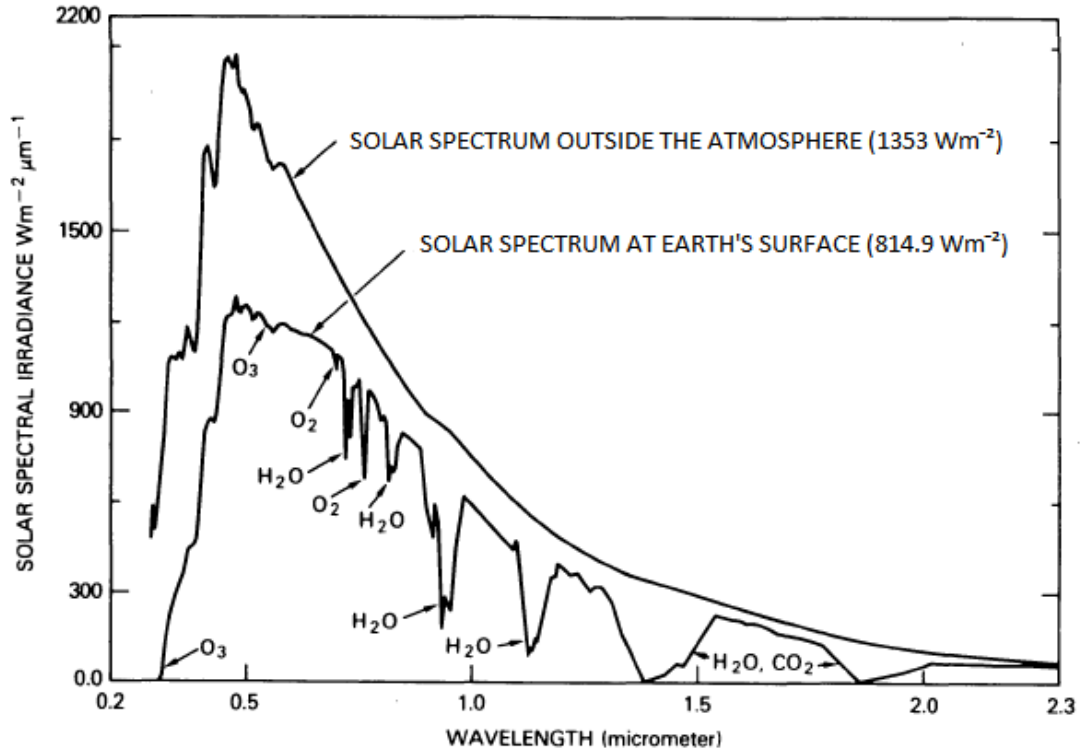

Figure 2.2.5 – Spectral solar irradiance as a function of the radiation wavelength measured outside the atmosphere and at Earth's surface. For the spectrum measured at Earth's surface, the absorption bands caused by water vapor (H_2O), carbon dioxide (CO_2), oxygen gas (O_2) and ozone (O_3) molecules present in the atmosphere are identified. Figure adapted from [35].

such as atomic vacancies, represent traps and recombination centers for electrons and holes, which avoids migration of the electron-hole pair to the active reaction sites. Moreover, the photocatalyst particle size also can play an important role in the photocatalytic activity. The smaller the particle the shorter the distance that photogenerated electrons and holes need to diffuse to migrate to reaction sites at the material's surface. It decreases the recombination process, increasing the photocatalytic activity.

The third main property needed for the photocatalysts is the presence of active reaction sites on the material's surface. Even if the properties presented above would be optimized, the water splitting reaction will not occur if the photocatalyst does not present active sites for redox reactions, like oxygen vacancies for oxide materials. However, since the oxygen vacancies also decrease the crystalline quality and increase the recombination process, there is an optimum oxygen vacancy population which maximizes the photocatalytic activity. Moreover, the higher the amount of active sites for redox reactions the higher the photocatalytic activity and the amount of active sites are proportional to the surface area of the photocatalyst. Therefore, high surface area materials with tunable oxygen vacancy population is the main candidate to optimize the photocatalytic activity.

Several materials applied to the photocatalytic water splitting reaction can be found in the literature. Photocatalysts based on Ti (TiO_2 [14], $SrTiO_3$ [15], La_2TiO_7 [36]), Nb ($Sr_2Nb_2O_7$ [37], $K_4Nb_6O_{17}$ [38], $Ba_5Nb_4O_{15}$ [39]), Ta (Ta_2O_5 [40], $NiTa_2O_6$ [16], $NaTaO_3$ [41]), In ($CaIn_2O_4$, $SrIn_2O_4$ [42]), Ga ($ZnGa_2O_4$ [43], Ga_2O_3 [44]), and Ce [45] (CeO_2 [17]) are only few examples of photocatalysts that can be found. One of the most investigated photocatalysts is the TiO_2 [46]. Kong *et al.* studied the influence of defects on the photocatalytic activity by synthesizing TiO_2 nanocrystals with tunable bulk/surface ratio of O vacancies and by using Transmission Electron Microscopy (TEM), X-ray Diffraction (XRD), N_2 adsorption-desorption isotherms, positron annihilation, and photocurrent measurements in order to characterize the samples. The authors found that decreasing the relative concentration ratio of bulk defects to surface defects, in TiO_2 nanocrystals, improves the electron-hole pair separation efficiency, decreasing the recombination probability and improving the photocatalytic efficiency. However, the band gap energy of TiO_2 is usually higher than 3.0 eV, which does not allow an efficient use of the solar energy in the main part of the solar spectrum. This issue can be resolved by doping the photocatalyst with some element or by using a material (co-catalyst), usually a metal, supported on the photocatalyst. The disadvantage of doping the photocatalyst is that the crystallinity of the photocatalyst decreases, which adds electron-hole recombination centers and the photocatalytic activity decreases. The co-catalyst is able to improve the charge separation to extend the solar radiation absorption into the visible region [47, 48], because the position of the conduction and valence bands of the combined system (photocatalyst + co-catalyst) can provide an effective charge separation and a band gap energy compatible with the visible light irradiation. Figure 2.2.6 shows a schematic representation of a pos-

sible utilization of a co-catalyst in order to improve the electron-hole pair separation and, therefore, to decrease the electron-hole recombination probability. The electron-hole pair production occurs in both photocatalyst and co-catalyst. The photogenerated electrons in the higher conduction band are transferred to the lower conduction band while the holes in the lower valence band are transferred to the higher valence band. It provides a spatial separation of the electron-hole pairs that results in a lower recombination probability and higher photocatalytic activity. Therefore, the use of a co-catalyst not only improves the photon absorption but can also separate the electron-hole pair more efficiently. This solution can be employed not only for the TiO_2 photocatalyst. Actually, it is possible to find in the literature different metals being widely used as co-catalyst or worn as dopping of the photocatalysts in photocatalytic reactions for many different kinds of semiconductors [32].

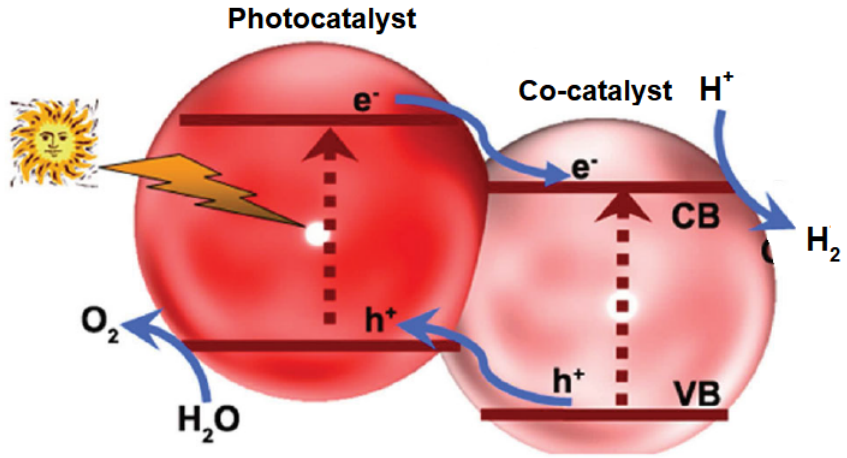

Figure 2.2.6 – Schematic representation of the utilization of a co-catalyst. Figure adapted from [49].

The semiconductors that present only the conduction (valence) band in the corrected energy position, required by the water splitting reaction, still can be used as photocatalysts to obtain H_2 (O_2) if a reducing agent (oxidizing agent) is used to capture the holes (electrons) that do not present the right potential to oxidize (reduce) the water molecule. Examples of reducing agents are methanol, ethanol and molecules that contain sulfide ions. These agents act as electron donors being, irreversibly, oxidized by the photogenerated holes. It enriches the photocatalyst with electrons that reduce the water molecule obtaining H_2. The H_2 production using this process can be very interesting if abundant compounds in nature and industries are used as reducing agents, like biomass and glycerol [50–52]. On the other hand, examples of oxidizing agents are silver (Ag^+) or iron (Fe^{3+}) cations. Analogously, these agents act as trapping of electrons irreversibly reducing the photocatalyst, capturing the photogenerated electrons. It enriches the photocatalyst with holes that oxidizes the water molecule and obtains the O_2 molecule. Also, in addition to allowing the H_2 or O_2 production for some photocatalysts, the sacrificial (reducing or oxidizing) agents improves the photocatalytic reaction, because they decrease

the recombination of the electron-hole pairs [32]. Figure 2.2.7 presents how the reaction occurs using sacrificial agents for two types of photocatalysts, one that uses a reducing agent to capture the holes to obtain H_2 (Figure 2.2.7)(a) and other that uses an oxidizing agent to capture the electrons to obtain O_2 (Figure 2.2.7)(b). Finally, it is important to stress out that the H_2 or O_2 obtained from the water molecule using a sacrificial agent is not considered water splitting. Water splitting is defined as obtaining both H_2 and O_2 in a stoichiometric amount in the absence of sacrificial agents [32].

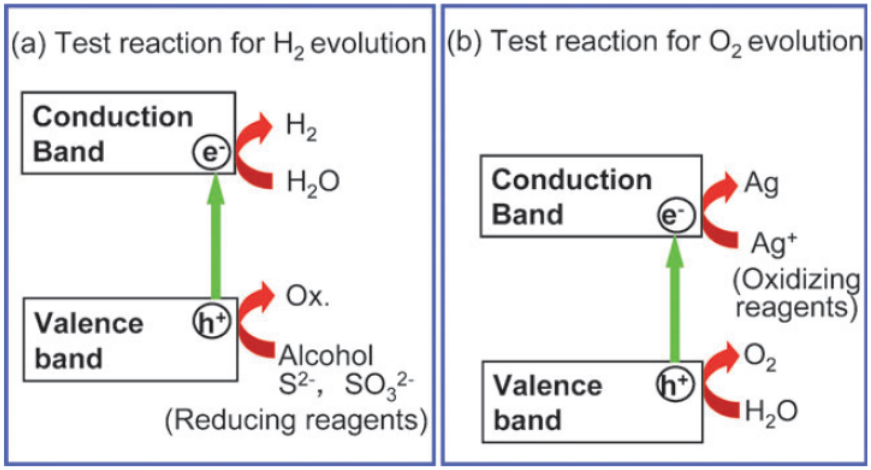

Figure 2.2.7 – Sacrificial agents used as (a) electron donors, improving the H_2 evolution, and (b) electron scavengers, improving the O_2 evolution. Figure obtained from [32].

2.3 Cerium Oxide as Photocatalyst Employed to H_2 Production

The cerium oxide (CeO_{2-x}, $0 < x < 0.5$) or ceria (CeO_2) is widely used currently in several fields of knowledge such as catalysis, fuel cells, and optics [18–21]. The main characteristic that makes it of great interest is the facility in creating and eliminating oxygen vacancies on the surface in a reversible way. This property is responsible for the high capacity of oxygen storage of ceria. Moreover, this property is important for catalytic applications because defects such as oxygen vacancies are one of the most reactive sites existing in metal oxides [53]. It makes catalysts containing ceria much more effective, for example, for the control of pollutant gas emission in the automotive industry when compared to catalysts without ceria [53, 54]. The use of ceria as support and catalyst has been widely investigated by the Physics of Nanostructures Laboratory in the Instituto de Física at UFRGS recently [21, 22, 55, 56]. Moreover, ceria has attracted great attention in the last years for energy applications, like H_2 production [57–59]. The reason is that ceria presents optimum positions of the conduction and valence bands. Issarapanacheewin *et al.* [60] characterized CeO_2/Bi_2WO_6 composite photocatalysts by means of XRD, Scanning Electron Microscopy (SEM), UV-Visible Spectroscopy (UV-Vis) and obtained the

positions of the CeO_2 conduction and valence bands of -0.23 V vs. NHE and 2.35 V vs. NHE, respectively. This result agrees with the result obtained by Magesh *et al.* [61], which characterized mixed oxides of CeO_2-TiO_2 applied to the decomposition of methylene blue by means of XRD, Thermogravimetric Analysis (TGA), TEM, SEM, UV-Vis and obtained the conduction and valence bands positions for pure CeO_2 of -0.32 V vs. NHE and 2.44 V vs. NHE, respectively. A slightly different value for the positions of the conduction and valence bands of the CeO_2 is obtained by Abdullah *et al.* [62]. They studied the CeO_2-TiO_2 photocatalyst applied to the photocatalytic reduction of CO_2 into methanol using XRD, Field Emission Scanning Electron Microscopy (FESEM), X-ray Photoelectron Spectroscopy (XPS), Nitrogen Physisorption Analysis, UV-Vis, Photoluminescence Spectroscopy (PL) and obtained the conduction and valence bands positions for CeO_2 of -0.07 V vs. NHE and 2.19 V vs. NHE, respectively. The cerium oxide itself can be used to convert only a small portion of the solar energy that reaches Earth due to its relatively high direct band gap energy, which vary typically from 2.92 eV to 3.70 eV [63, 64]. In the literature, this drawback is usually overcomed using a co-catalyst. Li *et al.* [65] synthesized heterostructured CdS/CeO_x nanowires by an electrochemical process and applying these nanowires to a photocatalytic reaction in order to produce H_2 from water. The CdS acts as a visible light co-catalyst, because it presents a band gap energy around 2.4 eV. Figure 2.3.1 shows that the photogenerated electrons in the conduction band of CdS are transferred to the Ce 4f orbital of CeO_2 and the photogenerated holes in the valence band of CeO_2 are transferred to the valence band of CdS. This process facilitates the separation of the electron-hole pairs and reduces their recombination, improving the photocatalytic efficiency. Similarly, Primo *et al.* [17] studied the photocatalytic activity of CeO_2 nanoparticles synthesized by alginate precipitation supported with small amounts (1.0 wt % and 3.0 wt %) of Au nanoparticles to produce O_2 from water. The 1.0 wt % Au/CeO_2 system presented an increase in the photocatalytic activity under visible light exposition in comparison to the 3.0 wt % Au/CeO_2 system and the CeO_2 sample without Au nanoparticles supported. Moreover, the Au/CeO_2 system presented a better photocatalytic activity under exposition to the visible light than the WO_3 photocatalyst, which presented a high photocatalytic activity to produce O_2 under exposition to UV light. Some other examples of co-catalysts, like Cs and zeolites, used with the CeO_2 photocatalyst can be found in the literature [45, 66, 67].

The comparison between the H_2 evolution photocatalytic activity of the TiO_2 with the CeO_2 photocatalyst shows that the CeO_2 material is a very promising photocatalyst to produce H_2 from water. Kato *et al.* [68] measured the H_2 production of TiO_2 (rutile) and various tantalate photocatalysts using a 450 W high pressure Hg lamp as light source and obtained a H_2 production of 0.04 $\frac{\mu mol}{hg}$ for TiO_2 (rutile). Sayama *et al.* [69] measured the H_2 production of TiO_2 using a 400 W high pressure Hg lamp as light source, utilizing Pt as co-catalyst and adding carbonate salts aiming to increase the concentration of carbonate

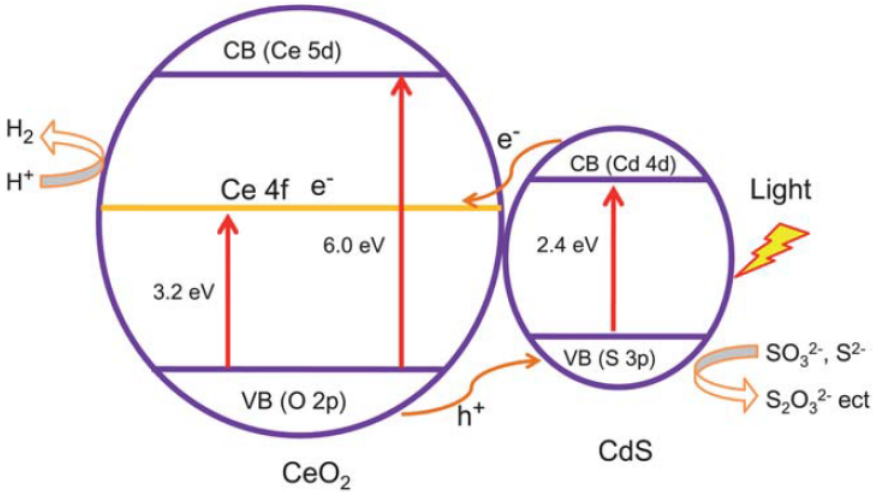

Figure 2.3.1 – Schematic representation of the electron-hole pair separation mechanism observed in the CdS/CeO_x nanowires [65].

ions in the photocatalytic solution. They obtained a H_2 production of 3.33 $\frac{\mu mol}{hg}$ for Pt-TiO_2 without carbonate salts. The change of the carbonate ions concentration in the photocatalytic solution by adding Na_2CO_3 gives a dramatic increase of the H_2 production to 1893.33 $\frac{\mu mol}{hg}$. Reddy *et al.* [45] measured the H_2 production of pure CeO_2 using a 400 W high pressure Hg lamp as light source and obtained a H_2 production of 12.50 $\frac{\mu mol}{hg}$. This result obtained for pure CeO_2 is quite higher than the result obtained for pure TiO_2 or Pt-TiO_2 without carbonate salts. Moreover, Chung *et al.* [66] measured the H_2 production of CeO_2 using a 450 W high pressure Hg lamp as light source and utilizing 1 % wt of Pt, Li or Cs as co-catalyst. The results of H_2 production obtained for CeO_2, Pt/CeO_2, Li/CeO_2 and Cs/CeO_2 are 7.08 $\frac{\mu mol}{hg}$, 7.67 $\frac{\mu mol}{hg}$, 8.35 $\frac{\mu mol}{hg}$ and 81.60 $\frac{\mu mol}{hg}$, respectively. It is possible to observe that the Cs/CeO_2 system presents a H_2 evolution photocatalytic activity more than ten times that obtained for pure CeO_2. Since the CeO_2 used in the works cited above was the CeO_2 standard commercial, there are many parameters that can be optimized aiming to improve the photocatalytic activity of the CeO_2 material in comparison with those works. It can give an even higher H_2 evolution photocatalytic activity than that obtained for TiO_2.

The increase of the photocatalytic activity of the CeO_2 photocatalyst employed to produce H_2 from water can be performed by using a reducing agent [70]. Lu *et al.* [70] grow CeO_2 hexagonal nanorods with {110} orientation onto Ti substrates by using an electrochemical method and apply these nanorods to a photocatalytic reaction to produce H_2 from water using Na_2S-Na_2SO_3 and methanol as reducing agents. The synthesized CeO_2 nanorods presented a higher photocatalytic activity in comparison with the commercial CeO_2, CdS and TiO_2 for both reducing agents. Furthermore, the Na_2S-Na_2SO_3 reducing agents provided a higher photocatalytic activity for the CeO_2 nanorods. Aiming to explain these results, the authors proposed that the agent reduced some Ce atoms

in the nanorods from Ce(IV) to Ce(III) and then the photogenerated holes oxidized the Ce atoms from Ce(III) to Ce(IV). This process improved the photocatalytic activity and since the reductive ability of S^{2-} and SO_3^{2-} ions are higher than the methanol, it makes sense that the Na_2S-Na_2SO_3 reducing agents provided a higher photocatalytic activity for the CeO_2 nanorods. Another characteristic that can increase the photocatalytic activity of the CeO_2 photocatalyst employed to produce H_2 from water is the presence of mesopores on the cerium oxide surface. The mesopores increase the surface area, which provides more adsorption sites for water molecules and more reaction active sites for the reaction. Moreover, mesoporous semiconductors usually present a high degree of crystallinity that provides a more effective separation and diffusion of the electron-hole pairs photogenerated, which improves the photocatalytic activity [49].

In a previous work [22], the possibility to tune the particle size, surface area and oxygen vacancy population of cerium oxide nanoparticles by changing the synthesis parameters was demonstrated. These nanoparticles were synthesized with a wide range of surface area ($96 < S_{BET} < 201 m^2/g$), pore volume ($32 < V < 132 mm^3/g$), diameter ($2 < d < 90 nm$) and Ce(III) fraction values, which are directly related to the oxygen vacancy population. Moreover, the synthesized nanoparticles present pore distribution in the microporous range and some of them in the mesopores range as well. After synthesis, the cerium oxide nanoparticles were exposed to a CO atmosphere and heated from room temperature to 500 °C and characterized by in situ techniques like Near Ambient Pressure XPS (NAP-XPS) and time-resolved X-ray Absorption Near Edge Structure (XANES). The results showed a very high reducibility at very low temperatures of the cerium oxide nanoparticles in comparison to the literature values typically found. Therefore, it is a promising system to be applied for the H_2 production since the photocatalytic activity can be optimized by tuning the structural and electronic properties of the cerium oxide nanoparticles synthesized. In the present work, an experimental and theoretical investigation was performed using the cerium oxide nanoparticles synthesized in the previous work [22] aiming to elucidate the main properties of the cerium oxide that are important to improve the photocatalytic activity of this photocatalyst when applied to the H_2 production reaction.

3 Physical Phenomena and Theoretical Background of the Methods of Analysis

In this chapter the physical phenomena and theoretical bases of the main methods of analysis used in this work will be presented: X-ray Diffraction (XRD), X-ray Photoelectron Spectroscopy (XPS), Ultraviolet Photoelectron Spectroscopy (UPS), X-ray Absorption Spectroscopy (XAS) and Density Functional Theory (DFT).

3.1 X-ray Diffraction (XRD) Technique

The XRD technique [71, 72] allows to identify the crystalline phases, to determine lattice parameters and to estimate crystallite sizes of crystalline materials. This technique consists on focusing a monochromatic X-ray beam to the sample at different angles with respect to the sample surface. A detector scans the intensity of the diffracted X-ray beam as a function of the angle 2θ between the incident and the diffracted beams, then constructing a diffraction pattern. Usually, the radiation used in XRD measurement is the Cu $K\alpha$ characteristic X-ray, which has an energy of 8.04 keV and a wavelength of 0.154 nm. The diffraction occurs because its X-ray wavelength is smaller and has the same order of magnitude than the distance between the atomic planes in a crystalline material.

The construction of a diffraction pattern can be understood with the Bragg's Law. Figure 3.1.1 presents the atomic planes of a crystalline material, with the atoms represented by the black circles, forming the A, B and C generic planes with the interplanar distance d. The numbered straight line segments represent the incident X-ray beams that are scattered by the crystal atoms. The scattered beam is detected with the maximum intensity when occurs a constructive interference, i.e., if the optical path difference between beam 2 and beam 1, for example, is an integer multiple of the X-ray wavelength λ. In this case

$$ML + LN = d\sin(\theta) + d\sin(\theta) = n\lambda \tag{3.1}$$

where n is a positive integer number. Then,

$$2d\sin(\theta) = n\lambda \tag{3.2}$$

The equation 3.2 is known as Bragg's Law and presents the condition to obtain a con-

structive interference in a XRD measurement, relating the distance between crystalline planes (d) and the angle (θ) of the incident beam. However, when angles slightly different from the angle that presents the complete constructive interference (θ_B) are considered, it is found that the destructive interference is not complete. It gives a broadening of the Bragg reflection in comparison to the case where only the constructive interference is considered. Moreover, the broadening of the Bragg reflection occurs also due to the experimental uncertainty of the measurement equipment, defects in the crystalline structure and size of the particles that constitute the material. The higher amount of defects (higher strain) and the smaller size of the particles the more wide is the Bragg reflection.

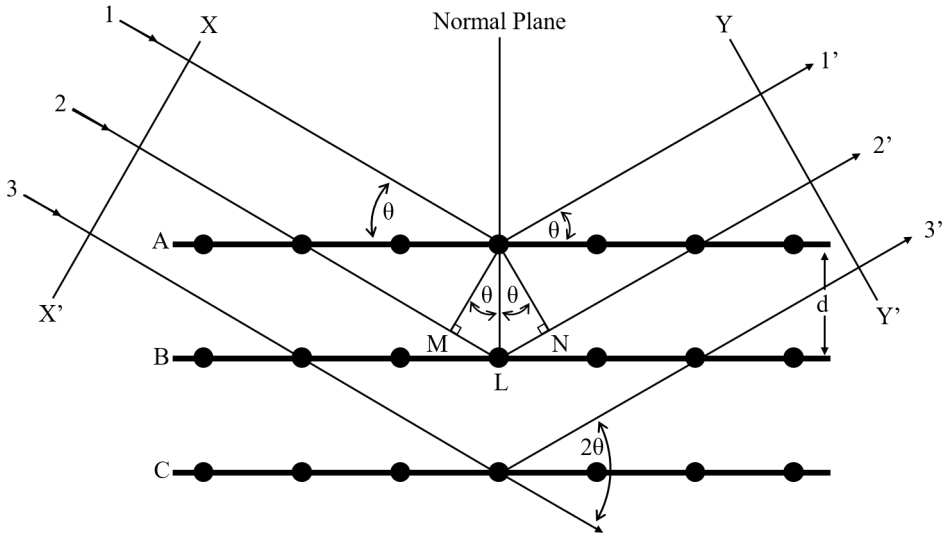

Figure 3.1.1 – Schematic of the X-ray diffraction in a crystalline material. Figure adapted from [72].

Figure 3.1.2 presents an example of the XRD pattern of the CeO_2 powder sample. The Miller indices (hkl) were used to identify the crystalline planes. Each crystalline structure corresponds to a set of Bragg reflections, which present specific relative intensities and positions, in the diffraction pattern. Therefore, the crystalline structure is determined comparing the position and relative intensities of the peaks in the diffractogram with a data base. After detemining the crystalline structure, the lattice parameter can be determined by the Bragg reflections position. The interplanar distance d can be obtained for a given reflection plane by equation 3.2 and, as the lattice parameter is related with d for a given reflection plane for a specific crystalline structure, the lattice parameter can be determined. Moreover, the size and strain of the particles that constitute the material can be obtained analysing the width of the peaks presented in the diffractogram. As mentioned previously, the defects in the crystalline structure and the size of the particles that constitute the material affect the width of the Bragg reflections. These two contributions are different and can be deconvoluted. One way to do that is using the Rietveld method, which will be presented in the Chapter 4.

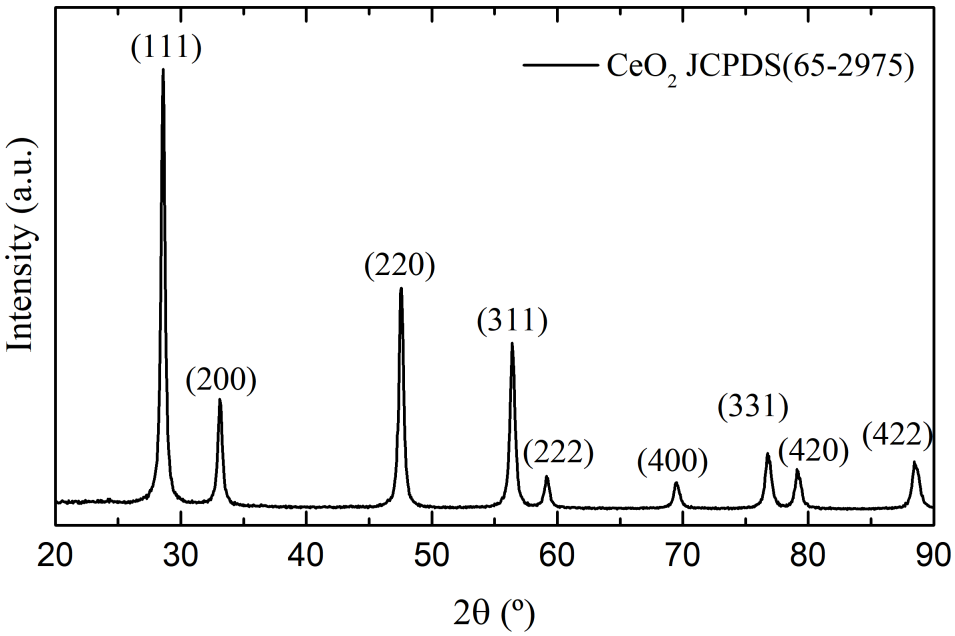

Figure 3.1.2 – Diffraction pattern of the CeO_2 standard sample. The peaks are identified with the Miller indices.

In general, there are three methods to perform the diffraction measurements: Laue method, rotating-crystal method and powder method. The Laue method was the first method used, based on the von Laue's original experiment. This method consists in keeping a single crystal fixed when irradiated by a polychromatic beam. A given Bragg reflection (given interplanar distance d) corresponds to a particular wavelength that satisfies the Bragg's Law a given θ value. There are two geometries of the Laue method that are characterized by the positions of the source, crystal and detector: transmission and back-reflection Laue methods. For both, the detector is placed perpendicular to the incident beam. Figure 3.1.3 presents these two geometries with a flat film as detector. The transmission Laue method (Figure 3.1.3(a)) consists in placing the crystal between the source and the film. Therefore, part of the beam is transmitted through the crystal to form a diffraction pattern in the film. The back-reflection Laue method (Figure 3.1.3(b)) consists in placing the film between the source and the crystal. In this configuration, there is a hole in the film where the beam passes through and irradiates the crystal. The back-reflected beam forms a pattern on the film. The position of the diffraction points on the film, for both geometries, depends on the orientation of the crystal relative to the incident beam. Moreover, the diffraction points become distorted if the crystal is bent or twisted. Therefore the Laue method is useful for two main goals: the determination of crystal orientation and the assessment of crystal quality.

The rotating-crystal method consists in to place a single crystal with one of its crystallographic axis normal to a monochromatic X-ray beam. A cylindrical film is placed around the crystal. Then, the crystal is rotated about a given direction, with the axis of the film

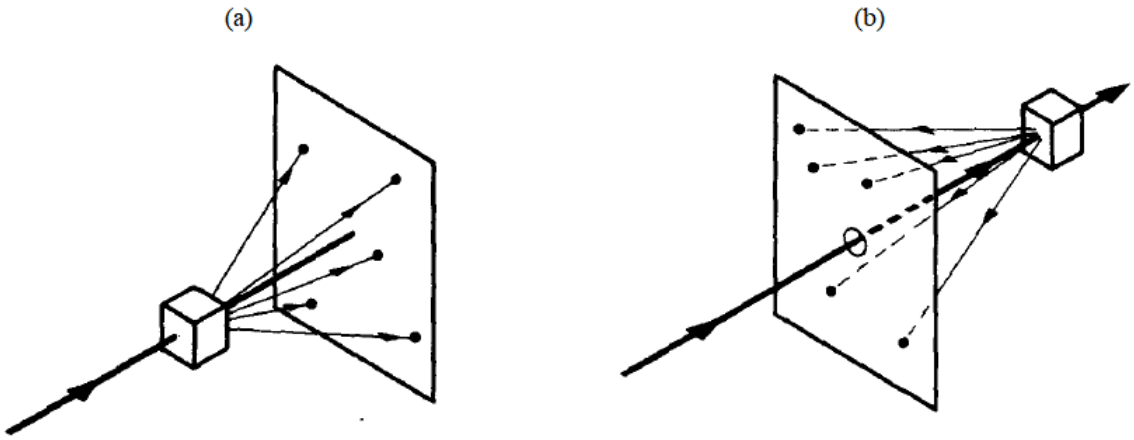

Figure 3.1.3 – Schematic of the (a) transmission and (b) back-reflection Laue methods. Figure obtained from [72].

coinciding with the axis of rotation of the crystal. So, a particular set of crystallographic planes will satisfy, for instance, the Bragg condition, while the crystal is rotating. The reflected beam forms diffraction points on the film. Figure 3.1.4 presents a schematic of this method. As the crystal is rotated about only one direction, it is not possible to obtain all Bragg reflections between 0° and 90° for every sets of planes. Even so, the rotating-crystal method corresponds to the most powerful tool in the determination of unknown crystal structures.

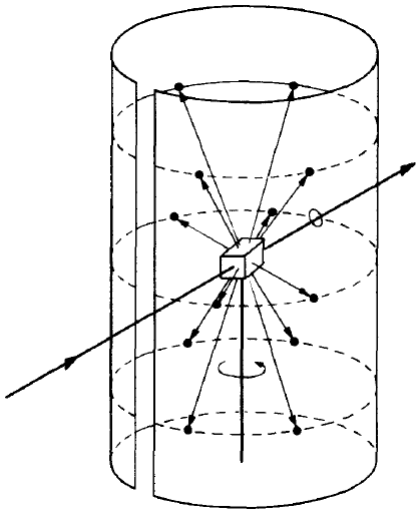

Figure 3.1.4 – Schematic of the rotating-crystal method. Figure obtained from [72].

The powder method consists in to irradiate a monochromatic X-ray beam to a crystal that was reduced to a very fine powder. The grain can be interpreted as a tiny crystal orientated randomly with respect to the incident beam. The result obtained is that every set of crystalline planes satisfy the Bragg condition. This result is equivalent to a single crystal rotated, not around one axis, but around all possible axes. Therefore, the diffracted beam forms a radiation cone for each set of crystalline planes present in the crystal. The

intensity of each radiation cone can be measured and, then, the diffraction pattern can be constructed. Figure 3.1.5 presents a schematic of the power method, showing three different radiation cones corresponding to three different sets of crystalline planes *hkl*. The powder method is the method used for policrystals and is especially useful to determine lattice parameters with high precision and to identify crystalline phases.

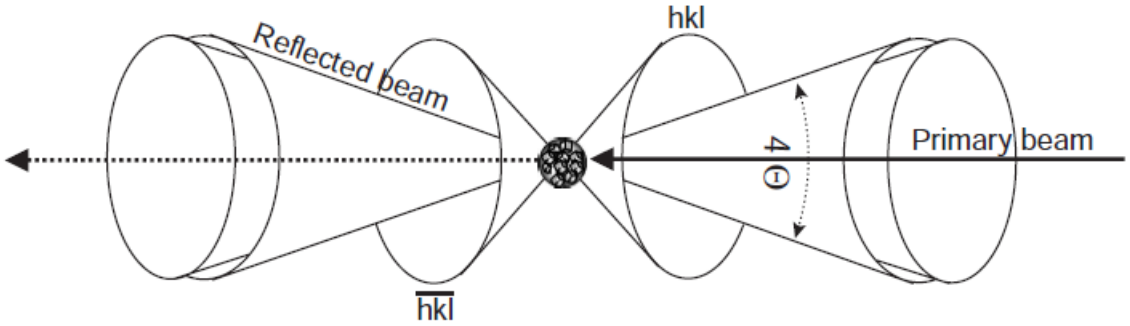

Figure 3.1.5 – Schematic of the power method. Three different radiation cones corresponding to three different sets of crystalline planes *hkl* are shown. Figure obtained from [73].

The most common configuration used for the XRD pattern measurements using the powder method is the Bragg-Brentano configuration. Figure 3.1.6 presents a schematic of this configuration. The divergent incident monochromatic beam is reflected in the sample surface and converges at the detector position (fixed radius). Slits placed after the source are responsible to control the divergence of the beam. Usually, the source is fixed and the sample holder and the detector are rotated in order to measure the diffraction pattern.

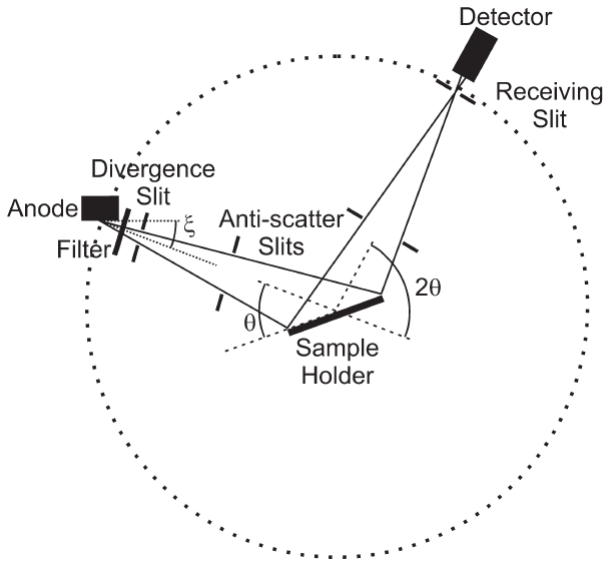

Figure 3.1.6 – Schematic of the Bragg-Brentano configuration. Figure obtained from [73].

3.2 X-ray Photoelectron Spectroscopy (XPS) and Ultraviolet Photoelectron Spectroscopy (UPS) Techniques

The electromagnetic radiation interacts with matter through several effects. Figure 3.2.1 presents the cross section as a function of the incident photon energy for a given physical phenomenon in the case of CeO_2. In the energy range corresponding to the ultraviolet light and X-rays, 3 eV to 500 keV, the photoelectric effect is the dominant one. In this effect, an electron in a bound state of the atom may absorb a X-ray photon. For an electron in a given electronic level, the incident photon with energy smaller than the electron binding energy is not absorbed. If the photon has an energy equal to the electron binding energy there is a non-zero probability of the photon to be absorbed and, in this case, the electron does not have kinetic energy to leave the atom and goes to an atomic excited state. Lastly, if the photon has an energy greater than the electron binding energy, there is also a probability of the photon to be absorbed and, in this case, the electron is ejected from the atom. The electron ejected from the atom due to a photon absorption is called photoelectron.

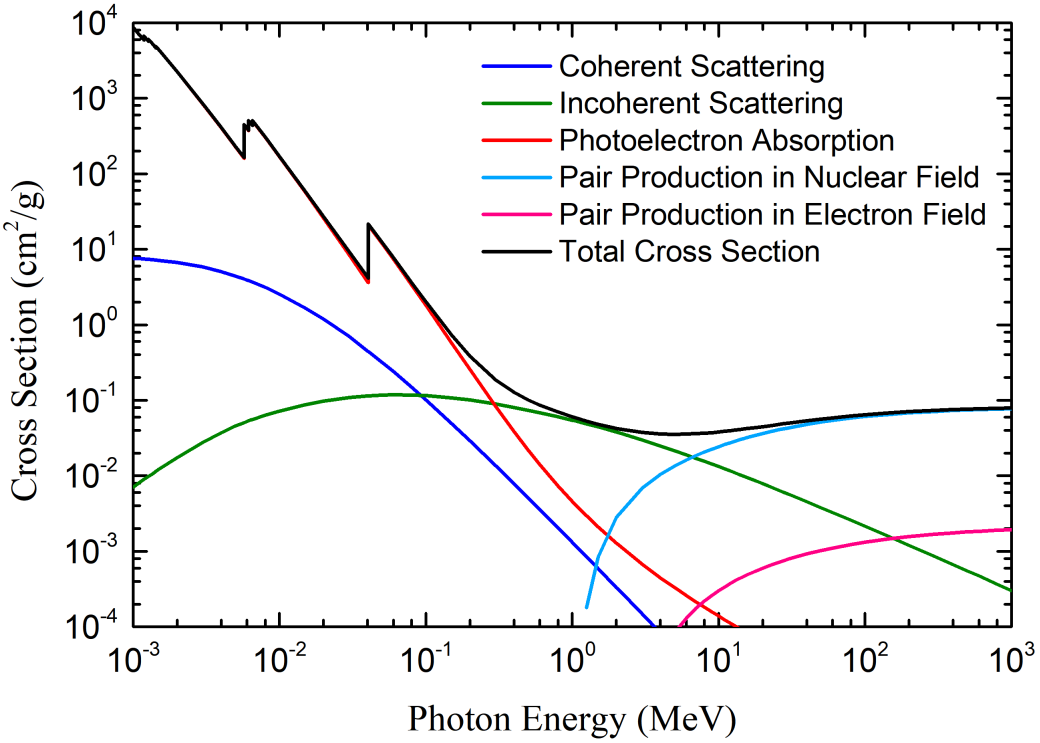

Figure 3.2.1 – Cross section of the several effects that occur when radiation interacts with matter as a function of the incident photon energy for CeO_2. Figure obtained from [74].

The XPS technique [71, 75] is widely used in catalysis because allows to obtain informations about the chemical composition, the oxidation state of the elements and the amount of each compound in the sample. The UPS technique [71, 75] allows to obtain

the molecular orbital energies of the valence band and to determine the material's work function. These techniques are based in the photoelectron effect and consist on focusing a light beam in a material and to measure the kinetic energy of the ejected photoelectrons from the material's surface. As presented in Figure 3.2.2, the kinetic energy (E_k) of the ejected photoelectron can be obtained by:

$$E_k = h\nu - E_b - \phi_s \tag{3.3}$$

where $h\nu$ is the energy of the incident radiation, E_b is the electron binding energy in the atom and ϕ_s is the work function of the sample. In order to measure the kinetic energy of the ejected photoelectrons, it is used an electron analyzer which has itself a work function ϕ_a that must be taken into account. Once the sample's work function usually is not known, it is possible to obtain the kinetic energy of the ejected photoelectrons without the ϕ_s value. In order to do that, the sample and the electron analyzer are grounded, aligning their Fermi levels. This alignment set a potential difference equals to $\phi_s - \phi_a$. In this way, the kinetic energy of the ejected photoelectrons can be written as

$$E_k = h\nu - E_b - \phi_s + (\phi_s - \phi_a) = h\nu - E_b - \phi_a \tag{3.4}$$

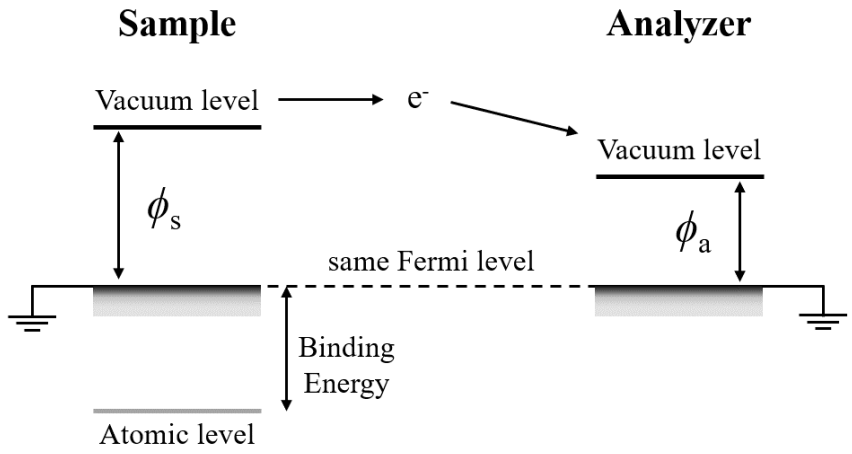

Figure 3.2.2 – Schematic representation presenting the energy levels involved in the photoemission process for the sample and for the electron analyzer.

The main difference between the XPS and UPS techniques lies in the incident radiation. The XPS technique usually works with Mg $K\alpha$ (1253.6 eV) or Al $K\alpha$ (1486.3 eV) X-ray sources while the most frequently used sources for the UPS technique are helium discharge lamps (UV source). These lamps produce fluorescence lines when the gas is excited in the discharge and then decays back to its ground state. By using a helium dis-

charge lamp it is possible to generate He I light (light emitted from neutral atoms), which has a photon energy of 21.2 eV, or He II light (light emitted by singly ionized atoms), which has a photon energy of 40.8 eV. Because of the different photon energy, while the XPS technique probes the electronic core levels of the atoms, the UPS technique probes the valence band.

The XPS and UPS spectra are usually a plot of the photoelectrons counts (or intensity) as a function of the electron binding energy in the atom [76]. The photoelectrons that suffer elastic scattering before being ejected of the material contribute to its characteristic atomic level peak. On the other hand, the photoelectrons that suffer inelastic scattering, losing energy before being ejected of the material, contribute to the spectrum background. Electrons in atomic states with non-zero orbital angular momentum give rise to a doublet in the spectrum due to the spin-orbit coupling. Therefore, each contribution of the doublet corresponds to a different total angular momentum ($j = l \pm s$). Photoelectron contributions are labelled according to the quantum numbers of the atomic level from which the electron originates.

Both XPS and UPS are surface sensitive techniques but the maximum depth of the sample that can be accessed by these techniques depends on the inelastic mean free path (λ_{IMFP}) of the ejected photoelectrons and the ejected photoelectron take-off angle (θ), measured with respect to the surface normal. The λ_{IMFP} is the mean distance travelled by the photoelectron before suffering an inelastic scattering in the sample. Its value depends on the kinetic energy of the photoelectron under consideration and can be described by an universal curve (Figure 3.2.3), because it is very similar to different materials. Tanuma *et al.* [77] developed the TPP-2M formula that can be used to calculate the inelastic mean free path of the photoelectrons in good agreement with the experimental results. The authors accomplished that by parametrizing the universal curve and adjusting the parameters in order to obtain a better agreement with the experimental results for each kind of material. The signal of the characteristic peaks in the XPS spectra is due to photoelectrons generated in the sample region from the surface until a depth of $3\lambda_{IMFP}\cos\theta$, where around 60 % of the signal comes from the surface region until a depth of around λ_{IMFP}. The λ_{IMFP} for photoelectrons ejected by typical X-ray and UV sources in XPS and UPS techniques is different and typically smaller in the UPS technique.

Besides the photoelectrons, other electrons can be ejected from the material and contribute to the spectrum. When the hole leaved by the ejected photoelectron is filled by an outer shell electron there is a non-zero probability that other electron is ejected from the atom in order to satisfy the energy conservation of the atomic relaxation process. This second electron, which is called Auger electron, has a fixed kinetic energy, independent of the incident X-ray energy. For that reason, the way to recognize the Auger contribution in the spectrum is to change the incident photon energy. The Auger contribution will appear in the same kinetic energy position for all the incident X-ray energies and the

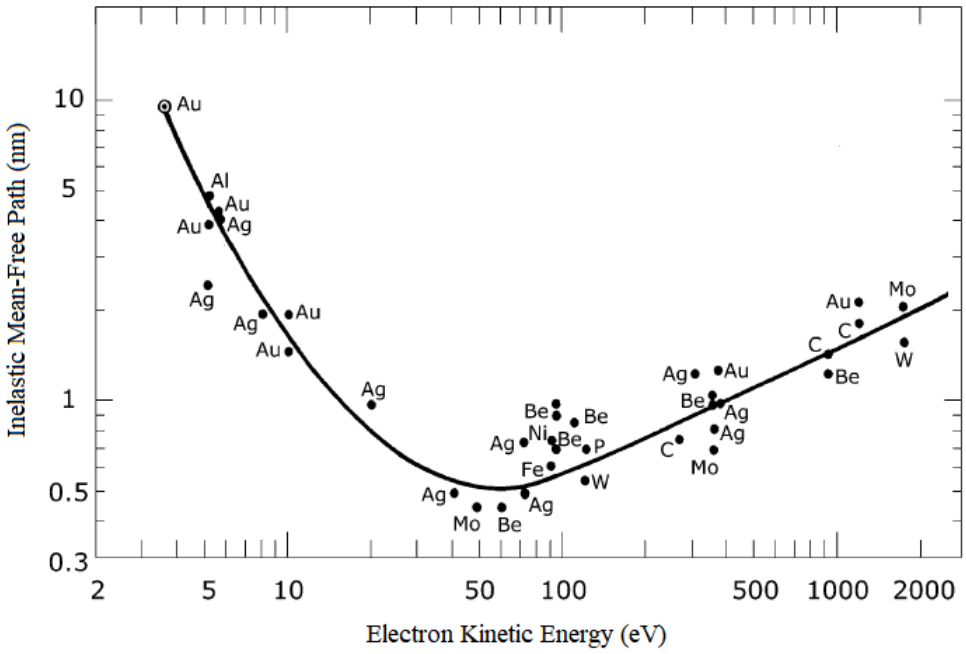

Figure 3.2.3 – Universal curve of the electron inelastic mean-free path as a function of the electron kinetic energy (solid line). The points represent measurements for different elements. Figure adapted from [71].

kinetic energy position of the peaks produced by the photoelectrons will change.

Auger contributions are labelled with the atomic shells involving in the emission process using the X-ray level nomenclature. For example, an KL_1L_2 Auger electron corresponds to a transition in which the hole leaved by the ejected photoelectron in the K shell is filled by an electron initially in the L_1 shell and the Auger electron is emitted from the L_2 shell.

Figure 3.2.4 presents examples of the XPS and UPS spectra of a CeO_2 sample. Figure 3.2.4(a) shows an UPS spectrum of a CeO_2 sample measured using a He II lamp (40.8 eV). The known incident photon energy and the electron binding energy in the atom, shown in Figure 3.2.4(a), allows to estimate the kinetic energy of the ejected photoelectrons and, by using the TPP-2M formula [77], one can conclude that this spectrum corresponds to $\lambda_{IMFP} = 3$ Å. The same can be performed with the spectra of Figures 3.2.4(b) and 3.2.4(c), which present XPS spectra of Ce 3d and Ce 4d regions measured with a Mg $K\alpha$ X-ray source. These two regions correspond to electrons of different binding energies and, therefore, contain informations of different depths of the sample. Performing the same procedure used to the UPS spectrum, one can conclude that the Ce 3d and Ce 4d regions correspond to $\lambda_{IMFP} = 8$ Å and $\lambda_{IMFP} = 18$ Å, respectively. In this way, using these three spectra is possible to obtain depth-resolved informations of the analysed material. Another possibility to probe different depths of the material is by changing the incident photon energy, easily achieved by using a Synchrotron Light Source, as performed in previous work of the group [55].

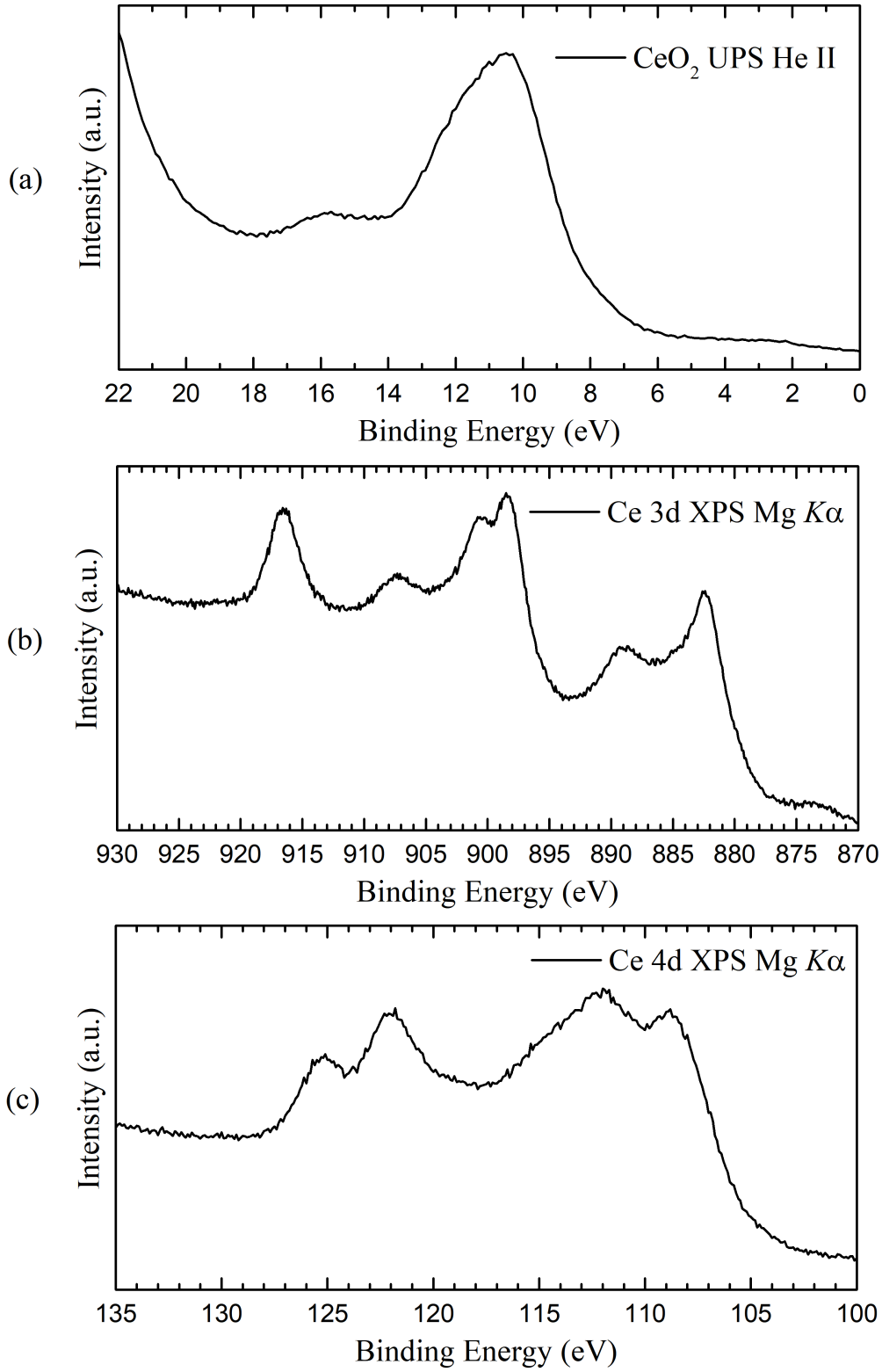

Figure 3.2.4 – (a) UPS spectrum of a CeO_2 sample measured using a He II light (40.8 eV). XPS spectra of a CeO_2 sample for the (b) Ce 3d and (c) Ce 4d regions measured using a Mg $K\alpha$ X-ray source.

The conventional XPS and UPS measurements is performed in ultra-high vacuum (around 10^{-8} to 10^{-10} mbar) for three main reasons. The ultra-high vacuum is impor-

tant because the low kinetic energy ejected photoelectrons can be easily scattered by gas molecules and, then, the noise present in the spectrum increases. Moreover, gas molecules can be adsorbed in the material's surface and change the properties of the sample during the spectrum acquisition. Furthermore, the electron analyser that detects the eject photoelectrons from the material only operates in ultra-high vacuum. Nowadays is already possible to perform APXPS (Ambient Pressure XPS) and NAP-XPS (Near Ambient Pressure XPS) measurements, that is, XPS measurements with the sample exposed to high temperatures and high pressure of the reactant gases or even XPS measurements with the sample in the liquid state. Previous work of the group [22, 56] used NAP-XPS and AP-XPS techniques and a detailed description of the techniques is given in [56].

A common electron analyser used is the hemispherical sector analyser (HSA) (Figure 3.2.5). This analyser consists of a pair of concentric hemispherical electrodes with a gap for the photoelectrons to pass through. An electric potential difference is applied between the inner and outer hemispheres to force the photoelectrons to describe a circular path. Only photoelectrons that present a given kinetic energy value are able to reach the multi-channel detector, which consists on the detectors arranged radially across the output plane. The HSA typically can operate in two modes: constant analyser energy (CAE) and constant retarded ratio (CRR). In the CAE mode, the photoelectrons are accelerated or retarded to fit an user-defined kinetic energy which is the energy that the photoelectrons must have when passing through the electron analyser in order to reach the multi-channel detector. This kinetic energy of the photoelectrons is called pass energy. The pass energy affects both the electron counts and the resolution of the analyser. The smaller the pass energy the higher the resolution and lower the transmission of electrons. On the other hand, the higher the pass energy the higher the transmission of electrons but the poorer the resolution. The pass energy remains constant throughout the energy range, threfore the resolution is constant across the entire width of the spectrum. In the CRR mode, similarly, electrons are retarded to fit a user-defined fraction of their original kinetic energy, called retard ratio, as they pass through the electron analyser. Therefore, the pass energy is proportional to the electron kinetic energy and the resolution becomes worse when the electron kinetic energy is increasing. However, the relative resolution is constant throughout the energy range.

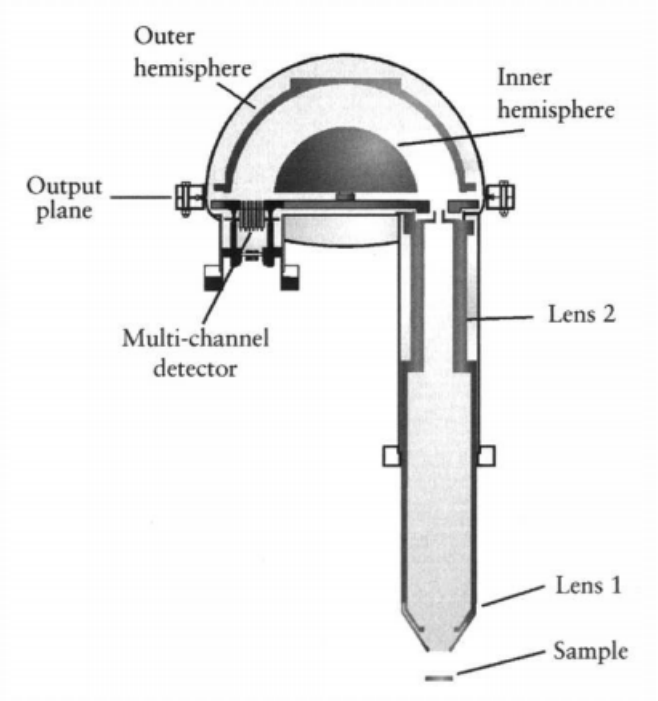

Figure 3.2.5 – Schematic of the hemispherical sector analyser (HSA). Figure obtained from [78].

3.3 X-ray Absorption Spectroscopy (XAS) Technique

The XAS technique [71,79] allows to obtain information about the electronic structure and to investigate the local atomic order around a specific atom. Therefore, by using this technique it is possible to obtain the oxidation state, the coordination number and structural disorder (Debye-Waller factor) of the atomic shells around the absorbing atom. The XAS technique consists in the measurement of the sample's X-ray absorption coefficient through the incidence of a monochromatic X-ray beam in the sample. The absorption spectrum shows the dependence of the absorption coefficient μ with the X-ray energy. This spectrum is described by the Beer-Lambert Law:

$$I = I_0 \, e^{-\mu t} \tag{3.5}$$

where I is the intensity of the radiation transmitted through the sample, I_0 is the intensity of the incident radiation in the sample and t is the thickness of the sample.

In a hypothetical case, if X-ray photons are incident on a single isolated atom, this atom can absorb a photon and then emit a photoelectron. The absorption spectrum in this case is presented in Figure 3.3.1(a). In this Figure it is possible to observe that when the incident photon energy ($h\nu$) is smaller than the electron binding energy (E_b) there is no absorption in this particular electronic level ($\mu = 0$). When the incident photon energy is equal to the electron binding energy there is an abrupt increase on the absorption

coefficient, giving the energy region named absorption edge. When the incident photon energy is greater than the electron binding energy the absorption continues with a given probability.

In a real case, there are neighbouring atoms around the absorbing atom. If the atom absorbs a photon and then emits a photoelectron, this photoelectron can be backscattered by the neighbouring atoms, as presented in Figure 3.3.1(b). Considering the photoelectron as a wave, it is emitted by the absorbing atom and is backscattered by the neighbouring atoms, then interfering with the incident wave. This interference can be constructive or destructive depending on the photoelectron wavelength, the distance from the absorbing atom to the scattering atom and the phase shift caused by the scattering event. If the interference is constructive (destructive) one can show that the absorption coefficient increases (decreases). This interference phenomenon gives rise to oscillations in the absorption spectrum after the absorption edge which contain structural information of the sample at the atomic level (Figure 3.3.1(b)).

The absorption spectrum comprehends two energy regions, the X-ray Absorption Near Edge Structure (XANES) region, which starts around 30 eV before the absorption edge and finishing around 50 eV after the absorption edge, and the Extended X-ray Absorption Fine Structure (EXAFS) region, which corresponds to the range of 50-1000 eV after the absorption edge (Figure 3.3.1(b)). The XANES region contains information about the atomic spatial geometry and the oxidation state of the absorbing atom while the EXAFS region contains information about the local atomic structure of the sample. Each region needs a different approach to be analysed.

In order to analyse each region of the absorption spectrum, first the spectrum is normalised. Two polynomials are used to perform this normalization. The first one is named pre-edge line and coincide with the spectrum region before the absorption edge. The second one is names post-edge line and is a polynomial that passes through the oscillations present at the region after the absorption edge (Figure 3.3.2(a)). By using these polynomials the edge height $\Delta\mu_0(E)$ is estimated and the absorption spectrum is normalised by this value. Then, the normalised absorption spectrum, shown in Figure 3.3.2(b), is obtained.

The amplitude of the EXAFS oscillations is much smaller than the absorption intensity at the absorption edge. In order to obtain a data with a high signal to noise ratio in this region, a X-ray source of high brilliance must be used to perform the measurement of the absorption spectrum. Because of that, this measurement is typically performed using a synchrotron light source [80–82]. The synchrotron radiation is generated when a charged particle with relativistic speed is deflected by a magnetic field, which is perpendicular to its direction of motion. This radiation presents advantageous characteristics like high brilliance, wide spectral range (from infrared to hard X-ray region), short time pulse (for time-resolved measurements), tunable polarization and small emittance. These character-

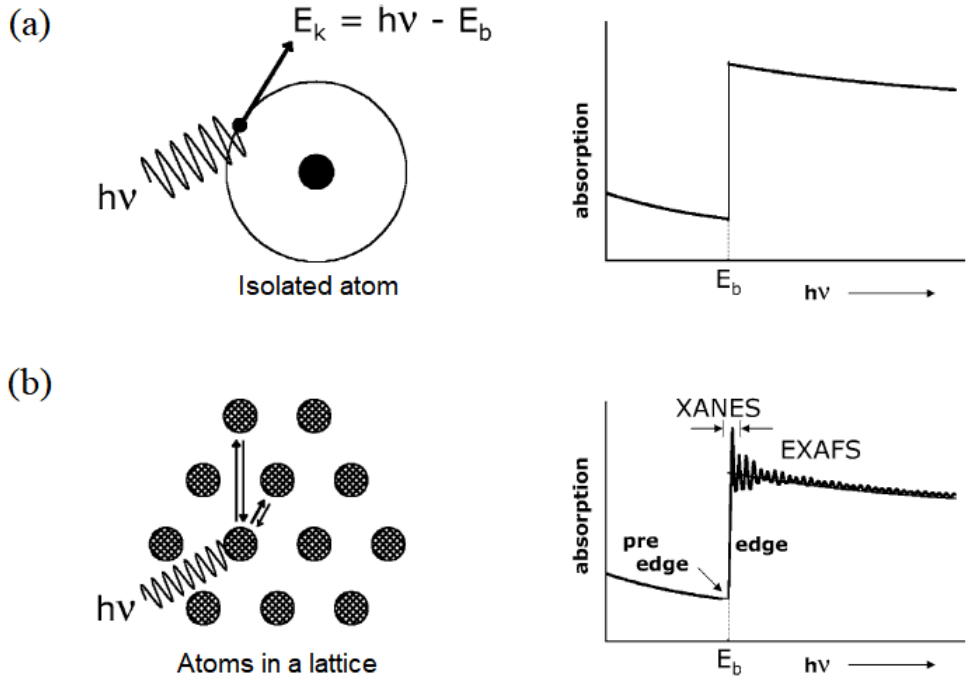

Figure 3.3.1 – Absorption spectrum as a function of the energy of the incident photon ($h\nu$) for (a) a single isolated atom (hypothetical case) and (b) an atom surrounded by neighbouring atoms (real case). Figure adapted from [71].

istics make the synchrotron light source an indispensable tool for material characterization in several studies nowadays.

There are three experimental modes to perform the measurement of the X-ray absorption spectrum: transmission, fluorescence and electrons detection. The transmission mode consists in focusing a X-ray beam in the sample and to measure the transmitted beam through the sample. The use of 3.5 allows to obtain the absorption coefficient of the sample. In general, the intensities I_0 and I are measured utilizing ionization chambers. The ionization chamber measures the intensity of the X-ray beam before it interacts with the sample (I_0) and another ionization chamber measures the intensity of the X-ray beam transmitted through the sample (I). The transmission mode is the preferred measurement mode, because it gives a better signal to noise ratio. However, for diluted or very thin samples, the signal to noise ratio obtained from transmission mode is not good enough and the preferred mode, in this case, is the fluorescence one. The fluorescence mode measurement consists on focusing the X-ray beam on the sample and to measure the emitted fluorescence lines. Usually, in order to perform this measurement, a solid-state Si or Ge detector is used, which allows to completely suppress the X-ray scatter contributions and other fluorescence lines, and to consider only the intensity of the fluorescence lines of interest. Since the material attenuates the X-rays emitted, the fluorescence intensity, and therefore the XAS signal, can be damped due to the self-absorption effect. Assuming that the sample is at 45° to both the incident beam and the fluorescence detector, the measured

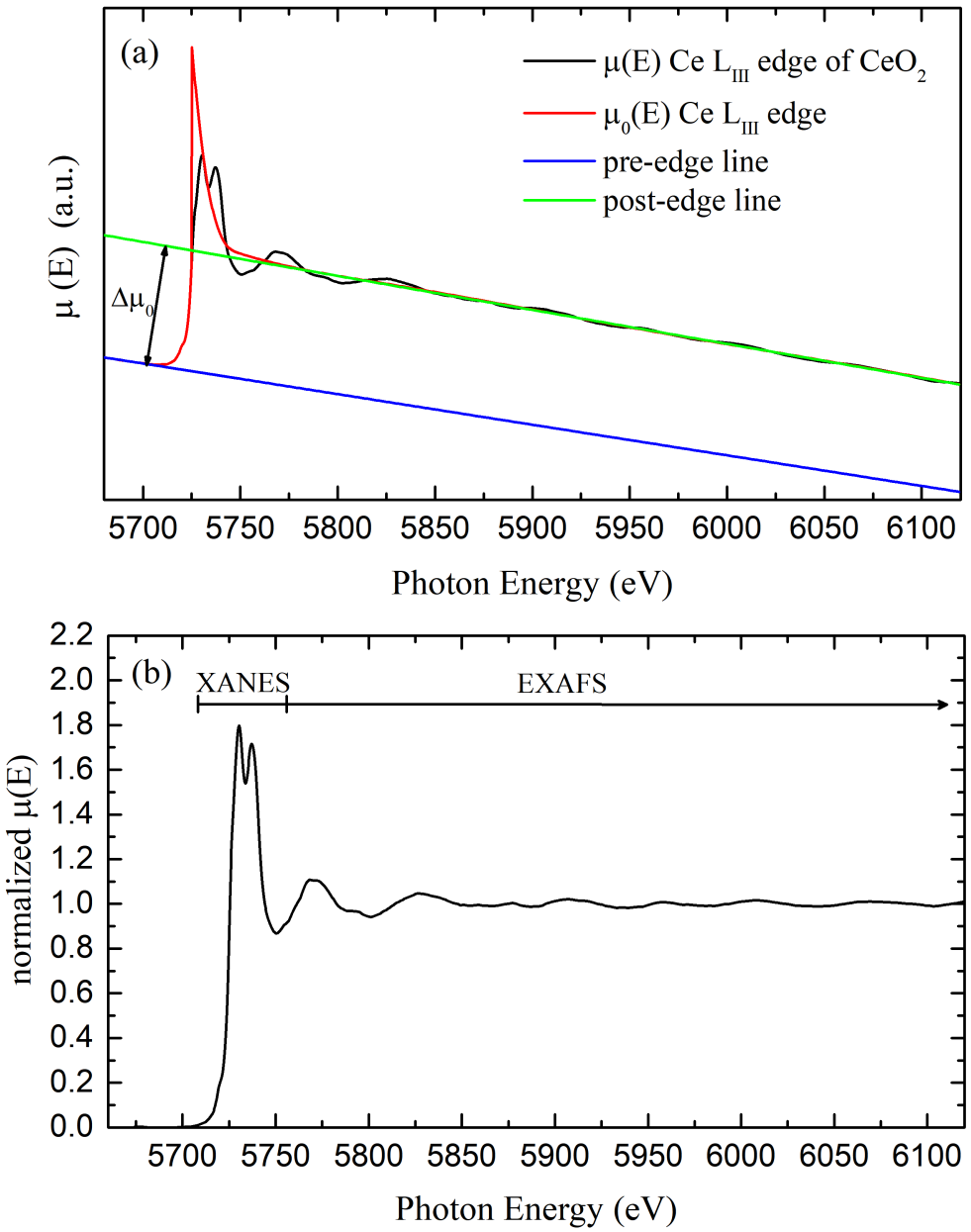

Figure 3.3.2 – (a) Absorption spectra at the Ce L_{III} edge (5723 eV) of a CeO_2 sample ($\mu(E)$) and of a single isolated Ce atom ($\mu_0(E)$). The pre-edge, post-edge lines and edge height $\Delta\mu_0(E)$ are shown as well. (b) Result of the absorption spectrum normalization of CeO_2. The XANES and EXAFS energy regions are shown.

fluorescence intensity (I_f) can be described as

$$I_f = I_0 \frac{\epsilon \Delta\Omega}{4\pi} \frac{\mu_\chi(E)}{\mu_{tot}(E) + \mu_{tot}(E_f)} [1 - e^{-(\mu_{tot}(E)+\mu_{tot}(E_f))t}] \tag{3.6}$$

where ϵ is the fluorescence efficiency, $\Delta\Omega$ is the detector solid angle, $\mu_\chi(E)$ is the absorption coefficient from the interest element, $\mu_{tot}(E)$ is the total absorption coefficient in

the sample, and E_f is the fluorescent X-ray energy. For diluted or very thin samples, the exponential in 3.6 can be approximate to $1 - (\mu_{tot}(E) + \mu_{tot}(E_f))t$. Then, 3.6 gives

$$\mu_\chi(E) \propto \frac{I_f}{I_0} \tag{3.7}$$

On the other hand, for concentrated or thick samples, that approximation can not be performed and the XAS signal will be severally damped by the self-absorption effect.

The electrons detection mode consists on focusing the X-ray beam on the sample and to detect the photoelectrons, Auger electrons and secondary electrons emitted from the sample. As presented for the fluorescence mode, it is possible to show that the absorption coefficient of the sample is proportional to the intensity of the photoelectrons, Auger electrons and secondary electrons emitted, where the major part of the signal is due to the secondary electrons generated. Since the escape depth for photoelectrons and Auger electrons is of the nanometer order, it makes this mode much more surface sensitive than the other modes.

3.3.1 X-ray Absoption Near Edge Structure (XANES)

The XANES energy region is close to the absorption edge, typically extending up to around 50 eV after the edge. This region contains structural and electronic informations of the sample, like the atomic spatial geometry and the oxidation state of the absorbing atom. The XANES signal after the absorption edge corresponds to electrons that were excited from atomic core levels to the continuum and to unoccupied electronic states. The allowed final electronic states are determined by the selection rules of the electric dipole

$$\Delta l = \pm 1 \tag{3.8}$$

$$\Delta j = \pm 1 \tag{3.9}$$

$$\Delta s = 0 \tag{3.10}$$

where l stands for the orbital angular momentum, j for the total angular momentum and s for the spin angular momentum [71]. The energy position of the absorption edge, which is defined as the energy position of the inflection point in this region, depends on the oxidation state of the sample. Moreover, the shape of the absorption edge depends on the chemical bounds present in the sample and can be used as a fingerprint of the chemical species. In some cases, a pre-edge can be observed in the spectrum. It receives this name because it appears before the absorption edge. The pre-edge is described by the electric dipole transitions and mainly by electric quadrupole transitions. It is an indicator of local site symmetry and orbital occupancy, and it contains information about hybridized states.

The description of the XANES region is more complex than the description of the EXAFS oscillations, because the kinetic energy of the photoelectrons corresponding to the XANES region is smaller. It gives the need of using a more complex potential than that used for the EXAFS region. In addition, the multiple scattering, that is more complex to be described than the single scattering, is much more common in the XANES region. Actually, there are some other methods to obtain information from this region. The most common method consists in adjusting the XANES region of the normalized absorption spectrum using a linear combination of normalized spectra of reference compounds. This method allows to obtain the oxidation state of the absorbing atom and even the amount of each compound present in the sample. The shape of the edge oscillations can be used as a fingerprint of chemical species because it depends on the chemical environment and kind of chemical bonding [71].

Since the XANES region is formed by electronic transitions to unoccupied electronic states or to the continuum, one can perform an adjust in the XANES region by using lorentzian and arctangent functions. The lorentzian functions describe the electronic transitions to unoccupied electronic states close to the Fermi level while the arctangent function describes the electronic transitions to continuum. Using this method it is possible to obtain information about the oxidation state and about the occupancy of a particular electronic state of the absorbing atom.

3.3.2 Extended X-ray Absorption Fine Struture (EXAFS)

The EXAFS region is the energy region in the range of 50-1000 eV after the absorption edge. This region contains structural information about the sample, like the coordination number around the absorbing atom, the distance from the absorbing atom to the scattering atoms and information about the thermal and structural atomic disorder. In order to obtain the structural information from the EXAFS region it is necessary to analyse the EXAFS oscillations. Aiming to do that, the single atom contribution ($\mu_0(E)$) (Figure 3.3.2) is removed from the absorption spectrum and the EXAFS oscillations, $\chi(E)$, are obtained.

Since the EXAFS oscillations are formed by an interference effect, which depends on the wave behaviour of the photoelectron, it is convenient to treat these oscillations as a function of the wavenumber of the photoelectrons, k, rather than the photon energy of the incident X-ray. Therefore, the following transformation is performed:

$$k = \sqrt{\frac{2m(E - E_b)}{\hbar^2}} \tag{3.11}$$

where E_b and m are the electron binding energy and the electron rest mass, respectively. Using this transformation, the EXAFS oscillations, $\chi(k)$, are obtained. Aiming to evidence

the oscillations in the region of high wavenumber, the oscillations $\chi(k)$ can be weighted by k, k^2 or k^3, depending on the case. Figure 3.3.3(a) presents the $k^2\chi(k)$ oscillations of the absorption spectrum at the Ce L_{III} edge of a CeO_2 sample.

The EXAFS oscillations can be described as:

$$\chi(k) = \sum_j \frac{N_j S_0^2 e^{-2k^2\sigma_j^2} e^{\frac{-2R_j}{\lambda_{IMFP}(k)}} f_j(k)}{kR_j^2} \sin[2kR_j + \delta_j(k)] \tag{3.12}$$

where j represents the number of the atomic shell around the absorbing atom, N_j is the coordination number of the j^{th} shell, S_0^2 is the correction for relaxation effects in the absorbing atom, σ_j^2 is the Debye-Waller factor, $\lambda_{IMFP}(k)$ is the photoelectron inelastic mean-free path, $f_j(k)$ is the scattering amplitude with the atoms at the j^{th} shell, $\delta_j(k)$ is the scattering phase shift with an atom at the j^{th} shell and R_j is given by $R_j = R_0 + \Delta R$, where R_0 is the theoretical distance from the absorbing atom to the scattering atom and ΔR is the change on the R_0 distance.

The term $e^{\frac{-2R_j}{\lambda_{IMFP}(k)}}$ represents the intensity attenuation when the electron travels through the solid, which depends on the photoelectron inelastic mean-free path $\lambda_{IMFP}(k)$. The term $e^{-2k^2\sigma_j^2}$ represents the thermal and structural disorder of the measured material. The dependence of the $\chi(k)$ on $\frac{1}{R_j^2}$ reflects that the outgoing electron is a spherical wave and its intensity decreases with the square of the distance.

The $f_j(k)$ and $\delta_j(k)$ parameters of the equation 3.12 are determined by *ab initio* calculations. The R_0 parameter is known by the crystallographic data. The $\lambda_{IMFP}(k)$ is obtained from the TPP-2M formula [77]. The other parameters (S_0^2, N_j, σ_j^2 and ΔR) can be obtained from the fitting procedure. The potential used to perform the calculations is based on the *muffin-tin* approximation, where the potential is assumed to be spherically symmetric in the region close to the atomic nucleus and constant in the region between the atoms (interstitial region) [83]. The real potential in the interstitial region is more complex than that considered by the *muffin-tin* approximation, due to metallic, ionic or covalent bondings. However, the kinetic energy of the photoelectrons at the EXAFS region is sufficiently high for considering the photoelectrons moving almost free in the interstitial region. Therefore, the *muffin-tin* approximation suffices for the analysis at the EXAFS region.

Aiming to describe the single and multiple scattering events and to avoid the calculations of wave functions, the description of the X-ray absorption spectrum can be done using the complete Green's function G defined by

$$G = \frac{1}{E + i\epsilon - H} \tag{3.13}$$

where H is the single-particle electron's Hamiltonian and ϵ represents the lifetime of the photoelectron. By using a spectral representation of the Green's function in the positional space

$$G(\mathbf{r}, \mathbf{r}_f; E) = \sum_f |\psi(\mathbf{r}_f)\rangle \frac{1}{E + i\epsilon - H_f} \langle\psi(\mathbf{r}_f)| \tag{3.14}$$

the absorption coefficient for a given core level $\psi(r_f)$ can the written as

$$\mu_c = -\frac{1}{\pi} Im \, \langle\psi_c|\hat{\epsilon} \cdot \mathbf{r} G(\mathbf{r}, \mathbf{r}_f; E) \hat{\epsilon} \cdot \mathbf{r}_f|\psi_c\rangle \, \theta_\epsilon(E - E_F) \tag{3.15}$$

where $\theta_\epsilon(E - E_F)$ is a broadened step function at the Fermi energy E_F. The *muffin-tin* approximation for the potential allows to write the Hamiltonian H_f as

$$H_f = E_k + U_a + \sum_{n \neq a} U_n \tag{3.16}$$

where E_k is the photoelectron kinetic energy, U_a is the potential of the ionized atom A in its fully relaxed state and $\sum_{n \neq a} U_n$ is the sum of all the potentials from the neighbouring atoms that affect the photoelectron motion. From this approximation it is possible to rewrite the absorption coefficient as

$$\mu_c = -\frac{1}{\pi} Im \, \langle\psi_c|\hat{\epsilon} \cdot \mathbf{r}[G_a + G_a \tau G_a] \hat{\epsilon} \cdot \mathbf{r}_f|\psi_c\rangle \, \theta_\epsilon(E - E_F) \tag{3.17}$$

where G_a is the Green's function belonging to the potential U_a

$$G = \frac{1}{E + i\epsilon - E_k - U_a} \tag{3.18}$$

and τ is the complete scattering operator.

$$\tau = \sum_{\substack{n \neq a \\ n \neq j}} U_n + \sum_{n \neq a} U_n G \sum_{m \neq j} U_m \tag{3.19}$$

The term that contains G_a in 3.17 corresponds to the absorption coefficient for the photoemission from the isolated atom A. The term that contains $G_a \tau G_a$ represents all the contributions to the absorption coefficient due to single and multiple scatterings events suffered by the photoelectron in the material. Therefore, this description allows to separate

the contribution from the isolated atom emission from the single and multiple scatterings events of the photoelectron in the neighbourhood of atom A. Moreover, using the perturbation theory, by applying the identity $U_n G_n = t_n G_0$, where t_n is the operator for the scattering of the photoelectron from the isolated atom N,

$$t_n = U_n + U_n G_n U_n \tag{3.20}$$

and G_0 is the free-space Green's function,

$$G_0 = \frac{1}{E + i\epsilon - E_k} \tag{3.21}$$

it is possible to rewrite 3.19 as

$$\begin{aligned} \tau = \sum_{n \neq a} t_n + \sum_{n \neq a} t_n G_0 \sum_{\substack{m \neq n \\ m \neq a}} t_m + \sum_{n \neq a} t_n G_0 \sum_{m \neq n} t_m G_0 \sum_{\substack{k \neq m \\ k \neq a}} t_k \\ + \sum_{n \neq a} t_n G_0 \sum_{m \neq n} t_m G_0 \sum_{k \neq m} t_k G_0 \sum_{\substack{j \neq k \\ j \neq a}} t_j + ... \end{aligned} \tag{3.23}$$

Replacing 3.23 in 3.17 one can see that the generic term of the multiple scattering expansion of the absorption coefficient has the following closed-loop structure: after emission from the atom A, the complete propagator G_a brings the photoelectron to the atom J, the photoelectron is scattered there (t_j) and propagates to the atom K in free space (G_0). Therefore, the expression obtained represents the absorption coefficient as a sum of all possible scattering events, single and multiple, which gives rise to the structure that is observed on the EXAFS region of the absorption spectrum.

In order to obtain information from the EXAFS oscillations, usually, a Fourier transform (FT) of these oscillations is performed. A k-interval (Δk) is used to perform this transform, as shown in Figure 3.3.3(a) for the $k^2\chi(k)$ EXAFS oscillations obtained from XAS spectrum shown in Figure 3.3.2(b). The FT can be interpreted as the absorbing atom in the position $R = 0$, thus each contribution corresponds to the single or multiple scattering of the ejected photoelectron that is caused by the atoms present around the absorbing atom. In this way, it becomes easier to visualize the neighbouring atoms contributions to the EXAFS oscillations $\chi(k)$. Figure 3.3.3(b) presents the Fourier transform of the EXAFS oscillations $k^2\chi(k)$ shown in Figure 3.3.3(a). In Figure 3.3.3(b) is possible to observe the identification of the contributions that correspond to single scattering events.

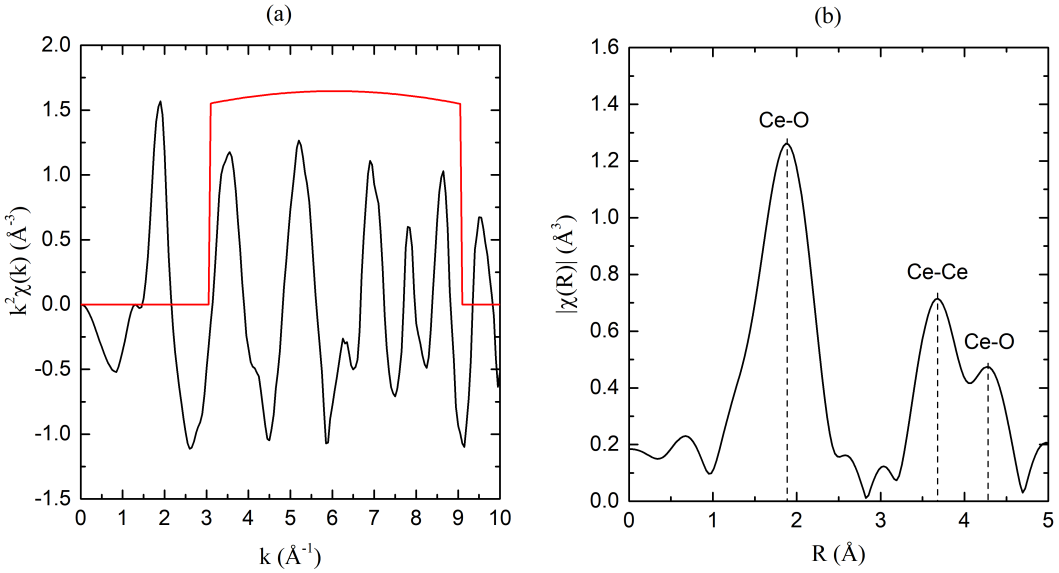

Figure 3.3.3 – (a) k^2-weighted and (b) the corresponding FT of the EXAFS oscillations $\chi(k)$ of CeO_2 with the identification of peaks that correspond to single scattering events. The red line shows the k-interval used to perform the Fourier transform.

3.4 Density Functional Theory (DFT)

The DFT [84–86] is an alternative approach to the Schrodinger's equation to calculate the ground state of a many-electrons system, in which the fundamental role is played by the electronic density distribution rather than the many-electron wave function. Then, a system with N electrons that would be treated by the Schrodinger's equation with a 3N variables wave function can be treated as an equation of the electronic density with only three variables. The DFT is widely used in chemistry and materials science for the investigation of complex systems at atomic scale and it showed to be one of the most efficient methods to calculate structural and electronic properties of the ground state of a material.

The DFT has two theorems demonstrated by Hohenberg and Kohn [84]. Considering a system with N electrons where $r_i = (x_i, y_i, z_i)$ is the position vector of the i^{th} electron:

Theorem 3.1. *The external potential $v(\boldsymbol{r})$ felt by the electrons is an unique functional of the electronic density $\rho(\boldsymbol{r})$.*

Theorem 3.2. *The density $\rho(\boldsymbol{r})$ that minimises the total energy $E_0[\rho]$ is the exact ground-state density,*

$$E[\rho] = \langle\psi|\hat{E}_k + \hat{U} + \hat{V}|\psi\rangle \tag{3.24}$$

where $\hat{E}_k$ is the kinetic energy operator, $\hat{U}$ is the potential energy operator, $\hat{V}$ is the electron-electron interaction energy operator.

It is convenient to separate from the universal functional $E_0[\rho]$ the classic coulombic part $F[\rho]$, then

$$E[\rho] = \int v(\mathbf{r})\rho(\mathbf{r})d^3r + \frac{1}{2}\int\int \frac{\rho(\mathbf{r})\rho(\mathbf{r}')}{|\mathbf{r}-\mathbf{r}'|}d^3rd^3r' + G[\rho] \tag{3.25}$$

and

$$F[\rho] = \frac{1}{2}\int\int \frac{\rho(\mathbf{r})\rho(\mathbf{r}')}{|\mathbf{r}-\mathbf{r}'|}d^3rd^3r' + G[\rho] \tag{3.26}$$

where the first term of 3.25 is the kinetic energy of the electrons interacting with an external static potential $v(\mathbf{r})$, the second term of 3.25 correspond to the coulomb potential energy, and $G[\rho]$ is also an universal functional. The $G[\rho]$ functional can be written as

$$G[\rho] \equiv E_{k0}[\rho] + E_{xc}[\rho] \tag{3.27}$$

where $E_{k0}[\rho]$ is the kinetic energy of a non-interacting system of electrons with density $\rho(\mathbf{r})$. $E_{xc}[\rho]$ contains the exchange and correlation energies of an interacting system with electronic density $\rho(\mathbf{r})$. The exact form of the $E_{xc}[\rho]$ functional is not even know, but can be approximated.

Using the variational principle to $E[\rho]$ and considering the constraint

$$\int \rho(\mathbf{r})d^3r = N \tag{3.28}$$

one can obtain the following equations:

$$(-\frac{1}{2}\bigtriangledown^2 + v^{KS}[\rho])\psi_i(\mathbf{r}) = \epsilon_i\psi_i(\mathbf{r}) \tag{3.29}$$

$$\rho(\mathbf{r}) = \sum_{i=1}^{N} |\psi_i(\mathbf{r})|^2 \tag{3.30}$$

$$v^{KS} = v(\mathbf{r}) + \int \frac{\rho(\mathbf{r}')}{|\mathbf{r}-\mathbf{r}'|}d^3r' + v_{xc}(\rho) \tag{3.31}$$

where $v_{xc}(\rho) = \frac{\delta E_{xc}}{\delta \rho}$ is the local exchange-correlation potential. These self-consistent equations are called Kohn-Sham (KS) equations [85] and can be used to obtain the electronic density of the system iteratively. Calculating the electronic density, the system ground state energy can be obtained from

$$E = \sum_i \epsilon_i + E_{xc}[\rho(\mathbf{r})] - \int v(\mathbf{r})\rho(\mathbf{r})d^3r - \frac{1}{2}\int\int \frac{\rho(\mathbf{r})\rho(\mathbf{r}')}{|\mathbf{r}-\mathbf{r}'|}d^3r d^3r' \tag{3.32}$$

The simplest approximation for $E_{xc}[\rho(\mathbf{r})]$ is the local-density approximation (LDA). In this approximation the exchange-correlation energy of a system of homogeneous electron gas of density $\rho(\mathbf{r})$ in the point $\mathbf{r}$ is assumed equal to the exchange-correlation energy of a homogeneous electron gas with the same density. Separating the exchange and correlation contributions it is possible to consider a term for the exchange (ϵ_x) and a term for the correlation (ϵ_c) contribution. Then, the E_{xc}^{LDA} can be written as

$$E_{xc}^{LDA}[\rho(\mathbf{r})] = \int \rho(r)[\epsilon_x(\rho(\mathbf{r})) + \epsilon_c(\rho(\mathbf{r}))]d^3r \tag{3.33}$$

The exchange part is given, in atomic units, by

$$\epsilon_x(\rho) = -\frac{0.458}{r_s} \tag{3.34}$$

where r_s is the Wigner radius that can be obtained from $\rho(\mathbf{r}) = \frac{3}{4\pi}\frac{1}{r_s^3}$. The correlation part is more complex and cannot be determined exactly. This term was estimated at the first time by Wigner in 1938 [87] and is given, in atomic units, by

$$\epsilon_c(\rho) = -\frac{0.44}{r_s + 7.8} \tag{3.35}$$

The LDA approximation gives extremely useful results for most applications. It gives a very good accuracy (around 1 %) when calculating bond lengths and geometries of molecules and solids and gives a fair accuracy of 10 % to 20 % when calculating ionization energies of atoms, dissociation energies of molecules and cohesive energies.

Some systems constituted, usually, by transition metals or rare earth elements that present localized electrons in the d or f orbitals are not well described by the DFT calculations. This happens because these localized electrons constitute "strongly correlated" electronic states and, to perform calculations with these systems properly, a correction in the energy functional should be considered. In this correction, which is based on the

Hubbard model and is called DFT+U [88–90], the strength of the on-site interactions are described by two parameters: U, which reflects the strength of the on-site Coulomb interaction, and J, which adjusts the strength of the exchange interaction. However, if the system calculated is rotationally invariant and has the high order terms of the Coulomb interaction neglected, a simpler form of this correction, proposed by Anasimov et al. [90], can be used. The correction uses the two parameters U and J combined in a single effective parameter $\mathrm{U}_{eff} = U - J$ that accounts for the Coulomb interaction. This simpler form is given by

$$E_{DFT+U} = E_{DFT} + \sum_i \frac{U_{eff}}{2} Tr(n^i - n^i n^i) \tag{3.36}$$

where n^i is the atomic orbital occupation matrix.

4 Experimental and Theoretical Procedure

This chapter is dedicated to describe the experimental and theoretical procedures and the data analysis used in each step of the work. The H_2 evolution photocatalytic activity measurements, the sample's characterization using UV-Vis, XRD, XPS, UPS, FTIR and XAS techniques and the theoretical procedure using DFT calculations will be described in details.

In order to perform the proposed study, 9 different CeO_2 samples were used, including the CeO_2 commercial standard. The other 8 samples were synthesized following the procedure presented in [22] in collaboration with Prof. Fernanda Poletto from Instituto de Química at UFRGS. Table 4.1 presents the main characteristics of the samples used in this work. The different samples were synthesized by the precipitation method using ceric ammonium carbonate as precursor and varying the synthesis temperature, precursor concentration, and the quantity of water and/or ethanol in the process. It is possible to observe in Table 4.1 that all samples are constituted by CeO_2 particles with nanometric size. Some samples present more than one value of mean diameter. This indicates that these samples present a multimodal size distribution and, therefore, each value of mean diameter shown in Table 4.1 corresponds to one mode. The surface area values were obtained from the N_2 adsorption-desorption isotherms measurements utilizing the Brunauer, Emmett and Teller (BET) multipoint technique.

Sample	Surface Area (m^2/g)	Pore Volume (mm^3/g)	Mean Diameter (nm)
1	138	52	13 ± 3
			44 ± 21
			90 ± 18
2	130	37	13 ± 15
3	104	32	15 ± 21
			26 ± 12
4	126	127	6 ± 3
5	165	132	22 ± 12
			63 ± 35
6	137	57	11 ± 6
7	170	91	3 ± 3
8	201	129	3 ± 2
Standard	38	104	26 ± 24

Table 4.1 – Samples used in this work and their respective surface area, pore volume and mean diameter obtained from [22]. The uncertainty associated to the surface area and pore volume values are, respectively, 5 m^2/g and 2 mm^3/g.

Figure 4.0.1 was obtained from the previous work [22] and presents the pore size distributions obtained from the N_2 adsorption-desorption isotherms measurements using the BJH (Barret, Joyner and Halenda) and DFT (mean field Density Functional Theory) methods for all the nanoparticles synthesized. It is possible to observe that all the samples present micropores regions (pores diameter smaller than 2 nm [91]) and only the samples 6, 7 and 8 present mesopores regions (pores diameter between 2 nm and 50 nm [91]). Some samples present a mean pore size as large as the nanoparticle mean diameter. However, it is important to notice that there is a distribution of nanoparticle diameter and pore size for each sample, in such a way that the pore size is always smaller than the nanoparticle diameter.

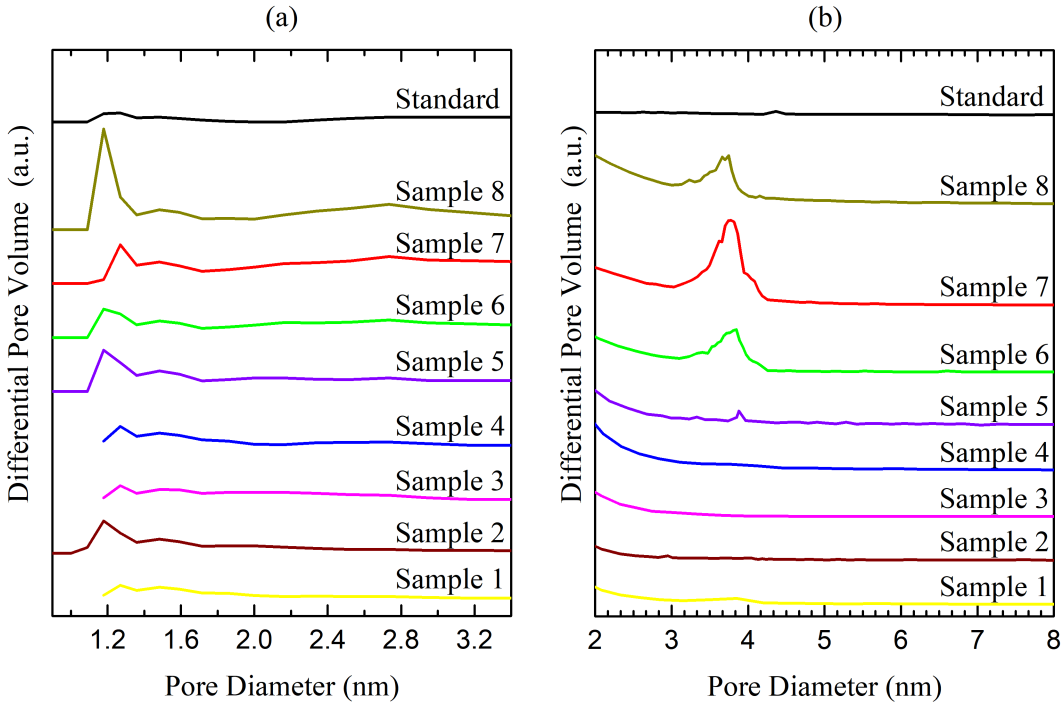

Figure 4.0.1 – Pore size distributions obtained using the (a) BJH (Barret, Joyner and Halenda) and (b) DFT methods. Figure adapted from [22].

4.1 Experimental Procedure

4.1.1 H_2 Evolution Photocatalytic Activity Measurements

The H_2 evolution photocalytic activity measurements were performed in the Instituto de Física at UFRGS using a quartz reactor with a volume of around 52 ml, presented in Figure 4.1.1. A 300 W Xe lamp (CERMAX LX300, $\lambda > 200$ nm) was used to simulate the solar spectrum. A gas chromatography system (GC System 6820, Agilent Technologies) equipped with a thermal conductivity detector (TCD) and an Ar carrier was used to detect the H_2 yield produced. 10 mg of CeO_2 nanoparticles powder was dispersed in 7.5

ml of deionised water inside the reactor using an ultrasonic device during 30 minutes. Then, 2.5 ml of ethanol, used as sacrificial agent was added, resulting in a solution of 1 mg/ml of nanoparticles. Aiming to reduce the amount of O_2 gas inside the reactor before starting the photocatalytic reaction, an Ar flux and a vacuum pump were used. The amount of O_2 gas inside the reactor was measured taking 50 μl of gas from the reactor and injecting on the GC system. A calibration curve was used to convert the O_2 signal presented by the GC to the amount of the O_2 gas present in the volume. The goal was to decrease the amount of O_2 gas to less than 0.2 μmol inside the reactor, by replacing it with Ar, which is an inert gas. After that, the reactor was irradiated by the Xe lamp, which simulates the solar light, operating at 75 % of its maximum power, that gives a 225 W power, while the solution was stirred magnetically. The reactor was maintained at 25 °C by a water cooling flow system. The value of the H_2 yield was determined by taking 300 μl of gas from the reactor every 15 minutes of reaction and using the GC system to analyse this gas.

Figure 4.1.1 – Pictures of the quartz reactor used to perform the H_2 evolution photocatalytic activity measurements. The pictures present the quartz part and the stainless steel part used to seal up the reactor.

4.1.2 Ultraviolet-visible (UV-Vis) Spectroscopy Measurements

The UV-Vis spectroscopy measurements were performed in the Instituto de Química at UFRGS in order to obtain the direct and indirect band gap energies of the nanoparticles synthesized. A Shimadzu UV-Vis spectrophotometer was used to obtain the absorption spectra of the CeO_2 nanoparticles. The measurements were performed with around 5 mg of each sample in the powder form. The absorption spectra consists in the absorption coefficient (α) of the nanoparticles as a function of the incident radiation wavelength. All

samples were measured in the incident radiation wavelength range from 200 nm to 800 nm.

4.1.3 X-ray Diffraction (XRD) Measurements

The XRD measurements were performed in the Centro de Nanociência e Nanotecnologia (CNANO) at UFRGS in order to identify the crystalline phases present in the nanoparticles and to obtain information about the lattice parameter and the O occupancy values using the Rietveld analysis. Before performing the measurements the samples were sieved using a 48 μm size sieve. A X-ray diffractometer (Rigaku Ultima IV) working at the Bragg-Brentano geometry at 40 kV and 17 mA with a Cu Kα radiation source (1.5405 Å) was used. The measurements were performed in the 2θ range from 20° to 90° with a step size of 0.05° with an acquisition time of 4.5 s/point.

4.1.4 X-ray Absorption Spectroscopy (XAS) Measurements

The XAS measurements were performed at the D08B-XAFS2 beamline of LNLS (Brazilian Synchrotron Light Source) [92] in transmission mode at the Ce L_{III} edge (5723 eV). For the measurements, about 5 mg of the nanoparticle powder was used to produce an homogeneous thin membrane supported on PVDF (polyvinylidene difluoride). Aiming to produce these membranes, the nanoparticles powder was sieved using a nylon mesh. Then, 5 mg of the nanoparticles powder was dispersed in isopropyl alcohol utilizing an ultrasound device, resulting in a homogeneous solution. A clean membrane was fixed between a glass funnel and a glass tube using a grapple (Figure 4.1.2). The solution was dropped inside the glass tube and, with the help of a vacuum pump attached to the glass funnel, passed through the membrane forming a thin layer of the nanoparticle powder on the membrane. Lastly, the membrane was fixed on the sample holder. The absorption spectra were collected at room temperature and at ambient pressure using a Si(111) double-crystal monochromator and three ionization chambers filled with Ar gas. The average time interval between spectra was around 40 min. The absorption spectra of commercial CeO_2 and $CeOHCO_3$ compounds were used as Ce(IV) and Ce(III) standards, respectively. A Cr foil was used as reference to calibrate the beamline energy.

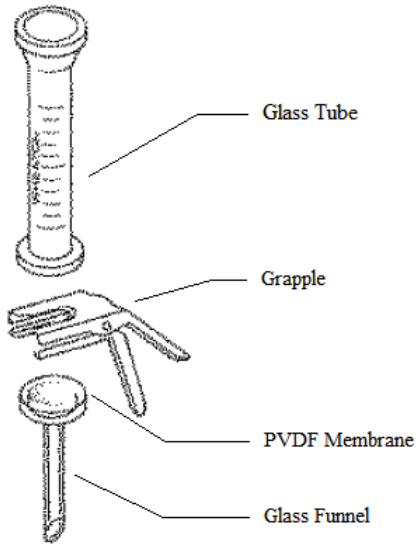

Figure 4.1.2 – Illustration of the system utilized to produce the membranes used in the XAS measurements.

4.1.5 Fourier Transform Infrared (FTIR) Spectroscopy Measurements

The FTIR spectroscopy measurements were performed in the Central Analítica of Instituto de Química at UFRGS in order to determine qualitatively of the organic compounds present in the CeO_2 nanoparticles surface. For the measurements, about 0.1 mg of the nanoparticle powder was mixed with 100 mg of KBr powder, and this mixture was compacted to produce homogeneous pellets. The measurements were performed at room temperature using a FTIR spectrophotometer (Shimadzu IRPrestige-21) in transmittance mode to obtain the FTIR spectra in the wavelength range from 4000 cm^{-1} to 400 cm^{-1} with a resolution of 2 cm^{-1}.

4.1.6 X-ray Photoelectron Spectroscopy (XPS) and Ultraviolet Photoelectron Spectroscopy (UPS) Measurements

The XPS and UPS measurements were performed in collaboration with Prof. Edmar Avellar Soares in the Instituto de Ciências Exatas of Departamento de Física at UFMG. For the measurements, a thin layer of the nanoparticles powder was dispersed on a carbon tape, placed in the sample holder, and exposed to an ultra high vacuum (UHV) condition inside the analysis chamber. The base pressure inside the chamber during the measurements was around 5.0×10^{-9} mbar. The XPS measurements were performed at room temperature utilizing a Mg Kα X-ray source (1253.6 eV). The XPS measurements were performed at the Long Scan, Ce 3d, O 1s, and C 1s regions. The electron analyzer (PHOIBOS HSA3500 CCD 100 R6-HiRes) was set at a pass energy of 60 eV for the long scan and 30 eV for the high resolution scans, and the energy step was 1.0 eV for the long scan and 0.1 eV for the high resolution scans, with an acquisition time of 100

ms/point. After this, the nanoparticles were heated to 120 °C in UHV (pressure $\sim 5.0 \times 10^{-9}$ mbar). At 120 °C, this temperature was maintained for 10 h, when the system was cooled to room temperature in UHV. This treatment was performed in order to clean the nanoparticles surface of organic compounds. The new XPS measurements, after heating treatment, were performed at room temperature using the Long Scan, Ce 3d, Ce 4d, O 1s, and C 1s regions. The Ce 3d and Ce 4d regions were probed intending to obtain the Ce oxidation state at different depths.

The UPS measurements were performed in the same system using a He II (40.8 eV) lamp after the thermal treatment in UHV at 120 °C for 10 h in order to probe the valence region of the first atomic layers of the nanoparticles. The sample preparation was performed in the same way than that in the XPS measurements. The electron analyzer (PHOIBOS HSA3500 CCD 100 R6-HiRes) was set at a pass energy of 4 eV, and the energy step was 0.1 eV, with an acquisition time of 50 ms/point.

4.2 Data Analysis

4.2.1 Ultraviolet-visible (UV-Vis) Spectroscopy Analysis

In order to determine the direct and indirect band gap energies of the CeO_2 nanoparticles, the UV-Vis spectra were analysed using the method proposed by Tauc, David and Mott [93–95]. This method uses the fact that the absorption edge of the UV-Vis spectrum can be described approximately as

$$(h\nu\ \alpha)^{\frac{1}{n}} = A(h\nu - E_g) \tag{4.1}$$

where $h\nu$ is the energy of the incident radiation, α is the radiation absorption coefficient, E_g is the band gap energy, and A is a proportional constant. The n is a value that depends on the nature of the electronic transition: $n = \frac{1}{2}$ for a direct allowed transition, $n = \frac{3}{2}$ for a direct forbidden transition, $n = 2$ for an indirect allowed transition, $n = 3$ for an indirect forbidden transition. Aiming to determine the band gap energy of a specific transition, the vertical axis of the UV-Vis spectrum, which contains the radiation absorption coefficient, was multiplied by the energy of the incident radiation $h\nu$ in eV and powered by $\frac{1}{n}$ resulting in $(h\nu\ \alpha)^{\frac{1}{n}}$. The horizontal axis was transformed from $\lambda(nm)$ to $h\nu$ in eV. After these transformations, the UV-Vis spectrum is presented as the $(h\nu\ \alpha)^{\frac{1}{n}}$ coefficient as a function of $h\nu$ (Figure 4.2.1). It is possible to observe an approximately linear region in this spectrum which corresponds to the absorption edge of the UV-Vis spectrum. The band gap energy of a specific transition, determined by the n value, can be obtained by fitting a straight line in this region, containing its inflection point. E_g is the value where this straight line crosses the $h\nu$ horizontal axis. Figure 4.2.1 presents an

example of this procedure to determine the direct allowed bang gap ($n = \frac{1}{2}$) energy value of the standard sample.

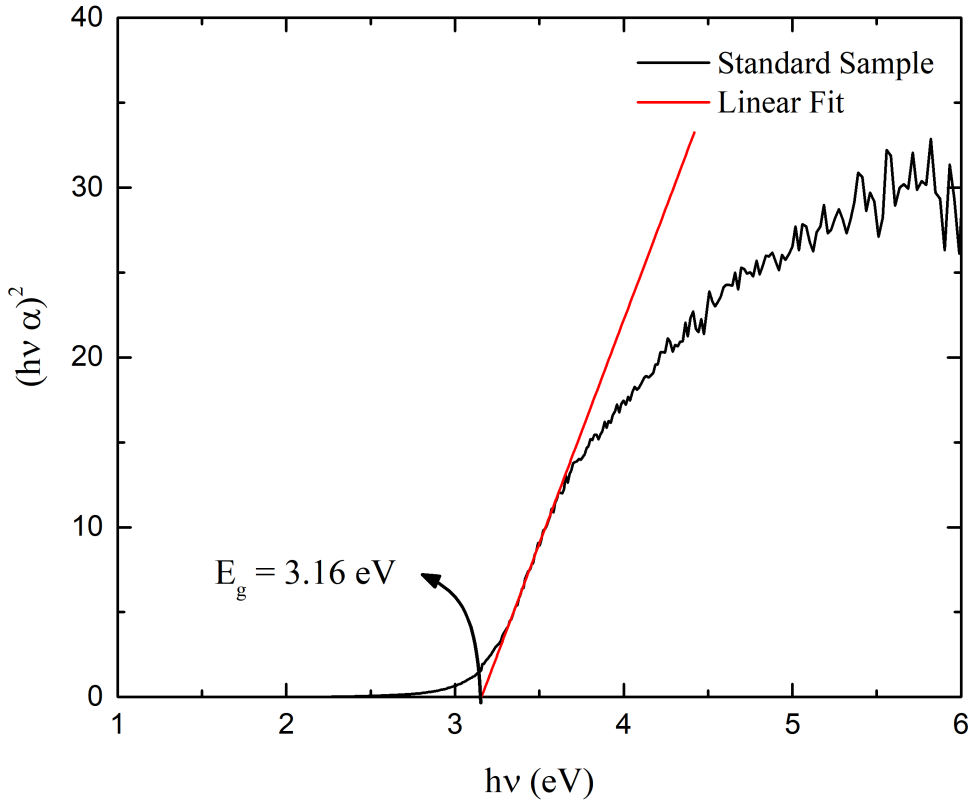

Figure 4.2.1 – Determination of the direct allowed bang gap energy value of the standard sample using the method proposed by Tauc, David and Mott [93–95]. The black line correspond to the $(h\nu\ \alpha)^2$ value as a function of $h\nu$ obtained from the UV-Vis spectrum. The red line is the straight line fitted on the approximately linear region which gives the absorption edge of the UV-Vis spectrum.

In order to obtain the best fit of the straight line on the approximately linear region and to obtain the band gap energy for each sample, several different initial and final $h\nu$ points close to the inflection point were used. For a given sample, the E_g value found always varied less than 1 % of the value in this procedure. The procedure described above was used to determine the direct ($n = \frac{1}{2}$) and indirect ($n = 2$) band gap energies of all the CeO_2 nanoparticles.

4.2.2 X-ray Diffraction (XRD) Analysis

In order to determine the crystalline phases and to identify the Bragg reflections present in the diffractogram of each sample, the Crystallographica Search Match software version 2.1 and the JCPDS-ICDD database were used. Aiming to obtain information about the lattice parameter, crystallite size, strain and O occupancy for each sample, the diffractograms were analysed with the Fullprof software-Fullprof Suite version of july-2017 using the Rietveld refinement method [96, 97]. This method consists of refining a crystal structure by minimizing the function

$$\chi^2 = \sum_{i=1}^{Npoints} w_i (I_i^{exp} - I_i^{calc})^2 \tag{4.2}$$

where I_i^{exp} is the intensity of the i^{th} point of the XRD pattern measured, I_i^{calc} is the intensity of the calculated pattern of the i^{th} point and $w_i = \frac{1}{\sigma_i^2}$, where σ_i^2 is the variance of the I_i^{exp}. The I_i^{calc} is given by

$$I_i^{calc} = \sum_{j=1}^{Nphases} S_j \sum_{k=1}^{Npeaks} L_k J_k |F_{k,j}|^2 \Omega_j (2\theta_i - 2\theta_{k,j}) P_{k,j} A_j + bkg_i \tag{4.3}$$

where

- S_j is the scale factor.
- L_k is the Lorentz-Polarization factor which depends on the measurement equipment configuration.
- J_k is the Multiplicity factor which depends on the crystalline structure of the sample.
- $P_{k,j}$ is the preferred orientation function.
- A_j parameter corresponds to the absorption correction.
- $F_{k,j}$ is the structure factor for each phase and Bragg reflection which is given by

$$F_{k,j} = \sum_{n=1}^{Natoms} O_n f_n e^{-B_n \frac{\sin^2\theta}{\lambda^2}} [e^{2\pi i (hx_n + ky_n + lz_n)}] \tag{4.4}$$

where O_n is the occupation factor, which depends on the atom occupancy, f_n is the atomic scattering factor, B_n is the isotropic temperature parameter, λ is the wavelength of the incident radiation, x_n, y_n, z_n are the coordinates of the nth atom and h, k, l are the Miller indexes.

- $\Omega_j(2\theta_i - 2\theta_{k,j})$ function corresponds to the reflection profile function that models both instrumental and sample effects, which determines the shape of the Bragg reflections. In order to obtain the domain crystallite size and strain of the nanoparticles, the Thompson-Cox-Hastings pseudo-Voigt Axial divergence asymmetry [98,99] profile function was used in this work.

- bkg_i correspond to the background contribution to the pattern. In this work, around 30 points of the observed pattern were used to describe the background as a linear interpolation. The heights of these points were refined to obtain a better result in the background description.

The fluorite-type crystalline structure of CeO_2 and the atomic positions of Ce and O atoms at the base vectors were used as input in the Fullprof software. The number of cycles used in the refinement of each case was 30. Firstly, the diffractogram of a quartz standard sample provided by CNANO was refined in order to obtain the equipment resolution file, which is necessary to determine the crystallite size and strain of the nanoparticles analysed. Then, the diffractograms of the CeO_2 nanoparticles were refined. All refinements were performed using the following constrains:

- The V and W parameters of the reflection profile function were determined by refining the quartz standard sample and fixed to 0 for the analysis of the XRD patterns of the nanoparticles.

- The isotropic temperature parameter (B-factor) value of each atomic specie was fixed to the value obtained in the crystallographic information file (CIF) of CeO_2 [100].

- The overall B-factor was allowed to have only positive values.

- The O occupancy number value was allowed to vary between the values that correspond to the completely oxidized cerium oxide (CeO_2) and the completely reduced cerium oxide (Ce_2O_3).

- The Ce occupancy number value was fixed to the value that correspond to the completely oxidized cerium oxide (CeO_2)

- The correction for the 0 value in the 2θ scale was determined by refining the CeO_2 standard sample and then fixed to this value for all the CeO_2 nanoparticles.

- The transparency instrumental parameter was allowed to have only positive values.

Together with the χ^2 index, two other indexes were used to indicate the fit quality: the weighted profile factor (R_{wp}) and the expected weighted profile factor (R_{exp}). These indexes are described as follow:

$$R_{wp} = \left(\frac{\chi^2}{\sum_{i=1}^{Npoints} w_i I_i^{exp^2}} \right)^{\frac{1}{2}} \times 100 \tag{4.5}$$

$$R_{exp} = \left(\frac{Npoints - p}{\sum_{i=1}^{Npoints} w_i I_i^{exp^2}} \right)^{\frac{1}{2}} \times 100 \tag{4.6}$$

where p is the number of refined parameters and, therefore, $(Npoints - p)$ is the number of degrees of freedom. At the end of the refinement, the R_{wp} index cannot vary, because the χ^2 index has already reached the minimum value. Moreover, the closer the R_{wp}/R_{exp} ratio to 1 the better the fit quality.

4.2.3 X-ray Absorption Spectroscopy (XAS) Analysis

In order to determine the oxidation state and to probe the local atomic order of the CeO_2 nanoparticles, the XANES and EXAFS regions of the XAS spectra were analysed using the IFEFFIT package [101]. The spectra were initially analysed in accordance to the standard procedure of data reduction [79]. After this, the XANES and EXAFS spectra were analyzed as described in the next sections.

4.2.3.1 Analysis of the XANES Region

Aiming to determine the Ce(III) fraction (Ξ^{XANES}) value in each sample, the method proposed by Takahashi *et al.* [102] was used. This method consists on adjusting the XANES region of the absorption spectra by using one arctangent and three Lorentzian functions. The energy range used in the fitting procedure includes the single (double) contribution characteristic of the Ce(III) (Ce(IV)) compounds. The two Lorentzian functions correspond to the $2p_{3/2} \rightarrow (4f\xi)5d$ (around 5730 eV) and $2p_{3/2} \rightarrow (4f^0)5d$ (around 5738 eV) electronic transitions and are associated with the Ce(IV) component, while the other Lorentzian function corresponds to the $2p_{3/2} \rightarrow (4f^1)5d$ electronic transition (around 5726 eV) and can be associated with the Ce(III) component. The symbol ξ denotes that an electron at the 2p orbital of O was transferred to the 4f orbital of Ce. The arctangent functions are associated with the electronic transitions from the $2p_{3/2}$ electronic level to the continuum. The parameters of the arctangent and Lorentzian functions (energy position and width) were determined by fitting the XANES region of the Ce(IV) and Ce(III) standards. In the fitting of the XANES spectra of the other CeO_2 nanoparticles the only parameter variable was the height of each arctangent and Lorentzian function. The energy

position and width are constrained to the values determined by fitting the XANES region of the Ce(IV) and Ce(III) standard spectra. At the end, the fitting was refined allowing the width and energy positions variation of the Lorentzian functions by 0.5 eV around their previous fixed positions. The Ξ^{XANES} value in each case is determined by equation 4.7.

$$\Xi^{XANES} = \frac{A_1}{A_1 + A_2 + A_3} \tag{4.7}$$

where A_1 is the area under the Lorentzian function associated to the Ce(III) component and A_2 and A_3 are the areas under each Lorentzian function associated to the Ce(IV) component. Figure 4.2.2 presents an example of the XANES measurement at the Ce L_{III} edge of the sample 7 adjusted using this method.

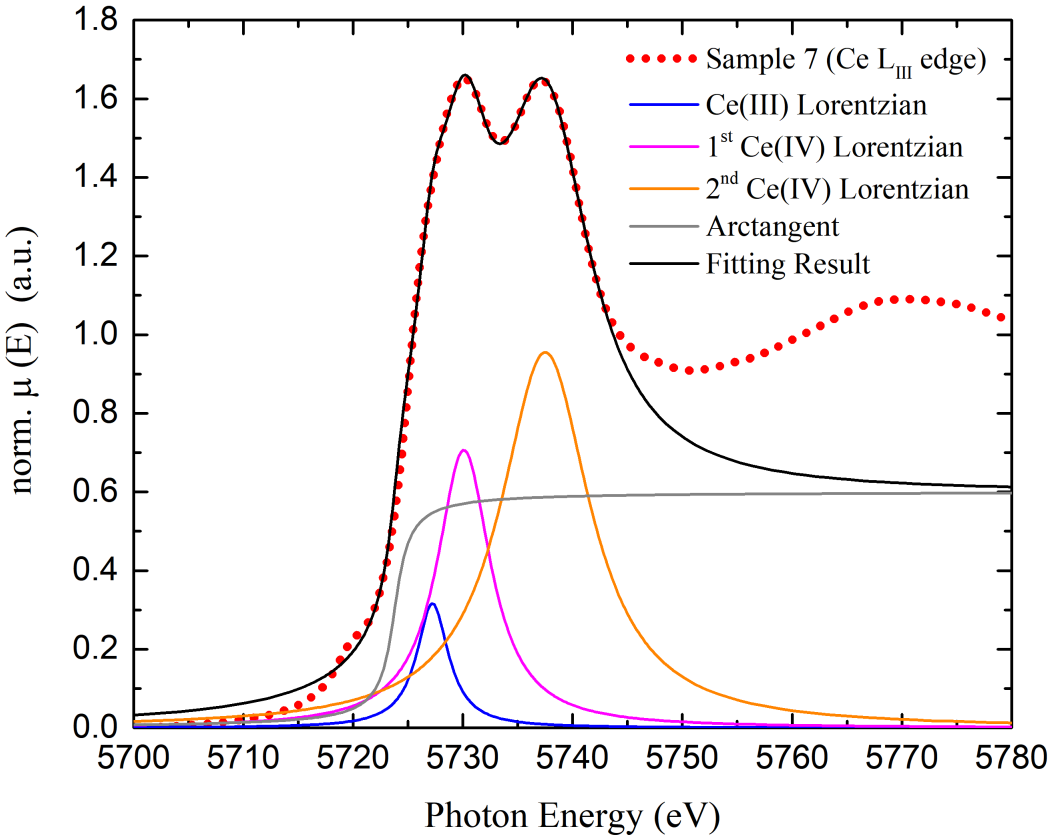

Figure 4.2.2 – XANES measurement at the Ce L_{III} edge of the sample 7 (red points) and the fitting performed using arctangent and Lorentzian functions (solid lines) that correspond to the Ce(III) and Ce(IV) components.

4.2.3.2 Analysis of the EXAFS Region

In order to analyse the EXAFS region, it is important to perform a correction due to the multielectron photoexcitations (MPE) effect before extracting the EXAFS oscillations

from the absorption spectra. The MPE effect [103] in Ce atoms corresponds to the generation of an atomic signal in the absorption spectrum, at around 5850 eV, together with the structural signal, due to coexcitations of valence and subvalence electrons of the atoms. For the Ce atom, this atomic signal is strong and should be removed. Aiming to perform this correction, two components of the MPE signal were considered. The first one corresponds to the Ce(III), represented by a Lorentzian function, and the other component corresponds to the Ce(IV), represented by a sum of two Lorentzian functions. A linear combination was used to determine the MPE signal that should be removed from the absorption spectrum, where the weight of each component corresponds to the Ce(III) and Ce(IV) fractions present on the sample, obtained by the analysis of the XANES region. Then, this signal was removed from the normalized absorption spectrum. This procedure was performed for all the EXAFS spectra of the CeO_2 nanoparticles. Figure 4.2.3 presents a comparison between the absorption spectrum of the CeO_2 standard sample before and after removal of the MPE contribution.

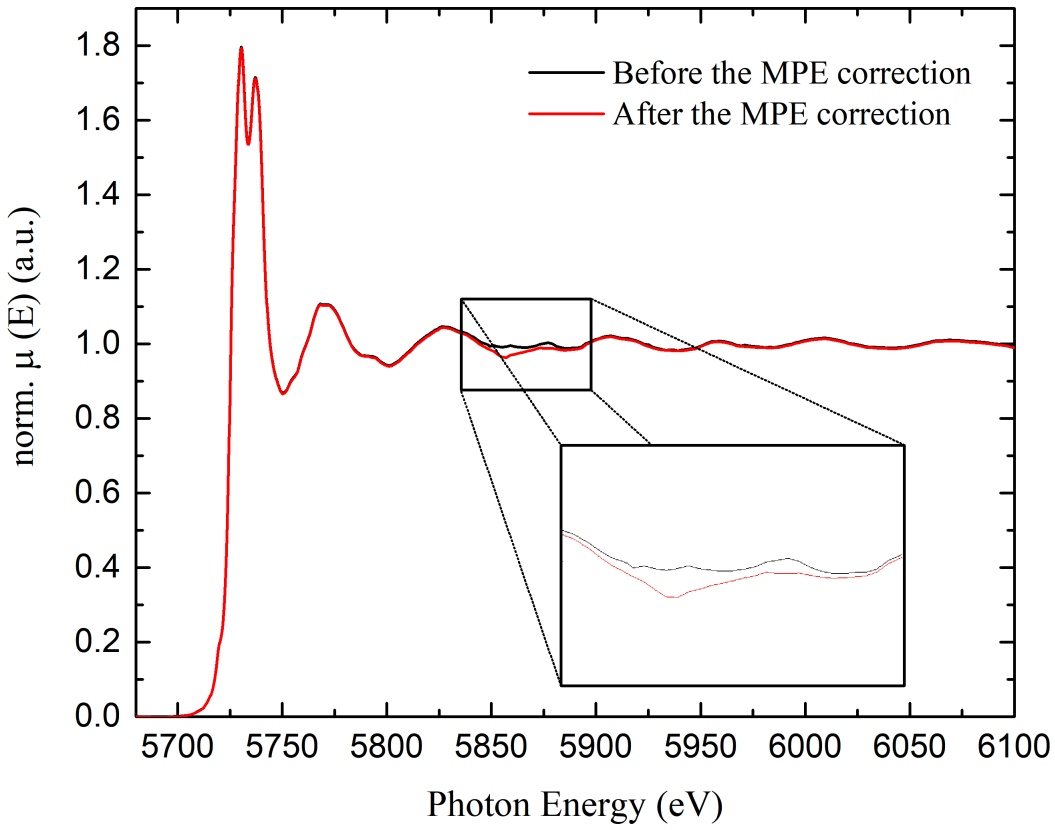

Figure 4.2.3 – Normalized EXAFS spectrum of the CeO_2 standard sample before and after removal of the MPE contribution. The difference between the spectra before and after the MPE correction is shown in the inset.

After performing the MPE correction, the EXAFS oscillations $\chi(k)$ were extracted from the normalized absorption spectra and k^2 weighted. The Fourier Transform (FT) of the $k^2\chi(k)$ oscillations was performed using a Kaiser-Bessel window [79] with a k-range of

5.5 $Å^{-1}$. This window selects the EXAFS region in the oscillations present in the absorption spectrum. The phase-shift and the scattering amplitude were calculated considering a CeO_2 cluster with 10 Å radius and the fluorite-type crystalline structure using the FEFF8 code [104]. The fitting of the FT of the EXAFS oscillations was performed only for the coordination shell of the Ce atom for all the CeO_2 nanoparticles. The parameter that corresponds to the correction for relaxation effects in the absorbing atom (S_0^2) was first determined by fitting the FT of the EXAFS oscillations of the CeO_2 standard sample. The S_0^2 value found was (0.69 ± 0.02). In order to adjust the FT of the EXAFS oscillations of all the synthesized CeO_2 nanoparticles, a Ce-H scattering path was considered. The phase-shifts and the scattering amplitudes of this path were calculated considering a CeH_2 cluster with 3.695 Å of lattice parameter using the FEFF8 code [104]. The FT of the EXAFS oscillations of all the CeO_2 nanoparticles were adjusted with the S_0^2 parameter constrained to the value determined by fitting the FT of the EXAFS oscillations of the standard sample. The coordination number of the Ce-O scattering path ($N_{\text{Ce-O}}$) was initially determined by the Ξ^{XANES} value of each case. At the end of the fitting, the $N_{\text{Ce-O}}$ values were allowed to vary. Moreover, by performing the fitting, it was found more than one value for the Debye-Waller factor of the Ce-H scattering ($\sigma^2_{\text{Ce-H}}$) that successfully adjusted the FT of the EXAFS oscillations of the synthesized nanoparticles. Therefore, the $\sigma^2_{\text{Ce-H}}$ parameter was constrained to be the same for all the CeO_2 nanoparticles.

4.2.4 X-ray Photoelectron Spectroscopy (XPS) Analysis

In order to determine the oxidation state of Ce in different depths, the Ce 3d and Ce 4d XPS spectra were analysed. The probed depth can be estimated by the inelastic mean free path of the photoelectrons coming from the Ce 3d and Ce 4d electronic levels. The TPP-2M equation gives λ_{IMFP} = 8 Å (Ce 3d) and λ_{IMFP} = 18 Å (Ce 4d). The analysis of the Ce 3d XPS region is challenging because of the complexity due to strongly mixed 4f final states, rearrangement of the electronic levels following the creation of a core hole and changes in the hybridization during oxidation processes [105]. This analysis was performed using the method described by Schierbaum *et al.* [106], and following the Burroughs's notation [107]. This method consists of adjusting the Ce 3d region with 10 distinct components, where each component is described as a symmetric Gaussian-Lorentzian sum function. 4 components correspond to the Ce(III) oxidation state (u_0, v_0, u', v') and the other 6 components correspond to the Ce(IV) oxidation state (u, v, u", v", u"', v"'). The Ce(III) components correspond to a pair of $3d_{3/2}$ and $3d_{5/2}$ doublets, therefore the intensity ratio Ce $3d_{5/2}$/Ce $3d_{3/2}$ was set to 1.5.

The Ce 3d and Ce 4d XPS spectra were adjusted with the XPSPeak 4.1 software. A Shirley-type background [108] was used. The percentage of the Gaussian and Lorentzian functions used to describe the components in the Ce 3d region was determined by fitting the component present at the energy position around 916.7 eV (labelled as u"') of the

standard sample. After that, the energy position values of the Ce 3d components reported by Schierbaum *et al.* [106] was used as input to adjust the XPS spectrum of the standard sample. For the Ce 3d XPS spectrum measured before the thermal treatment, the FWHM values were initially allowed to vary maintaining the same decreasing order as the FWHM values reported by Schierbaum *et al.* [106]. Since the fitting quality was not satisfactory, the energy position was allowed to vary 0.8 eV around the previous values, without allowing to invert the components position. For the Ce 3d XPS spectrum measured after the thermal treatment, it was not possible to maintain the same FWHM values as the values obtained in the fitting procedure of the samples before thermal treatment. Then, the energy position values were allowed to vary by a maximum of 0.3 eV from the values reported in the literature and the FWHM values were allowed to vary freely aiming to obtain a better adjust to the XPS spectrum. The Ce(III) fraction (Ξ^{XPS}) present in each sample can be calculated from the Ce 3d XPS spectra by the ratio of the sum of the intensity of the Ce(III) components to the sum of the intensities of all the components, following equation 4.8.

$$\Xi^{XPS}\ \text{Ce 3d} = \frac{U_0 + U' + V_0 + V'}{U_0 + U + U' + U'' + U''' + V_0 + V + V' + V'' + V'''} \tag{4.8}$$

where the upper case letters correspond to the intensities of the components.

The Ξ^{XPS} value present in each sample was calculated from the Ce 4d XPS spectra using the method described by Zhang *et al.* [109]. This method uses the fact that the two components at higher binding energies (around 123 eV and 126 eV) of the Ce 4d region can be assigned to the spin-orbit doublets associated with the Ce(IV) oxidation state. The fraction of the Ce(III) component is proportional to the ratio of the sum of the intensity of these two components associated with Ce(IV) ($I_{\text{Ce(IV)}}$) to the intensity of the full Ce 4d region (I_{Ce4d}), following equation 4.9.

$$\Xi^{XPS}\ \text{Ce 4d} = 1 - \left(\frac{I_{\text{Ce(IV)}}}{I_{\text{Ce4d}}} \times 3.78\right) \tag{4.9}$$

The $I_{\text{Ce(IV)}}$ and I_{Ce4d} values were calculated by integrating the Ce 4d region in the energy range from 119.6 eV to 130 eV and from 102 eV to 130 eV, respectively, after background removal. Then, the Ξ^{XPS} value was obtained from equation 4.9.

4.3 Theoretical Procedure

4.3.1 Density Functional Theory (DFT) Calculation

Aiming to obtain the electronic density of states (DOS) and the electronic band structure of the bulk and surface region of the CeO_{2-x}, DFT calculations were performed using the Quantum-ESPRESSO 5.4.0 package [110], which uses a plane-wave basis set to describe the behaviour of the valence electrons. In this work, an ultrasoft pseudopotential was employed using the projector-augmented wave (PAW) method [111] to describe the effect of the core electrons on the valence electrons of Ce and O atoms. For the exchange-correlation functional, the local density approximation (LDA) was used. The Gaussian smearing was used to describe the electronic occupations. In order to determine the values for the parameters corresponding to the plane waves kinetic energy cut-off, charge density kinetic energy cut-off, k-points grid size and the width of the Gaussian smearing, self consistent calculations varying these parameters were performed. It is important to obtain convergence values for these parameters to ensure the convergence of the next step calculations. The primitive unit cell of CeO_2, shown in Figure 4.3.1, was used to perform these calculations.

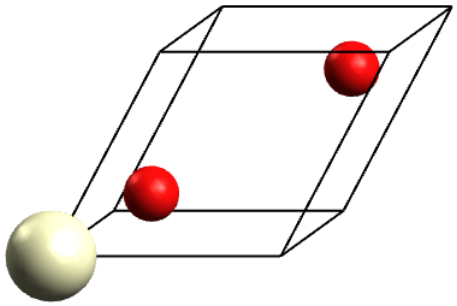

Figure 4.3.1 – Primitive unit cell of CeO_2 used to perform the self consistent calculations in order to determine the values of some parameter and ensure the convergence of the following calculations. The red and white spheres correspond to O and Ce atoms, respectively. The black solid line delimits the unit cell volume.

Figure 4.3.2(a) presents the total energy obtained by the self consistent calculations as a function of the plane waves kinetic energy cut-off. This parameter determines the amount of plane waves used to perform the calculations. The higher amount of plane waves implies in a more accurate results but also more time spent. However, there is an amount of planes waves where the total energy of the system becomes stable and can describe the system satisfactorily. In Figure 4.3.2(a) the stable region can be reached for 42 Ry. Therefore, the value of 46 Ry was chosen for the plane waves kinetic energy cut-off because the difference between the total energy becomes lower than 2×10^{-3} Ry when changing 4 Ry in the plane wave kinetic energy.

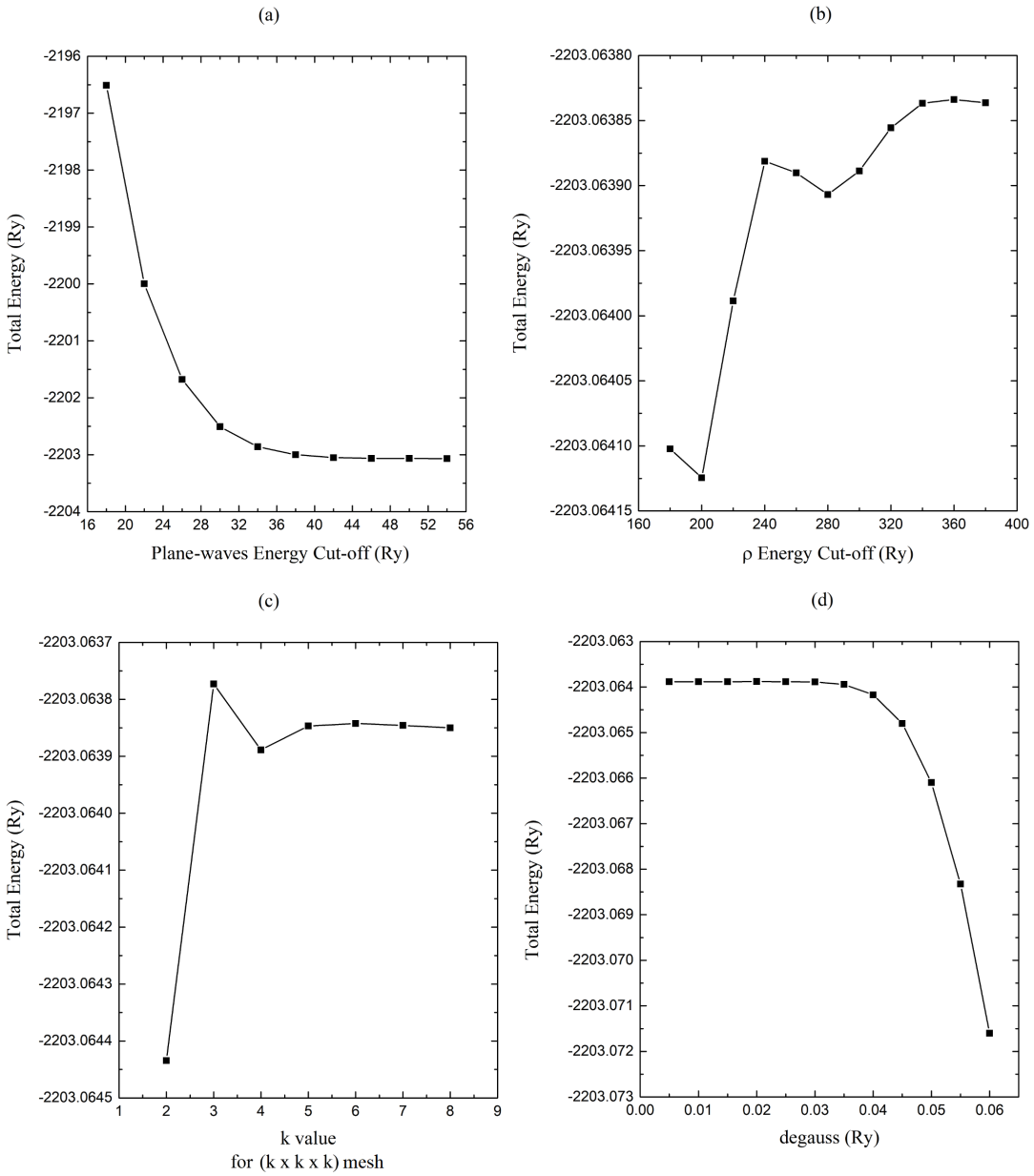

Figure 4.3.2 – Total energy obtained by the self consistent calculations as a function of the (a) plane waves kinetic energy cut-off, (b) charge density (ρ) kinetic energy cut-off, (c) k-points grid size and (d) *degauss* parameter value.

Figure 4.3.2(b) presents the total energy obtained by the self consistent calculations as a function of the charge density (ρ) kinetic energy cut-off. In the same way as the plane waves kinetic energy cut-off, the higher this parameter, the more accurate the results becomes and more time is spent to be finished. However, this parameter presents a stable region for the total energy too. This region can be observed in Figure 4.3.2(b) at the value of 240 Ry, where the difference between the total energy becomes lower than 10^{-5} Ry when changing 20 Ry. Therefore, the value of 240 Ry was chosen for the charge density (ρ) kinetic energy cut-off.

The total energy obtained by the self consistent calculations as a function of the k-

points grid size is presented in Figure 4.3.2(c). This parameter determines how accurate the Brillouin zone is described in the reciprocal space. In the same way as the two cases described above, this parameter presents a stable region. It is possible to observe a stable region for a value around $k = 4$, where the difference between the total energy becomes lower than 10^{-4} Ry when the k value is changed by 1. Therefore, the value $k = 4$ was chosen to form a 4×4×4 k-point grid.

Figure 4.3.2(d) presents the total energy obtained by the self consistent calculations as a function of the width of the Gaussian smearing (*degauss* parameter). The lower the value of this parameter the more accurate the electronic occupations can be described. It is possible to observe that this parameter becomes stable for a value around 0.03 Ry. However, aiming to obtain a more detailed description of the electronic density of states, the value of 0.005 Ry was chosen for this parameter.

The DFT calculations fail to fully describe the electronic behaviour of CeO_2 because the Ce 4f orbital presents localized electrons. In order to obtain a correct description of this system, the DFT+U calculations were performed, using the simplest form of this correction presented in the last chapter. In the literature, it is possible to find many articles using different values of the U_{eff} parameter depending on the mail goal of the calculation [112–115]. In this work, the value for the U_{eff} parameter was determined by using the linear response method proposed by Cococcioni and Gironcoli [116]. This method determines the value for the U_{eff} parameter by

$$U_{eff} = \chi_0^{-1} - \chi^{-1} \tag{4.10}$$

where $\chi = \frac{\partial n_I}{\partial \alpha_I}$ and $\chi_0 = \left(\frac{\partial n_I}{\partial \alpha_I}\right)_0$ are the responses allowing (SCF response) and not allowing (bare response) localized perturbation to be optimally screened, respectively. The n_I is the occupation number on the site I. The α_I is a perturbation in the potential on each nonequivalent "Hubbard" site I. In order to determine the value for the U_{eff} parameter using this method, the conventional unit cell of CeO_2, presented in Figure 4.3.1, was used. Firstly, a self consistent (SCF) calculation with the non-perturbed potential ($\alpha = 0$) was performed and the charge density was stored. Then, new SCF calculations were performed starting from the charge density stored for $\alpha = 0$ and small perturbations were added in the potential. For these new calculations, the occupations for all sites in the first and last SCF interactions are recorded. The localized perturbation non-optimally screened (bare response) was considered as the first SCF interaction and the localized perturbation optimally screened (SCF response) was considered as the last SCF interaction. After that, these sets of occupation values were plotted as a function of the potential perturbation (α). Figure 4.3.3 presents this plot. A linear fitting was performed for each set of occupation values. The slope of the straight line fitted is equal to the χ_0 for the bare response set and χ for the SCF response set. So, it was possible to use the equation 4.10 to obtain the value

of the U_{eff} parameter as $U_{eff} = 5.5$ eV. This U_{eff} parameter value was used to perform the relaxation procedure and the DOS calculations for CeO_{2-x} bulk and surface. For the relaxation procedure, the convergence threshold on the total energy and convergence threshold on forces for ionic minimization were chosen as 10^{-4} and 10^{-3} Ry, respectively. The convergence threshold for selfconsistency was chosen as 10^{-5} Ry for all calculations.

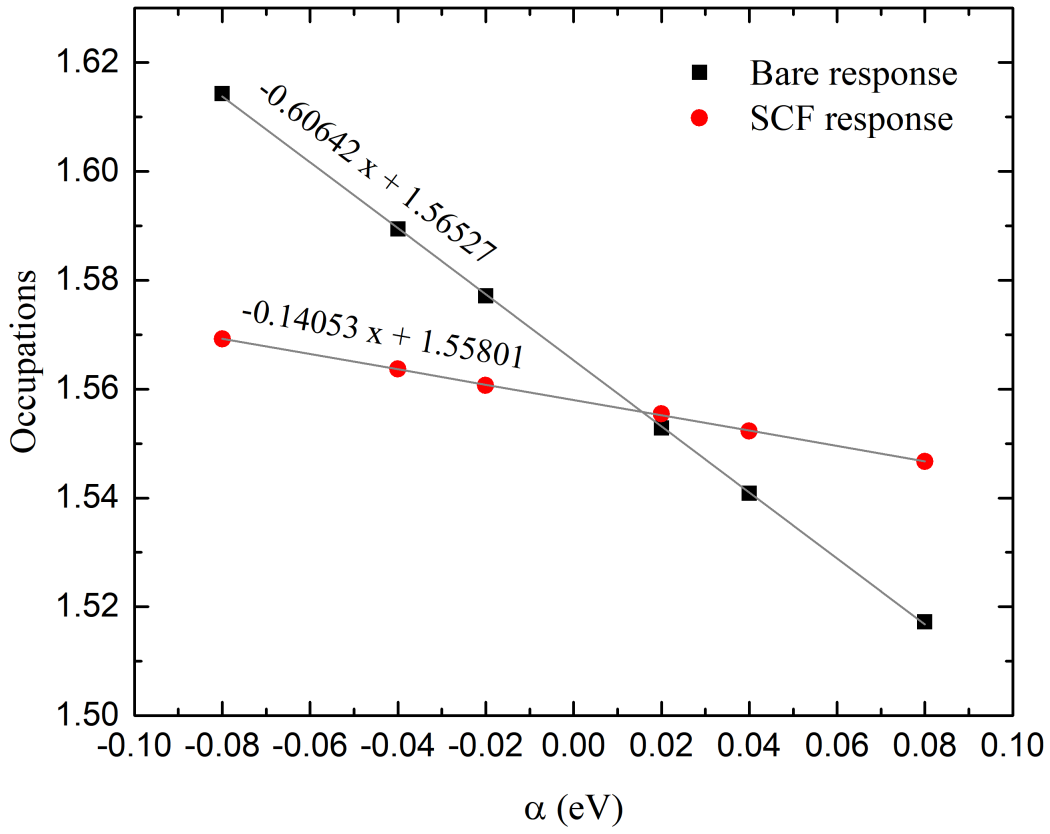

Figure 4.3.3 – Occupation number as a function of the perturbation in the potential (α) for the bare response and the SCF response. The grey straight lines correspond to the linear fitting performed for each set of occupation values. The equation of each straight line is shown too.

The bulk calculations were performed using 48 atoms (16 Ce atoms and 32 O atoms) in the fluorite-type crystalline structure of CeO_2 (Figure 4.3.4). For the surface calculations, 9 layers oriented in the (111) direction of the CeO_2 cluster was used because this orientation corresponds to the most stable case [117–119]. Figure 4.3.5 presents the slab used in the calculation. A vacuum layer of around 15 Å was set between the slabs to minimize their interaction. The three bottom layers were not allowed to vary the parameter in the relaxation procedure, while the other six layers were allowed to vary in this procedure. Both bulk and surface calculations were performed for 0, 1 and 2 O vacancies in order to investigate the electronic behaviour of the system by varying its oxidation state. It corresponds to 0 %, 12.5 %, and 25 % of O vacancy in the bulk calculations.

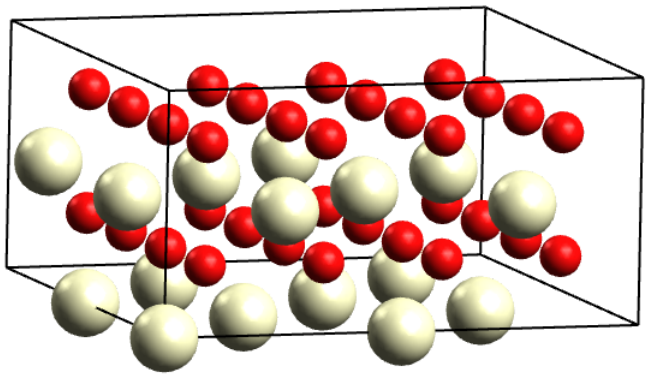

Figure 4.3.4 – The CeO_2 structure proposed with 48 atoms. The red and white spheres correspond to O and Ce atoms, respectively. The black solid line delimits the unit cell volume.

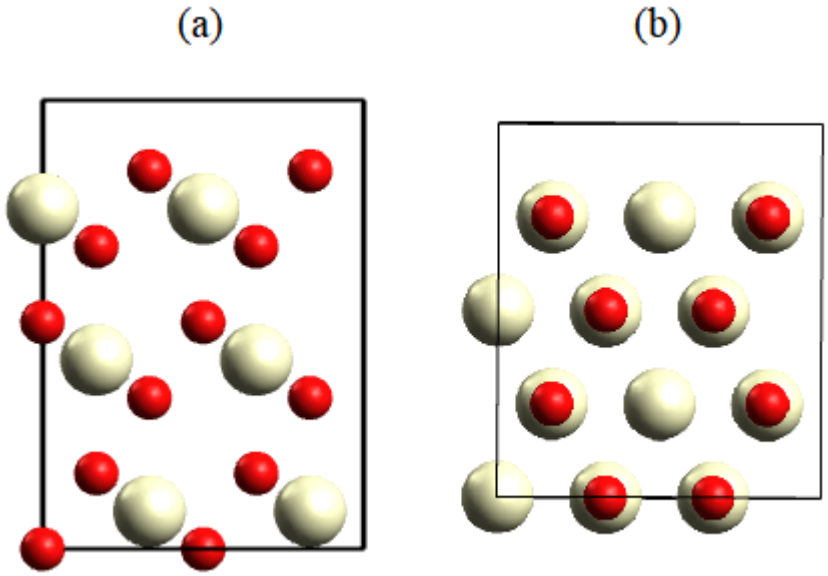

Figure 4.3.5 – The $CeO_2(111)$ slab used in the calculation shown in (a) side view and (b) top view. The red and white spheres correspond to O and Ce atoms, respectively. The black solid line delimits the unit cell volume.

5 Elucidation of the Bulk and Surface Properties of CeO_2 Photocatalysts to Improve the H_2 Evolution Photocatalytic Activity

This chapter is dedicated to present the results obtained, data analysis and theoretical calculations described in the last chapter. These results will be discussed in order to determine the properties of the CeO_2 photocatalysts that are important to improve the H_2 evolution photocatalytic activity.

5.1 H_2 Evolution Photocatalytic Activity Results

Figure 5.1.1 presents the H_2 yield as a function of the photocatalytic reaction time obtained from the H_2 evolution photocatalytic activity measurements. It was observed that the H_2 yield measurement occurred after 15 to 30 minutes typically. It occurs because it is well known that at the beginning of the reaction the H_2 production is not linear. The results show that the H_2 yield values have a different time dependence between the cerium oxide nanoparticles. Moreover, almost all the synthesized cerium oxide nanoparticles present significant improvement on the photocatalytic activity in comparison to the commercial standard sample. In order to obtain the H_2 evolution photocatalytic activity for each sample, a straight line was adjusted for each set of points presented in Figure 5.1.1. The slope of these straight lines gives the H_2 evolution photocatalytic activity. The uncertainty for the H_2 evolution photocatalytic activity values was obtained from the fitting result.

Table 5.1 presents the results for the H_2 evolution photocatalytic activity obtained from the data shown in Figure 5.1.1. It is possible to observe that only the sample 8 presents an activity lower than the standard sample. All the other synthesized nanoparticles present an activity higher than the standard sample. Moreover, the sample 7 presents the highest H_2 evolution photocatalytic activity value, about ten times higher than the standard sample. Table 5.2 presents typical results for the H_2 evolution photocatalytic activity that can be found in the literature for different photocatalysts. The co-catalyst, reducing agent, power and minimum wavelength (λ) of the light source used are presented as well. By comparing these typical results with the highest result of H_2 evolution photocatalytic activity obtained in the present work (Sample 7), it is possible to observe that the result obtained is better than almost all the photocatalysts without co-catalyst or reducing agent. Note that in this work the light source power used is lower than the light source power used in the literature. Moreover, the photocatalytic activity obtained for

Sample 7 is comparable with the highest photocatalytic activity for the CeO_2 presented in Table 5.2, which utilize a co-catalyst of Cs and $(NH_4)_2CO_3$ as reducing agent. The highest photocatalytic activity presented in Table 5.2 corresponds to a TiO_2 photocalyst utilizing Pt as co-catalyst and Na_2CO_3 as reducing agent. However, since the H_2 evolution photocatalytic activity does not present a linear dependence with the light source power, it is not possible to know if the Sample 7 is better or worse than that photocatalyst. On the other hand, it is possible to conclude that the Sample 7 is a great option to be utilized together with an optimized co-catalyst and an optimized reducing agent in order to improve H_2 evolution photocatalytic activity even more.

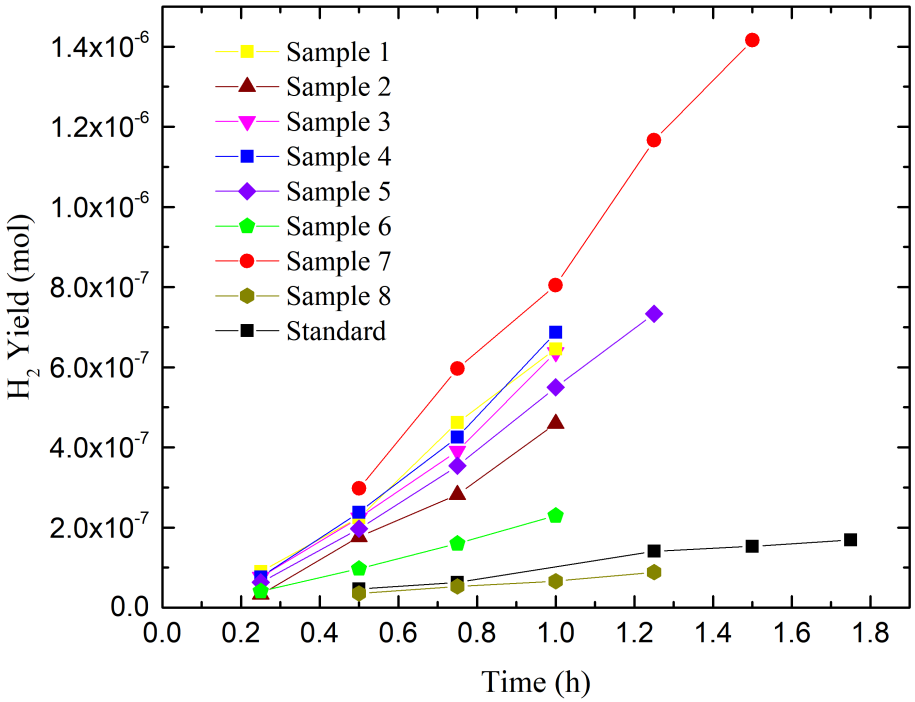

Figure 5.1.1 – H_2 yield as a function of the photocatalytic reaction time obtained from the photocatalytic H_2 evolution photocatalytic activity measurements for the cerium oxide nanoparticles.

Furthermore, it is important to notice in Table 5.1 that it is not possible to observe a direct relation between the surface area of the cerium oxide nanoparticles and the H_2 evolution photocatalytic activity values. It means, there are other parameters relevant to the photocatalytic activity, results that are dependent on the nanoparticles synthesized. Since it is well known that a high surface area presents an elevated number of catalytic active sites, it improves the photocatalytic activity. Then, the H_2 evolution photocatalytic activity values were normalized by the corresponding surface area of the cerium oxide nanoparticles in order to facilitate the comparison between the nanoparticles photocatalytic activity and other parameters that influence on the photocatalytic activity results. An important parameter is the band gap energies of the cerium oxide nanoparticles. The band gap energies are very important for the photocatalytic activity since it influences

Table 5.1 – Surface area, H_2 evolution photocatalytic activity and H_2 evolution photocatalytic activity normalized by the surface area for the cerium oxide nanoparticles. The uncertainty associated to the surface area values is around 5 m^2/g.

Sample	Surface Area $\left(\frac{m^2}{g}\right)$	H_2 Evolution $\left(\times 10^{-6}\ \frac{mol}{h\ g}\right)$	H_2 Evolution / Surface Area $\left(\times 10^{-7}\ \frac{mol}{m^2\ h}\right)$
1	138	76 ± 5	5.5 ± 0.4
2	130	55 ± 4	4.2 ± 0.4
3	104	74 ± 6	7.1 ± 0.7
4	126	81 ± 6	6.4 ± 0.5
5	165	68 ± 3	4.1 ± 0.2
6	137	25 ± 1	1.8 ± 0.1
7	170	112 ± 5	6.6 ± 0.4
8	201	7 ± 1	0.35 ± 0.05
Standard	38	11 ± 1	2.9 ± 0.5

Table 5.2 – Comparison of the H_2 evolution photocatalytic activity obtained by using different photocatalysts in the literature and the better result obtained in the present work. The co-catalyst, reducing agent, power and minimum wavelength (λ) of the light source used are shown for each case.

Photocatalyst	Co-catalyst	Reducing Agent	Power of the light source (W)	λ (nm)	H_2 Evolution $\left(\times 10^{-6}\ \frac{mol}{h\ g}\right)$
TiO_2 (rutile) [68]	-	KNO_3	450	> 250	0.04
TiO_2 (anatase) [69]	Pt	-	400	> 200	3.33
TiO_2 (anatase) [69]	Pt	Na_2CO_3	400	> 200	1893.33
ZrO_2 [120]	-	-	400	> 200	72
ZrO_2 [120]	-	$(NH_4)_2CO_3$	400	> 200	142
CeO_2 [45]	-	-	400	> 200	12.50
CeO_2 [66]	-	-	450	> 200	7.08
CeO_2 [66]	Pt	-	450	> 200	7.67
CeO_2 [66]	Li	-	450	> 200	8.35
CeO_2 [66]	Cs	-	450	> 200	81.60
CeO_2 [66]	Cs	$(NH_4)_2CO_3$	450	> 200	166.42
CeO_2 (Sample 7)	-	Ethanol	225	> 200	112

on the absorption efficiency of the photons by the photocatalyst. The ultraviolet-visible (UV-Vis) spectroscopy technique was used to obtain these values for each sample.

5.2 Ultraviolet-visible (UV-Vis) Spectroscopy Results

Figure 5.2.1 presents the UV-Vis spectra of the cerium oxide nanoparticles. It is possible to observe that the absorption edge of the spectrum shifts horizontally depending on the case. This shift indicates a difference in the bang gap energies between the cerium oxide nanoparticles. Since the lower the wavelength (λ) of the incident radiation the higher the radiation energy, it is possible to observe that sample 7 presents the lowest band gap energy, because the absorption edge of this sample is positioned on the highest λ value. In the same way, it is possible to observe that the standard sample presents the highest band gap energy.

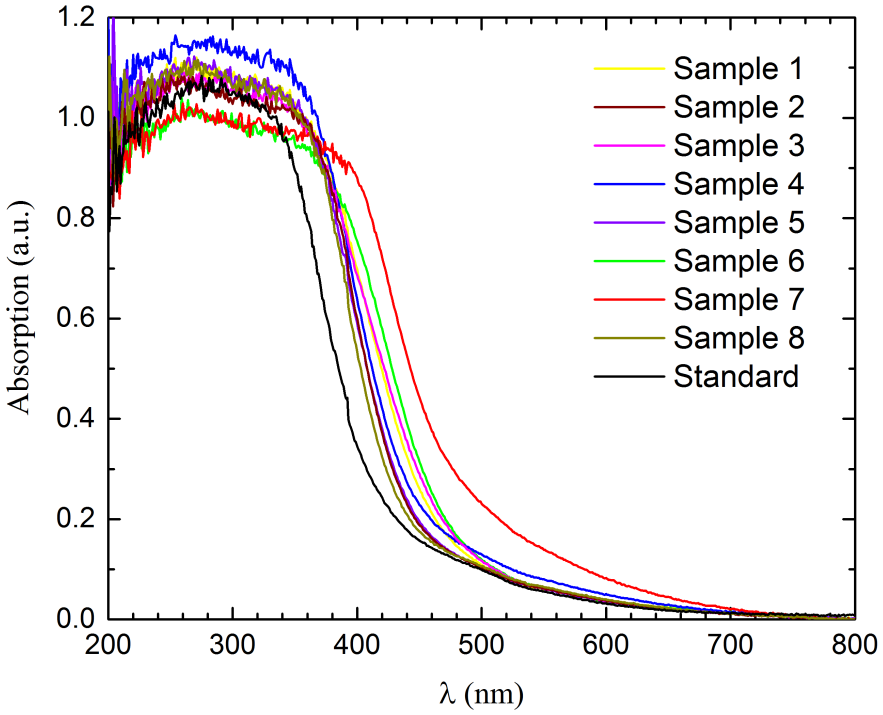

Figure 5.2.1 – UV-Vis spectra of the cerium oxide nanoparticles synthesized. The position on the wavelength axis at the absorption edge of the spectrum is not the same for all samples indicating that there is a difference in the bang gap energy value.

The direct (E_g^D) and indirect (E_g^I) band gap energies of the cerium oxide nanoparticles are shown in Table 5.3. It is possible to observe that the band gap energies vary among the cerium oxide nanoparticles. The lowest band gap energy obtained in this work is 2.73 eV for the sample 7. In the literature, the cerium oxide presents a typical direct band gap energy in the range (2.92 - 3.7) eV [63, 64]. It means the values found in this work are significantly lower than those found in the literature and it explains partially the good photocatalytic results obtained, since improving the photon absorption efficiency is very important in order to improve the H_2 evolution photocatalytic activity.

In order to observe the relation between the H_2 evolution photocatalytic activity and

Table 5.3 – Direct and indirect band gap energies for the cerium oxide nanoparticles obtained by the UV-Vis spectroscopy analysis.

Sample	E_g^D (eV)	E_g^I (eV)
1	2.88 ± 0.03	2.27 ± 0.03
2	2.97 ± 0.03	2.46 ± 0.03
3	2.88 ± 0.03	2.24 ± 0.03
4	2.96 ± 0.03	2.39 ± 0.03
5	3.0 ± 0.03	2.41 ± 0.03
6	2.79 ± 0.03	2.24 ± 0.03
7	2.73 ± 0.03	2.16 ± 0.03
8	3.0 ± 0.03	2.49 ± 0.03
Standard	3.16 ± 0.03	2.51 ± 0.03

the band gap energies for the cerium oxide nanoparticles analysed, the H_2 evolution photocatalytic activity normalized by the surface area was plotted as a function of the direct (E_g^D) and indirect (E_g^I) band gap energies of the cerium oxide nanoparticles, which is presented in Figure 5.2.2 and Figure 5.2.3, respectively. In these figures, the cerium oxide nanoparticles presenting mesopores and micropores on the surface (samples 6, 7 and 8) are identified as red circles. The black circles represent the cerium oxide nanoparticles with the presence of microporous and without the presence of mesopores at the surface. It is possible to observe that, in general, the expected behaviour that a lower band gap energy corresponds to a higher photocatalytic activity is presented. Moreover, the cerium oxide nanoparticles that do not present mesopores at the surface present an approximately linear behaviour between H_2 evolution photocatalytic activity normalized by the surface area and band gap energies. On the other hand, the cerium oxide nanoparticles that present mesopores at the surface present a different mathematical behaviour with an abrupt increase of the H_2 evolution photocatalytic activity normalized by the surface area with the decrease on the band gap energies. It is hard to state the mathematical relation in this case because there are only three points measured but the results may show an exponential dependence, for example. In the literature, a relation of the photocatalytic activity with the direct or indirect band gap energy for the photocatalyst it is not found. These results do not explain fully the photocatalytic results and the dependence of the band gap energies with the cerium oxide nanoparticles synthesized should be clarified. Aiming this, the Ce(III) fraction (Ξ) was investigated in the cerium oxide nanoparticles.

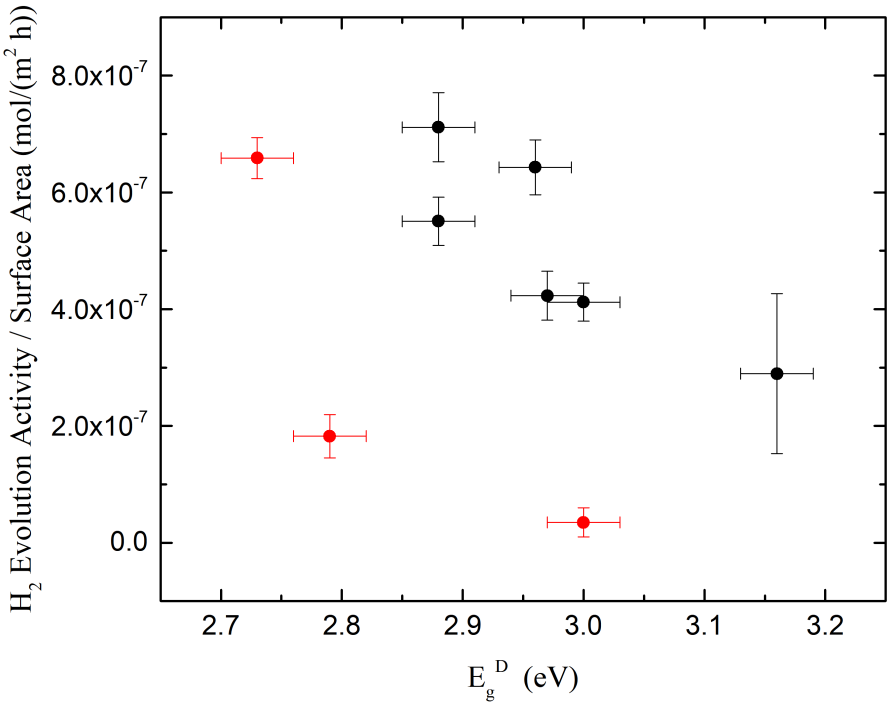

Figure 5.2.2 – The H_2 evolution photocatalytic activity normalized by the surface area as a function of the direct band gap energies. The red circles correspond to the cerium oxide nanoparticles that present mesopores at the surface.

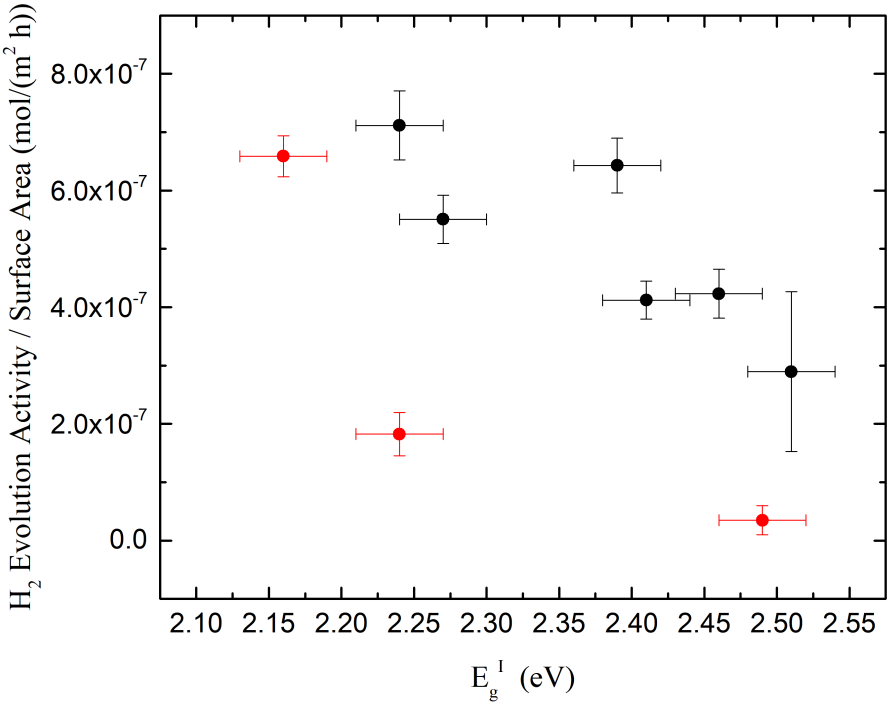

Figure 5.2.3 – The H_2 evolution photocatalytic activity normalized by the surface area as a function of the indirect band gap energies. The red circles correspond to the cerium oxide nanoparticles that present mesopores at the surface.

5.3 X-ray Diffraction (XRD) Results

The diffractograms of the cerium oxide nanoparticles obtained by the XRD measurements are presented in Figure 5.3.1. It is possible to observe that all the nanoparticles present the same crystalline structure, the cubic fluorite-type crystalline structure of CeO_2. Moreover, all the synthesized cerium oxide nanoparticles present broader Bragg reflections in comparison to the standard sample, indicating that the synthesized nanoparticles present a smaller crystallite size and/or more structural defects and strain than the standard sample. The crystal structure was refined for each sample to match the XRD patterns measured and the lattice parameter, crystallite size, strain and O occupancy were obtained for each case. The O occupancy allows one to calculate the Ξ^{XRD} value in the nanoparticles. This value can be compared with the Ξ^{XRD} value obtained from the lattice parameter using the Kim's equation [99]. This equation is used specifically for cerium oxide (CeO_{2-x}) samples and allows one to obtain the x value by

$$x = \frac{a(\text{Å}) - a_0(\text{Å})}{0.4612} \tag{5.1}$$

where a(Å) is the lattice parameter of the nanoparticles given in Å and a_0 is the lattice parameter of a reference sample that presents $x = 0$.

The XRD patterns and the fitting obtained by the Rietveld refinement for each case are presented in Figure 5.3.1. The χ^2, R_{wp}, R_{exp} and R_{wp}/R_{exp} ratio values obtained for the fitting were lower than or equal to 1.28, 13.8, 12.91 and 1.13, respectively, which demonstrates the good quality of the Rietveld refinement results. The crystallite mean diameter, strain and lattice parameter values obtained by the Rietveld refinement are presented in Table 5.4. The Ξ^{XRD} value evaluated by the Kim's equation is presented as well. It is possible to observe that the crystallite mean diameter of the standard sample is bigger than the other nanoparticles and the values for the synthesized nanoparticles are very similar. The comparison of these values with the particle mean diameter obtained by Transmission Electron Microscopy (TEM) measurements [22] (see table 4.1) allows to observe that the TEM results always present a particle mean diameter bigger than or equal to that obtained by the Rietveld refinement. The discrepancy between XRD and TEM results for the particle size is well known from the literature [121]. The wider the Bragg reflection the smaller and/or higher the defects concentration in the sample. As it is expected to have a high defect concentration in the cerium oxide nanoparticles synthesized it gives a widening of the Bragg reflections that is interpreted as a smaller size of the nanoparticles. In fact, the strain value of the standard sample is smaller than the nanoparticles synthesized which have similar values.

The O occupancy values presented are equal to the atom multiplicity in the unit cell divided by the number of possible symmetry operations of this unit cell. The O occupancy

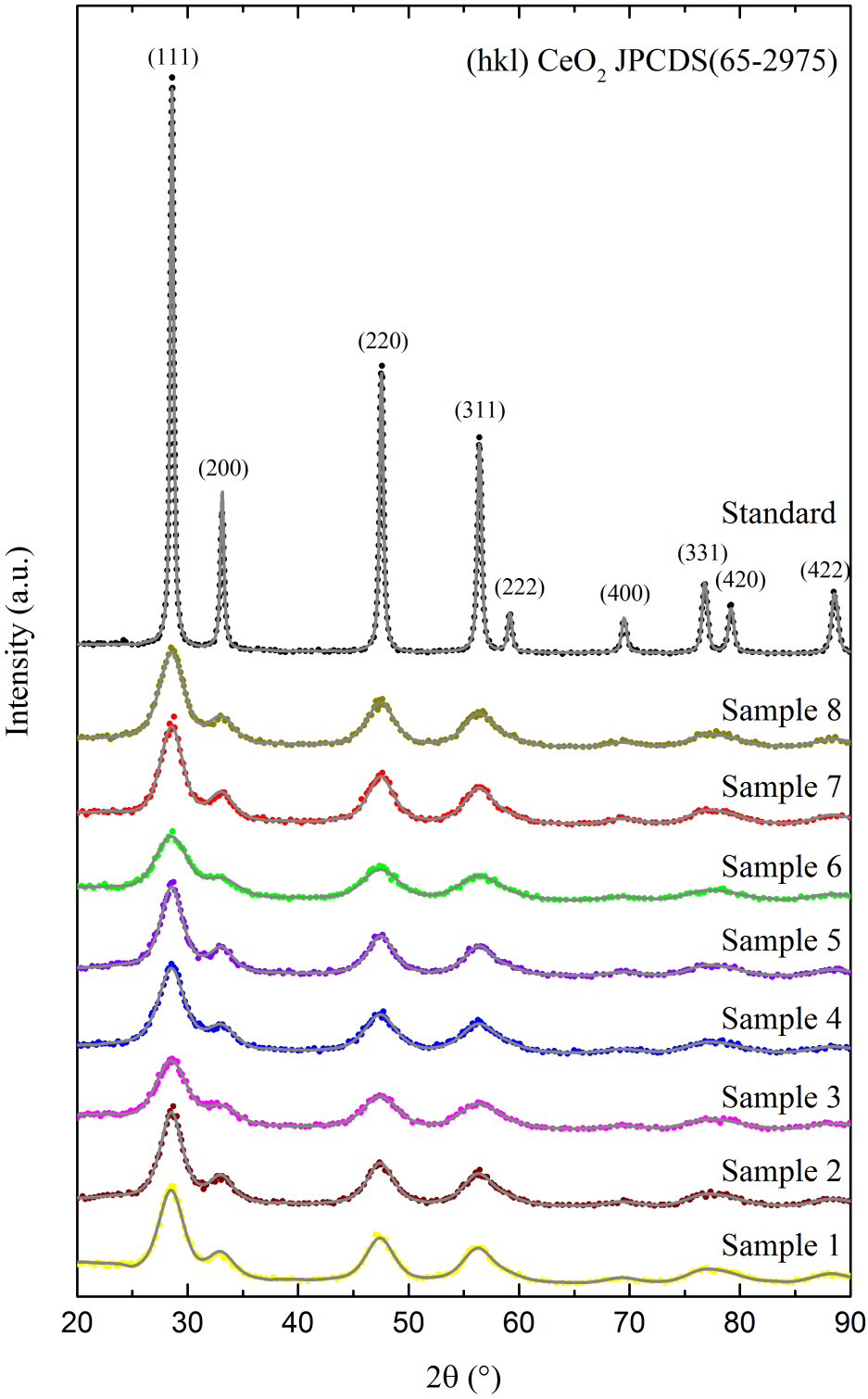

Figure 5.3.1 – Diffraction patterns of the cerium oxide nanoparticles and the result of Rietveld refinement. The points correspond to the experimental data. The gray solid line corresponds to the adjustment obtained by the Rietveld refinement.

values are the same for all the cerium oxide nanoparticles synthesized and the cerium oxide standard, equal to 0.04167 that corresponds to the value of the fully oxidized case

[100]. If these values were allowed to vary, the Rietveld refinement results do not change significantly. It indicates that the XRD patterns of all nanoparticles have no dependence with this parameter and all cerium oxide nanoparticles are almost fully oxidized. However, it is possible to observe that the lattice parameter value is different between the samples. Considering that the standard sample presents $\Xi^{XRD} = 0$ (fully oxidized), it was possible to obtain the Ξ^{XRD} value for the synthesized cerium oxide nanoparticles by using the Kim's equation [122]. It is possible to observe that the Ξ^{XRD} value obtained with this method is almost the same for all the cerium oxide nanoparticles. Therefore, it is possible to conclude that the cerium oxide nanoparticles present approximately the same oxidation state. However, the XRD measurements performed were sensitive to the bulk region of the sample which should have different results than those found at the surface region of the nanoparticles. In order to corroborate these results and to investigate the local atomic order of the cerium oxide nanoparticles, the samples were investigated by means of the X-ray Absorption Spectroscopy (XAS) technique.

Table 5.4 – Crystallite mean diameter (Size), strain and lattice parameter (a) values obtained by the Rietveld refinement. The Ξ^{XRD} value was evaluated by the Kim's equation. The uncertainty associated to the size and strain values are, respectively, 0.1 nm and 10^{-5} %.

Sample	Size (nm)	Strain (%)	a (Å)	Ξ^{XRD} value by Kim's equation
1	2.8	1.011×10^{-2}	5.4234	0.06
2	2.9	1.481×10^{-2}	5.4192	0.05
3	2.5	1.318×10^{-2}	5.4206	0.05
4	2.6	1.733×10^{-2}	5.4192	0.05
5	3.2	1.554×10^{-2}	5.4149	0.03
6	2.4	1.174×10^{-2}	5.4194	0.05
7	3.0	1.166×10^{-2}	5.4157	0.03
8	2.9	1.304×10^{-2}	5.4162	0.03
Standard	19.4	5.62×10^{-3}	5.4089	0.00

5.4 X-ray Absorption Spectroscopy (XAS) Results

5.4.1 XANES Analysis Results

Figure 5.4.1 presents the XANES region of the normalized XAS spectra of the cerium oxide nanoparticles measured at the Ce L_{III} edge and the respective fitting. The normalized XAS spectrum of the $CeOHCO_3$ compound, used as Ce(III) standard, is shown too. It is possible to observe the Ce(III) and Ce(IV) characteristic fingerprints present

in the XANES region of the standard compounds. The Ce(III) component has an important contribution at 5725.9 eV, while the Ce(IV) component shows a doublet in this region. Since the spectra of all the cerium oxide nanoparticles synthesized are very similar to the spectrum of the Ce(IV) standard sample and it does not present a significant Ce(III) component, it can be concluded that all the cerium oxide nanoparticles are almost fully oxidized and have approximately the same oxidation state than the Ce(IV) standard sample.

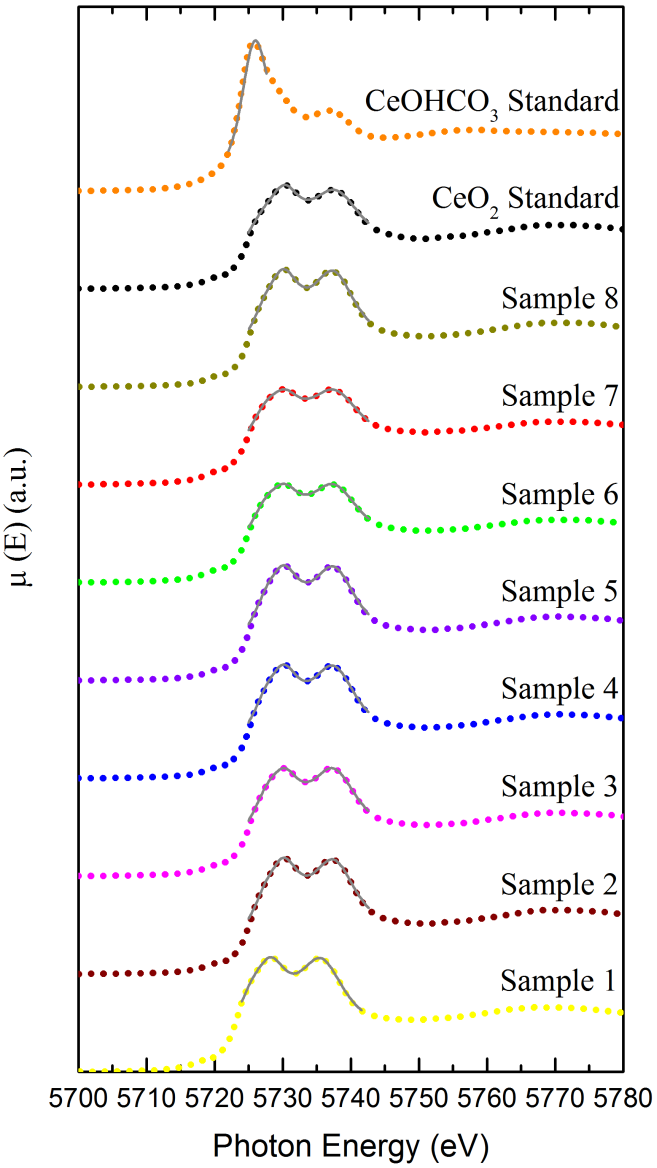

Figure 5.4.1 – XANES spectra measurements at the Ce L_{III} edge for the cerium oxide samples synthesized and for the standard samples. The points correspond to the experimental data. The gray solid line corresponds to the best fitting obtained.

The reduced χ^2 factor obtained in the fitting was always smaller than 7.8×10^{-5}, which shows the good quality of the fitting. The Ξ^{XANES} is presented in Table 5.5. The CeO_2

standard sample was used as the Ce(IV) standard and, therefore, it has $\Xi^{XANES} = 0$. Considering the uncertainty of the Ξ^{XANES} value, it is possible to observe that the synthesized nanoparticles of cerium oxide present approximately the same oxidation state, which is almost fully oxidized. This conclusion is in accordance with the result obtained from the XRD analysis.

Table 5.5 – Ξ^{XANES} values of the cerium oxide nanoparticles obtained by the fitting performed in the XANES region of the X-ray absorption spectra. The uncertainty associated to the Ξ^{XANES} values is around 0.05.

Sample	Ξ^{XANES}
1	0.09
2	0.05
3	0.09
4	0.06
5	0.06
6	0.11
7	0.12
8	0.06
Standard	0.00

An interesting relation involving the direct band gap energies can be observed in Figure 5.4.2. This figure presents the ratio between the area of the 1^{st} Ce(IV) Lorentzian function (A2) and the area under the 2^{nd} Ce(IV) Lorentzian function (A3) obtained from the XANES analysis as a function of the direct band gap energies of all the cerium oxide nanoparticles. It is possible to observe that a linear behaviour with great correlation is presented in Figure 5.4.2, as shown by the red line adjusted to the data. As previously presented, the 1^{st} Ce(IV) Lorentzian function corresponds to the $2p_{3/2} \rightarrow (4f\xi)5d$ transition, where the symbol ξ denotes that an electron in the 2p orbital of O was transferred to the 4f orbital of Ce, and the 2^{nd} Ce(IV) Lorentzian function corresponds to the $2p_{3/2} \rightarrow (4f^0)5d$ transition. The difference between these transitions is that the first one contains the Ce 4f orbital occupied with one electron while the second one presents the Ce 4f orbital unoccupied. It is possible to observe in Figure 5.4.2 that the higher the A2 area in relation to the A3 area, the higher the direct band gap energy for the cerium oxide nanoparticles. In other words, the bigger number of Ce atoms with the Ce 4f orbital occupied present in the sample, the higher the direct band gap energy of the sample. It means the tuning of the band gap energies in the CeO_2 nanoparticles is done by tuning the number of Ce atoms with the 4f orbital partially filled by electrons coming from the O 2p orbital. In the literature, it is not found a relation between the occupancy of such electronic orbital of a semiconductor material with the band gap energy of this semiconductor material. Therefore, this interesting link between a macroscopic property (band gap energy) and

a microscopic property (occupancy of such electronic orbital) possibly was first observed in this work, particularly for CeO_2 nanoparticles. The DFT results shown in Section 5.7 explain the change observed on the Ce 4f orbital occupancy.

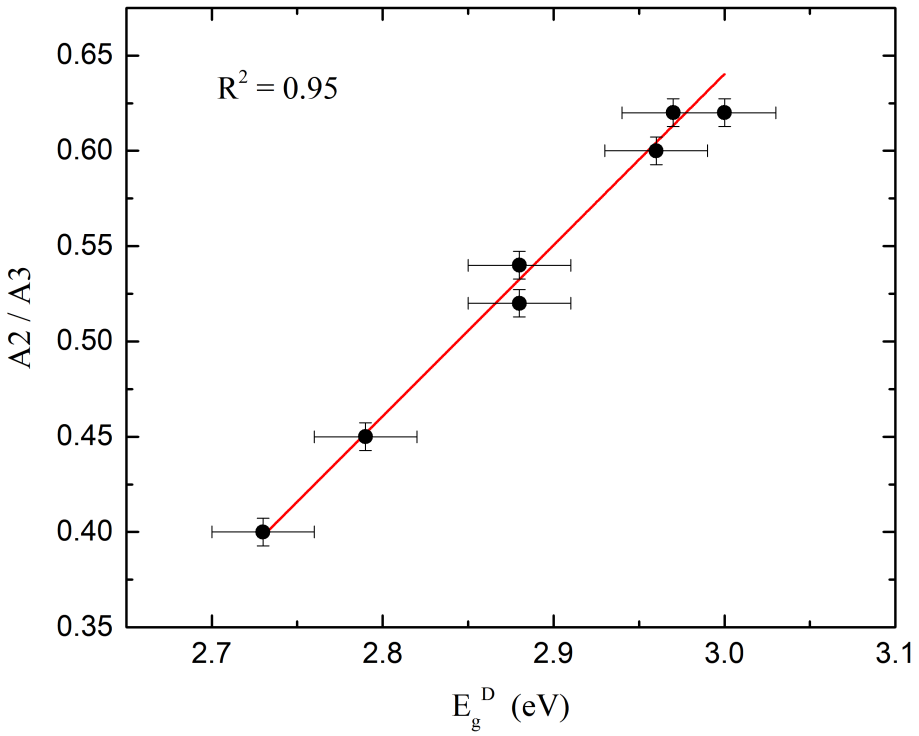

Figure 5.4.2 – Ratio of the area under the 1^{st} Ce(IV) Lorentzian function (A2) and the area under the 2^{nd} Ce(IV) Lorentzian function (A3) obtained from the XANES analysis as a function of the direct band gap energies of the cerium oxide nanoparticles. The red solid line corresponds to a linear fitting performed in order to show the great correlation presented by the data.

5.4.2 EXAFS Analysis Results

The Fourier Transform (FT) of the EXAFS oscillations $k^2\chi(k)$ of the X-ray absorption spectra and the fitting obtained are shown in Figure 5.4.3. The fitting was optimized using the k^2-weighted oscillations, and the fitting results were satisfactorily good for k- and k^3-weighted oscillations as well. The R factor obtained in the fitting was always lower than 0.001, which demonstrates the excellent quality of the fitting results. The FT clearly showed the Ce-O and Ce-Ce scattering paths for all the cases, where only the coordination shell, which corresponds to the Ce-O scattering path, was adjusted. All the cerium oxide nanoparticles synthesized present the intensity for the Ce-O scattering smaller than the corresponding intensity of the CeO_2 standard case. It is associated to the small size of the synthesized nanoparticles in comparison to the CeO_2 standard besides possibly a smaller coordination number of the Ce-O scattering path. Moreover, it is possible to observe a shoulder in the Ce-O contribution at small distances for all the cerium oxide

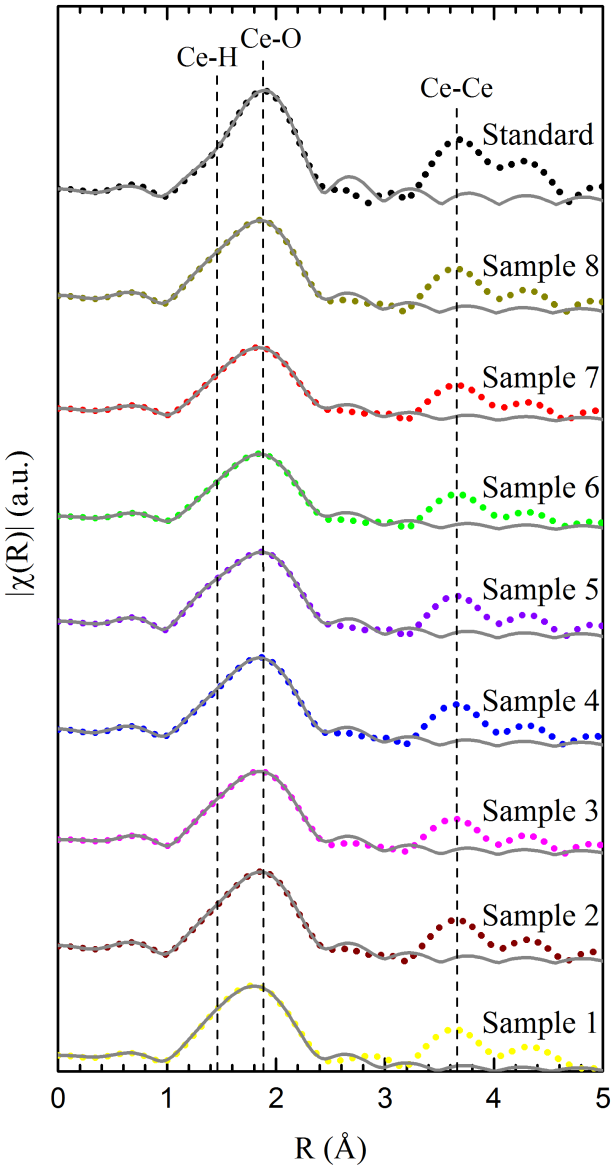

Figure 5.4.3 – Fourier transform of the EXAFS oscillations of the measured X-ray absorption spectra for each sample. The points correspond to the experimental data. The gray solid line corresponds to the fitting obtained.

nanoparticles synthesized although not for the CeO_2 standard case. Aiming to ensure that this shoulder was not created artificially by the MPE correction procedure, the FT of the EXAFS oscillations of the standard sample and the synthesized samples before and after the MPE correction were compared. As an example, Figure 5.4.4 presents this comparison for the standard sample and sample 5. It is possible to observe that before the MPE correction (Figure 5.4.4(a)) the FT of the EXAFS oscillations of the sample 5 present a shoulder around 1.4 Å (no phase correction) in comparison to the standard sample. This shoulder still remains after the MPE correction (Figure 5.4.4(b)), which indicates that this shoulder is not related to the MPE correction procedure. This behaviour is observed for all synthesized CeO_2 nanoparticles. Moreover, aiming to investigate the

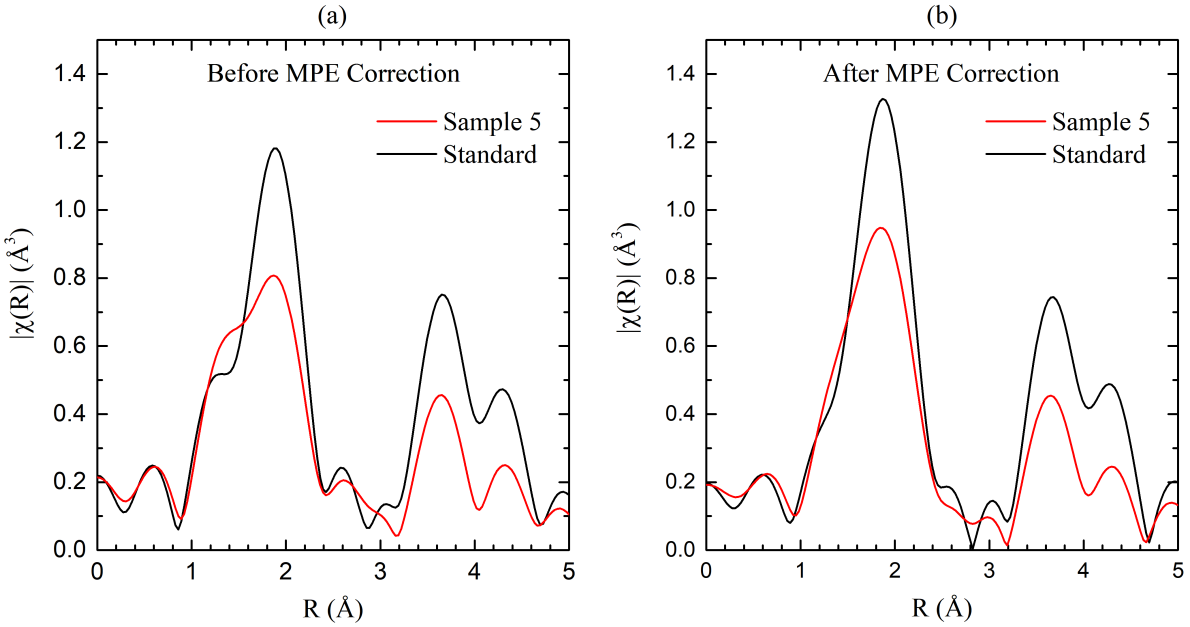

Figure 5.4.4 – Fourier transform of the EXAFS oscillations of the measured X-ray absorption spectra for standard sample and sample 5 (a) before and (b) after the MPE correction.

possibility of this shoulder be caused by non-Gaussian structural disorder presented in the synthesized CeO_2 nanoparticles, the cumulant expansion method [123] was considered in the fitting procedure. However, the FT of the EXAFS oscillations of some samples could not be adjusted satisfactorily using this method. Even the FT of the EXAFS oscillations of the samples that were adjusted satisfactorily presented inconsistent parameters. The samples that showed lower (higher) structural disorder, observed by the Debye-Waller factor, presented higher (lower) corrections due to non-Gaussian structural disorder. This result allowed one to decide that the use of this method is inappropriate in this case. Then, in order to take into account the contribution at this shoulder and adjust the FT of the EXAFS oscillations of the synthesised samples correctly, a Ce-H scattering path was included in the fitting procedure. For sure, it is not possible to affirm by analyzing the FT of the EXAFS oscillations that there is indeed a Ce-H scattering but at least it is possible to affirm that there is a Ce-X scattering at this distance, where X stands for some light element. It is quite possible that there is a mixture of possible light elements (C, H, etc) around this position that is simplified in the fitting using a single Ce-H scattering. The ΔE_0 value found from the fitting performed varied from (5.9 ± 0.2) eV to (8.1 ± 0.2) eV. Table 5.6 presents the other parameters obtained. In this table it is possible to observe the values obtained for the coordination number (N), distance from the absorbing atom to the scattering atom (R) and the Debye-Waller factor (σ^2) for the Ce-O and Ce-H scattering paths. For the Ce-O scattering path, the best fitting was obtained fixing the N parameter to the value associated to the sample's Ce(III) fraction obtained from the XANES analysis (Ξ^{XANES}), where $\Xi^{XANES} = 0$ corresponds to N = 8.0 and $\Xi^{XANES} = 1$

Table 5.6 – Parameters obtained from the fitting of the EXAFS region. For the Ce-H scattering path, the uncertainties obtained in the fit procedure for the R and σ^2 values are around 0.01 Å and 0.7 × 10^{-3} Å^{-1}, respectively. For the Ce-O scattering path, the uncertainties obtained in the fit procedure for the R and σ^2 values are around 0.002 Å and 0.3 × 10^{-3} Å^{-1}, respectively. The Ce-O distance calculated from the Rietveld refinement results is shown as well.

Sample	Ce-H Scattering Path			Ce-O Scattering Path			$R^{XRD}_{\text{Ce-O}}$ (Å)
	N	R (Å)	σ^2 (10^{-3} Å^{-1})	N	R (Å)	σ^2 (10^{-3} Å^{-1})	
1	4 ± 1	1.65	9.1	7.64	2.304	9.3	2.348
2	4 ± 1	1.66	9.1	7.79	2.323	8.5	2.347
3	4 ± 1	1.67	9.1	7.64	2.320	9.4	2.347
4	4 ± 1	1.66	9.1	7.76	2.321	8.9	2.347
5	4.4 ± 0.9	1.64	9.1	7.76	2.333	9.8	2.345
6	2.9 ± 0.8	1.70	9.1	7.57	2.313	10.2	2.347
7	3.5 ± 0.6	1.71	9.1	7.52	2.306	10.2	2.345
8	4.0 ± 0.9	1.64	9.1	7.75	2.326	8.3	2.345
Standard	0.00	-	-	8.00	2.317	4.1	2.342

corresponds to N = 4.0. It gives a coordination number close to 8.0, that corresponds to the fully oxidized case. This result, again, is consistent with the XRD results where a small Ξ value can be found in the bulk region of the samples. The R parameter value was obtained for each case from the fitting and can be compared with the lattice parameter (a) obtained from the XRD analysis. By considering the fluorite-type crystalline structure of CeO_2, the Ce-O distance ($R^{XRD}_{\text{Ce-O}}$) can be obtained from the Rietveld refinement results using the following equation:

$$R^{XRD}_{\text{Ce-O}} = \sqrt{3\left(\frac{a}{4}\right)^2} \tag{5.2}$$

The $R^{XRD}_{\text{Ce-O}}$ results are shown in Table 5.6. It is possible to observe that the $R^{XRD}_{\text{Ce-O}}$ values are always longer than the $R_{\text{Ce-O}}$ values obtained by the EXAFS analysis. This indicates anomalies in the crystal structure of cerium oxide, as already reported in the literature [124]. Kossoy *et al.* [124] investigated the Ce-O bond length of the CeO_2 and oxygen deficient cerium oxide ($CeO_{1.95}$ and $CeO_{1.90}$) thin films by means of XRD and EXAFS measurements. It was observed that the Ce-O bond length of the $CeO_{1.95}$ and $CeO_{1.90}$ derived from the EXAFS analysis was significantly shorter than that derived from the XRD analysis. The authors attribute this difference to the O vacancies present in the structure which do not contribute to the Ce-O bond length derived from the EXAFS analysis but do affect the Ce-O bond length derived from the XRD analysis. Moreover, it

was concluded that the $CeO_{1.95}$ and $CeO_{1.90}$ crystalline structures present a deviation from the fluorite-type crystalline structure of the CeO_2, but not great enough to be detectable in the XRD measurements. This deviation is caused by the presence of the O vacancies in the structure that move the nearest Ce ion neighbours outwards while the O atoms of the second layer are moved inwards toward the O vacancy, creating a compression strain in the crystalline structure. Note that the $CeO_{1.95}$ sample used in [124] corresponds to around 0.10 of the Ce(III) fraction, consistent with the results obtained by the XANES analysis shown in Table 5.5.

The Debye-Waller (σ^2) parameter value presents a significant difference between the cerium oxide nanoparticles. The standard sample presents the lower σ^2 value between the cerium oxide nanoparticles, indicating that this sample presents the lower structural disorder. This result is consistent with the result obtained for the cerium oxide nanoparticles from the XRD analysis by comparing the strain of the standard sample with the strain of the synthesized nanoparticles. Furthermore, it is not possible to observe a direct relation between the σ^2 values obtained from the EXAFS analysis and the strain obtained from the XRD analysis, as reported by Kossoy *et al.* [124].

Another interesting relation can be observed in Figure 5.4.5, that presents the Debye-Waller factor of the Ce-O scattering ($\sigma^2_{\text{Ce-O}}$) obtained by the EXAFS analysis as a function of the direct band gap energies of the cerium oxide nanoparticles. It is possible to observe that these two parameters present a great correlation. The higher the Debye-Waller factor of the Ce-O scattering, the lower the band gap energy. In the literature, it is possible to find a similar behaviour for hydrogenated amorphous silicon. Cody *et al.* [125] studied the effects of the thermal and structural disorder on the optical absorption edge of hydrogenated amorphous silicon by means of transmission, reflectivity and photoconductivity measurements. The authors found that the thermal and structural disorder of the system is directly related with its band gap energy. Moreover, the authors proposed a theoretical model to describe the data where the band gap energy presents a linear dependence with the thermal and structural disorder of the material. The thermal disorder contribution is described by approximating the phonon spectrum of the material by an Einstein oscillator with a characteristic temperature. The structural disorder contribution is described as the mean-square deviation of the atomic positions from a perfectly ordered configuration. By using this theoretical model, the authors concluded that the band gap energy is determined by the degree of thermal and structural disorder in the lattice. The higher the disorder, the lower the band gap energy presented for the studied system. The same qualitative relation is obtained here but probably with a different function relating the Debye-Waller factor and the band gap energies. This kind of relation is not found for the cerium oxide in the literature.

The Ce-H scattering path had to be added in order to adjust the coordination shell of the FT of the EXAFS oscillations of the synthesized cerium oxide nanoparticles. The N

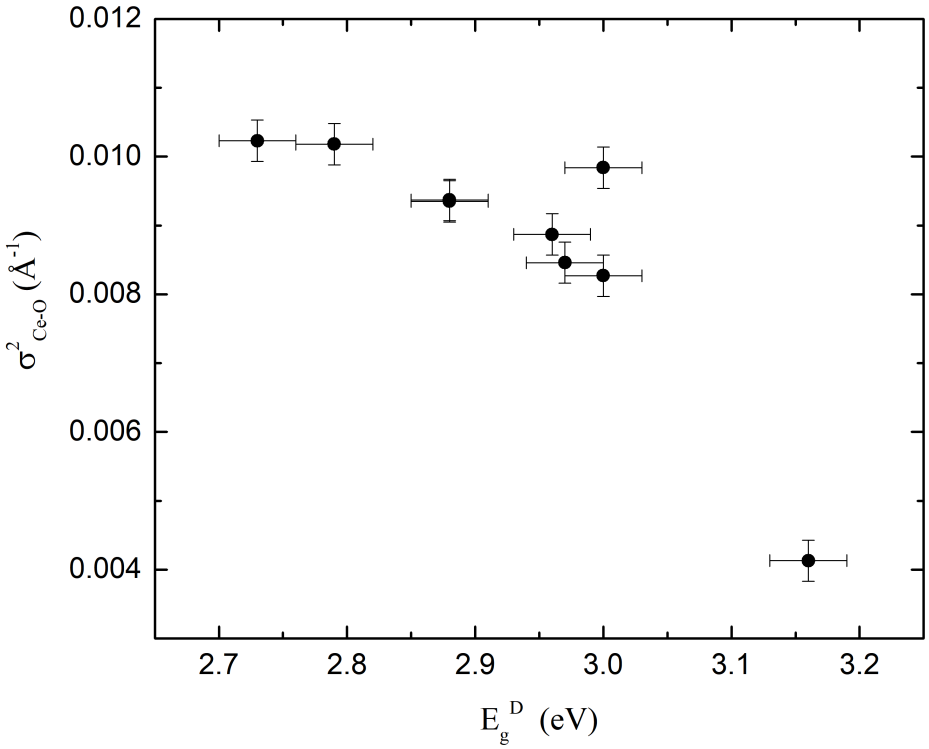

Figure 5.4.5 – Debye-Waller factor of the Ce-O scattering ($\sigma^2_{\text{Ce-O}}$) obtained by the analysis of EXAFS oscillations as a function of the direct band gap energies of the cerium oxide nanoparticles.

and R parameters values were obtained for each sample from the fitting and, considering the uncertainty associated to these parameters, the values obtained are practically the same for all the cerium oxide nanoparticles where this scattering path was added. The σ^2 parameter value was constrained to the same value for all the nanoparticles where this scattering path was added. This scattering path is consistent with the presence of an atom of a light element in the interstitial region of the CeO_2 crystal structure. The presence of this light element possibly contributes for the higher σ^2 and strain values presented by the synthesized cerium oxide nanoparticles in comparison to the standard sample. Aiming to corroborate this result, the samples were characterized by means of Fourier Transform Infrared (FTIR) Spectroscopy.

5.5 Fourier Transform Infrared (FTIR) Spectroscopy Results

The FTIR spectra represent the transmittance percentage of the incident radiation through the samples as a function of the wavenumber of the incident radiation. When the incident radiation matches the wavenumber that corresponds to a vibrational mode of the atoms, the transmittance percentage reaches a minimum in the spectra forming what is called an absorption band. In general, the absorption band position of each vibrational mode depends on the bond strength and reduced mass of the atoms involved in this vibration. The stronger the bonding between these atoms, the higher the required wavenumber to excite the correspondent vibrational mode. Also, the higher the reduced mass of these atoms, the lower the required wavenumber to cause the correspondent vibrational mode.

Figure 5.5.1 presents the FTIR spectra with a wavenumber interval from 400 cm^{-1} to 1000 cm^{-1}. There it found important contributions around 550 cm^{-1} and 500 cm^{-1}. For the standard sample, the absorption band at around 550 cm^{-1} is assigned to the Ce-O stretching vibration [126–128]. For the other samples, the same contribution can be observed shifted to around 500 cm^{-1}. This shift occurs when the bond strength between Ce and O atoms becomes weaker. Therefore, this result is consistent with the presence of an atom in the interstitial region in the cerium oxide crystalline structure, that agrees with the result obtained by means of the EXAFS analysis. Note that the wavenumber shift occurs for all the synthesized nanoparticles, as obtained from the EXAFS analysis. The full FTIR spectra (not shown here) presents evidences of organic compounds containing H atoms at the nanoparticles but the analysis of the detailed composition is out of the scope of this work. Nevertheless, the presence of organic compounds containing H atoms is expected also from the synthesis procedure described in the previous work [22].

The results shown contributed for elucidating the electronic and structural properties observed but it still does not explain fully the different photocatalytic activities obtained by the cerium oxide nanoparticles. Aiming to obtain an explanation for the photocatalytic results, the Ce(III) fraction was investigated at the surface of the cerium oxide nanoparticles.

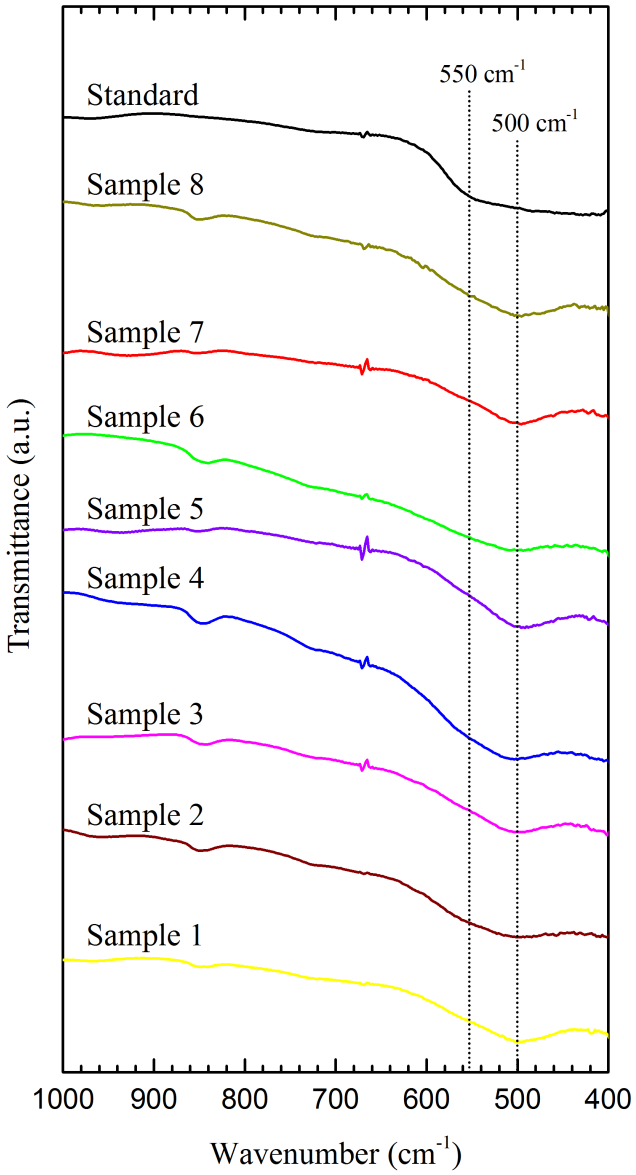

Figure 5.5.1 – FTIR spectra of the cerium oxide nanoparticles from 400 cm^{-1} to 1000 cm^{-1}. The dotted lines indicate the absorption bands associated to the Ce-O stretching vibration present at 550 cm^{-1} for the standard sample and around 500 cm^{-1} for the other nanoparticles.

5.6 X-ray Photoelectron Spectroscopy (XPS) and Ultraviolet Photoelectron Spectroscopy (UPS) Results

In the long scan spectrum of the cerium oxide nanoparticles synthesized, not shown here, all the samples present a very similar spectrum among them, where it is possible to observe the photoelectric and Auger lines coming from the Ce, C and O atoms, as expected and without contamination.

Figure 5.6.1 presents the XPS spectra at the Ce 3d region with the samples measured before the thermal treatment at 120 °C (Ce 3d RT). The fitting of the spectrum for each

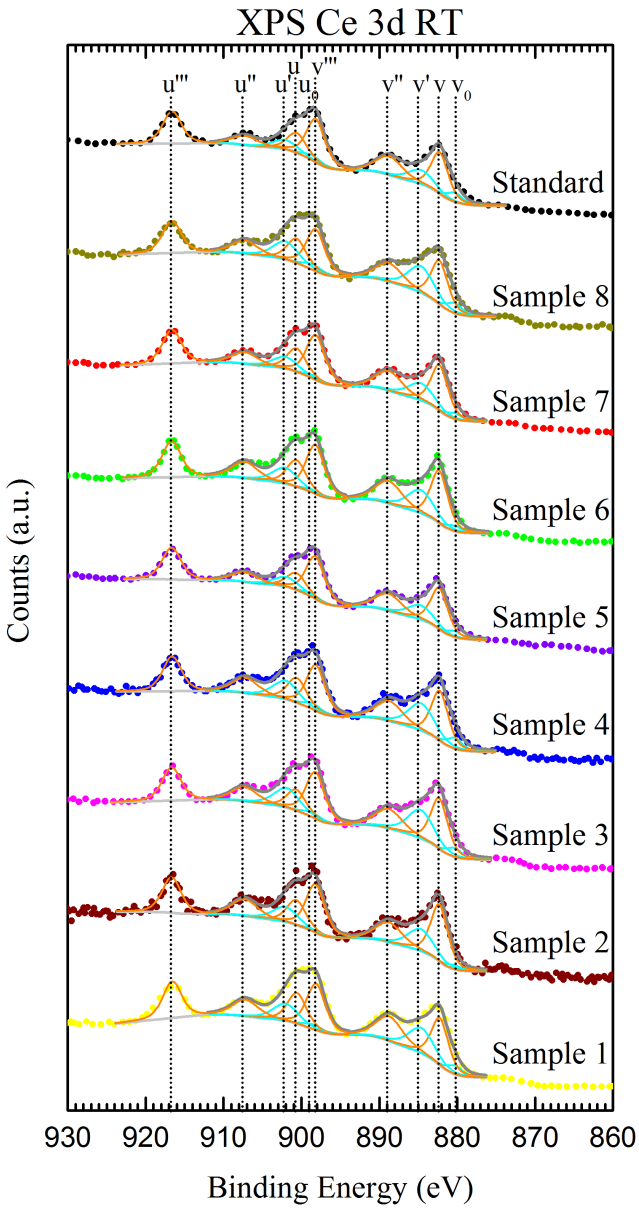

Figure 5.6.1 – XPS spectra at the Ce 3d region measured before the thermal treatment at 120 °C. The fitting of the spectrum for each sample and the identification of each contribution used in the fitting are presented. The orange and cyan peaks correspond to the Ce(IV) and Ce(III) components, respectively.

sample and the identification of each contribution used in the fitting are shown as well. By using the TPP-2M formula [77], the inelastic mean free path (λ_{IMFP}) of the photoelectrons coming from the Ce 3d region is around 8 Å. A qualitative analysis of the Ξ value in each sample can be performed observing the u”’ contribution. This contribution around 916 eV comes from the Ce(IV) component, where a higher intensity corresponds to a lower Ξ value. Therefore, by comparing the relative intensity of this contribution between spectra, it is possible to observe that the u”’ contribution has a small variance in intensity between the spectra, indicating that the Ξ value in each sample is slightly different. The result of the quantitative analysis obtained for Ξ^{XPS} values by fitting the Ce 3d RT spectra is

presented in Table 5.7. It is possible to observe that the Ξ^{XPS} value is slightly different between the samples, in agreement with the qualitative analysis, and assumes values from 0.20 to 0.29. These Ξ^{XPS} values are higher than those obtained from the XANES and XRD analysis, which is expected since the XPS analysis probes the surface region of the nanoparticles. In principle, the Ξ^{XPS} value in this case may comes from the presence of O vacancies or even organic molecules adsorbed at the surface, then changing the Ce(IV) oxidation state to Ce(III) oxidation state. In spite of this, it presumably comes from the O vacancies present at the surface since the organic molecules typically interacts with the cerium oxide surface by filling the O vacancies with O atoms from the molecule [129].

Table 5.7 – Ce(III) fraction (Ξ^{XPS}) obtained by means of the XPS analysis of the Ce 3d and Ce 4d regions. The results obtained by the analysis performed with the samples measured before (after) the thermal treatment at 120 °C is indicated by the RT (120 °C).

Sample	Ξ^{XPS} Ce 3d RT $\lambda_{IMFP} = 8$ Å	Ξ^{XPS} Ce 3d 120 °C $\lambda_{IMFP} = 8$ Å	Ξ^{XPS} Ce 4d 120 °C $\lambda_{IMFP} = 18$ Å
1	0.25	0.45	0.18
2	0.21	0.53	0.48
3	0.28	0.52	0.39
4	0.28	0.44	0.37
5	0.20	0.37	0.32
6	0.22	0.39	0.21
7	0.20	0.34	0.17
8	0.29	0.39	0.27
Standard	0.21	0.28	0.07

Figure 5.6.2 presents the XPS spectra of the Ce 3d region with the samples measured after the thermal treatment at 120 °C (Ce 3d 120 °C). As performed for the Ce 3d RT spectra, by comparing the relative intensity of the isolated contribution around 916 eV is possible to observe a significant variance between the spectra, indicating that the Ξ^{XPS} value in each sample is significantly different. The XPS spectrum of the standard sample seems to present the highest relative intensity of this contribution (lowest Ξ^{XPS} value). The quantitative Ξ^{XPS} value results obtained by fitting the XPS spectra are presented in Table 5.7. It is possible to observe a more important variation on the Ξ^{XPS} values than those obtained from the Ce 3d RT spectra, where the standard sample presents the smallest Ξ^{XPS} value (0.28) and the samples 2 and 3 present the highest Ξ^{XPS} value (0.53 and 0.52). This difference in the Ξ^{XPS} value results between the samples measured before and after thermal treatment can be explained if considering the presence of organic compounds, like hydrocarbons, on the samples surface before the thermal treatment. It comes from the synthesis procedure and due to the exposition to the atmosphere. The thermal

treatment allowed cleaning the samples surface and the cerium oxide nanoparticles could be probed without interference of organic compounds.

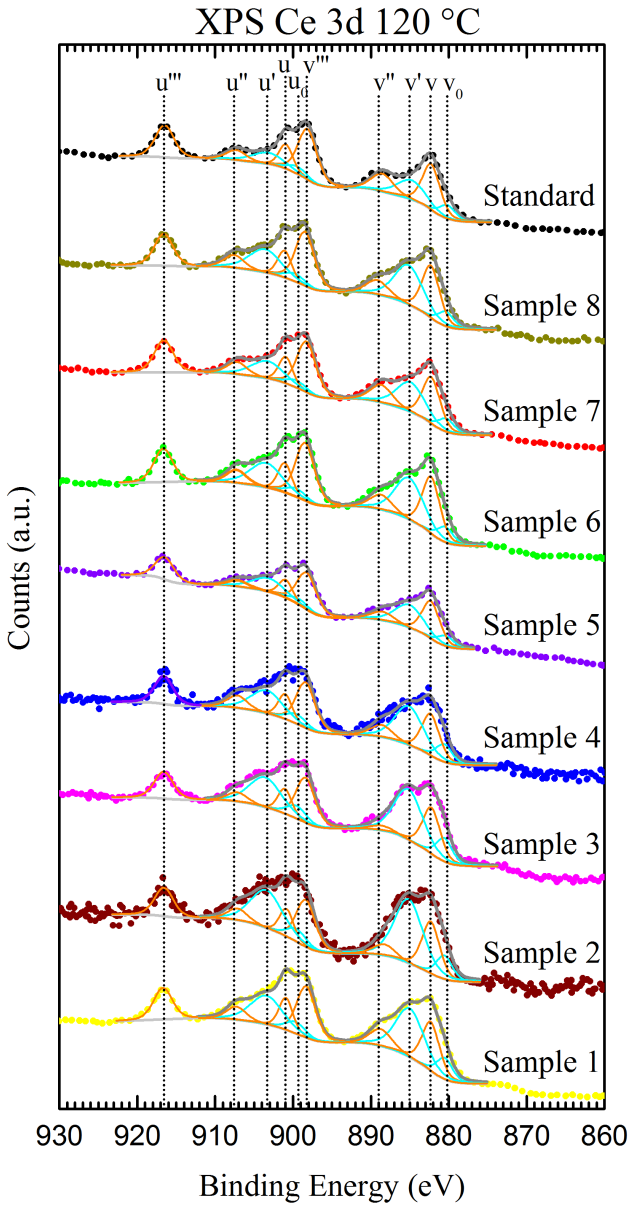

Figure 5.6.2 – XPS spectra at the Ce 3d region of the cerium oxide samples measured after thermal treatment at 120 °C. The adjustment of the spectrum for each sample and the identification of each contribution used in the adjustment are presented. The orange and cyan peaks correspond to the Ce(IV) and Ce(III) components, respectively.

Figure 5.6.3 presents the XPS spectra at the Ce 4d region with the samples measured after the thermal treatment at 120 °C (Ce 4d 120 °C). By using the TPP-2M formula [77], the inelastic mean free path (λ_{IMFP}) of the photoelectrons coming from the Ce 4d region is around 18 Å. The two contributions corresponding to the Ce(IV) oxidation state can be observed at the binding energy values around 122 eV and 125 eV. A qualitative analysis of the Ξ^{XPS} value in each sample can be performed observing the relative intensity of

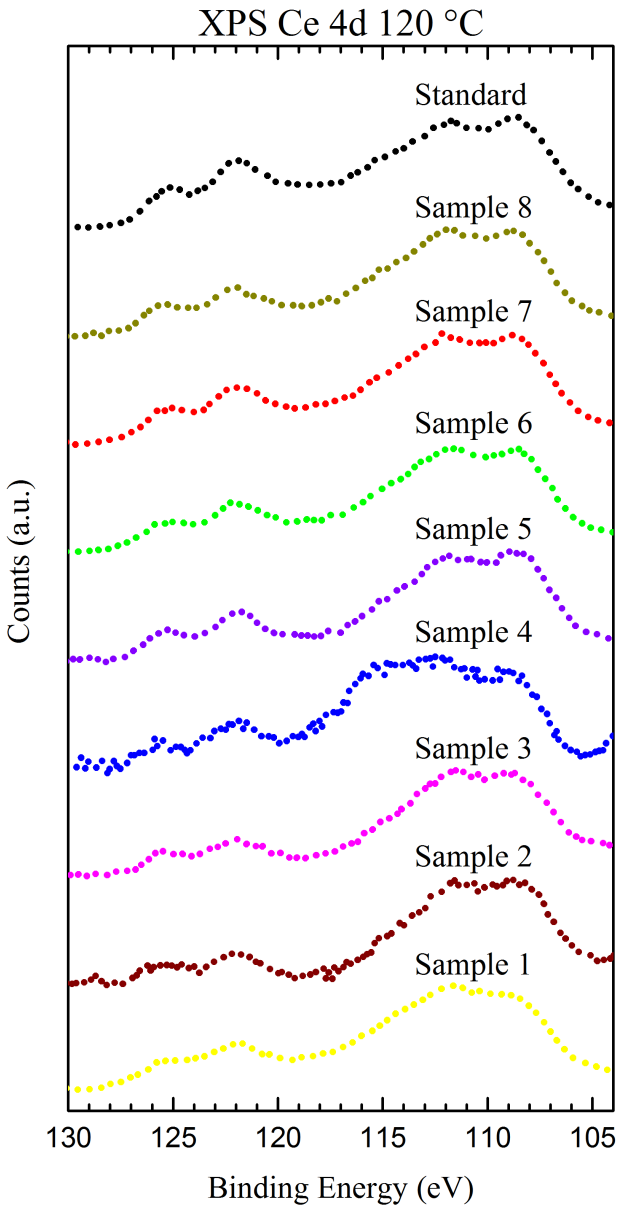

Figure 5.6.3 – XPS spectra at the Ce 4d region of the cerium oxide samples measured after the thermal treatment at 120 °C.

these two contributions, where a high relative intensity corresponds to a low Ξ^{XPS} value. By comparing the relative intensity of these two contributions between the spectra it is possible to observe a variation on the Ξ^{XPS} value, where the standard sample seems to present the lowest Ξ^{XPS} value while the sample 2 seems to present the highest Ξ^{XPS} value. The result of the quantitative analysis obtained for the Ce 4d spectra after thermal treatment at 120 °C is presented in Table 5.7. It is possible to observe a significant variation on the Ξ^{XPS} value between the samples. The standard sample presents the lowest Ξ^{XPS} value (0.07) while sample 2 presents the highest Ξ^{XPS} value (0.48), in accordance to the qualitative analysis. Moreover, each sample presents a Ξ^{XPS} value lower than the Ξ^{XPS} value obtained by the analysis of the Ce 3d XPS spectrum after thermal treatment

at 120 °C. Since the photoelectrons from the Ce 4d electronic region have a higher λ_{IMFP} than those from the Ce 3d region (18 Å versus 8 Å), it is possible to conclude that there is a gradient of O vacancies for all the samples, where there are more O vacancies in the region closer to the surface. This behaviour is in agreement with that observed in the previous work [22], where the reductive behaviour of these cerium oxide nanoparticles was probed in situ by NAP-XPS and time-resolved XANES measurements during reduction of the nanoparticles by exposition to a CO atmosphere. The reduction process starts with the surface reduction, where an O atom is removed leaving behind two localized electrons in the 4f orbital of two Ce atoms, thus turning Ce(IV) into Ce(III) and creating an O vacancy at the surface. When the surface is fully reduced and due to the gradient in the O vacancy population, O atoms move through the nanoparticle from the inner region to the surface region by the vacancy hopping mechanism [130]. This process continues until the full nanoparticle is reduced.

The UPS measurements could only be performed after thermal treatment at 120 °C, when the samples surface was clean, because the UPS technique probes only the very first atomic layers of the nanoparticles. By using the TPP-2M formula [77], the inelastic mean free path (λ_{IMFP}) of the photoelectrons coming from the valence region in the UPS measurements is around 3 Å. Figure 5.6.4 presents the UPS spectra of the samples measured after the thermal treatment and two other spectra taken from the literature [131] for comparative purposes to represent the Ce(III) and Ce(IV) standards. In Figure 5.6.4 it is possible to observe that the UPS spectrum of the Ce(IV) standard consists of two contributions at around 10.5 eV and 16 eV. These two contributions are associated with O 2p orbitals that are hybridized with Ce 4f and Ce 5d orbitals, respectively [132]. For the Ce(III) standard, a single contribution can be observed at 3 eV which is assigned to the emission from the localized Ce 4f orbital [133, 134]. By comparing the UPS spectra of the samples, it is possible to observe that hybridized states change, which indicates differences in the oxidation state. However, all the nanoparticles do not present the contribution assigned to the localized Ce 4f orbital. Therefore, the samples do not present occupied states in the localized Ce 4f orbital in the Ce atoms at the surface, where the reaction occurs. Note that this information complements that obtained from XANES analysis (Figure 5.4.2) where is observed an increasing occupation of the Ce 4f orbital with the decrease of the band gap energy in the bulk region of the samples. Since there are very few achievements in the literature which analyse quantitatively the UPS spectra of the cerium oxide and all of them use Ce(III) and Ce(IV) standards in order to fit the data, it was not possible to obtain a reliable method aiming to analyse quantitatively the UPS spectra of the cerium oxide nanoparticles presented in this work.

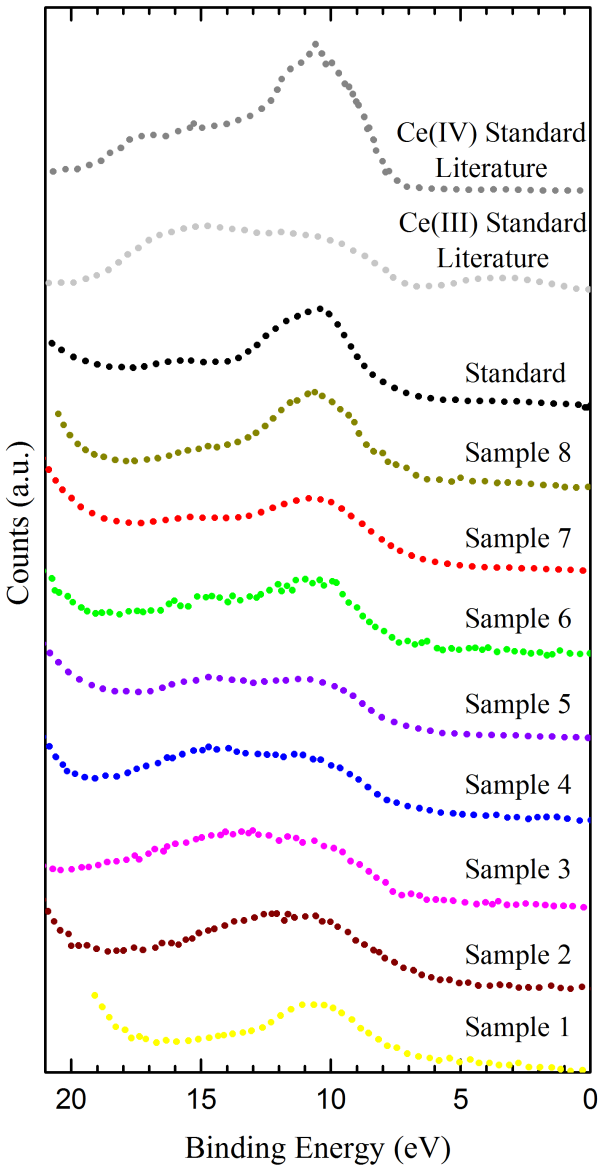

Figure 5.6.4 – UPS spectra of the cerium oxide samples measured after the thermal treatment at 120 °C. The two spectra at the top were taken from the literature [131] and represent the Ce(III) and Ce(IV) standards.

In order to determine the influence of the surface Ce(III) fraction (Ξ^{XPS}) in the H_2 evolution photocatalytic activity, figure 5.6.5 shows the H_2 evolution photocatalytic activity normalized by the surface area as a function of the Ξ^{XPS} values obtained from the XPS analysis of Ce 3d region ($\lambda_{IMFP} = 8$ Å) measured before the thermal treatment at 120 °C. The XPS results obtained were used before the thermal treatment since it represents the condition of the cerium oxide nanoparticles before the photocatalytic reaction. It is possible to observe that there is an approximately linear behaviour between these two parameters presented for the cerium oxide nanoparticles that do not present mesopores at the surface (black circles). The higher the Ξ^{XPS} value at the cerium oxide surface, the higher the photocatalytic activity normalized by the surface area. Since the thermal

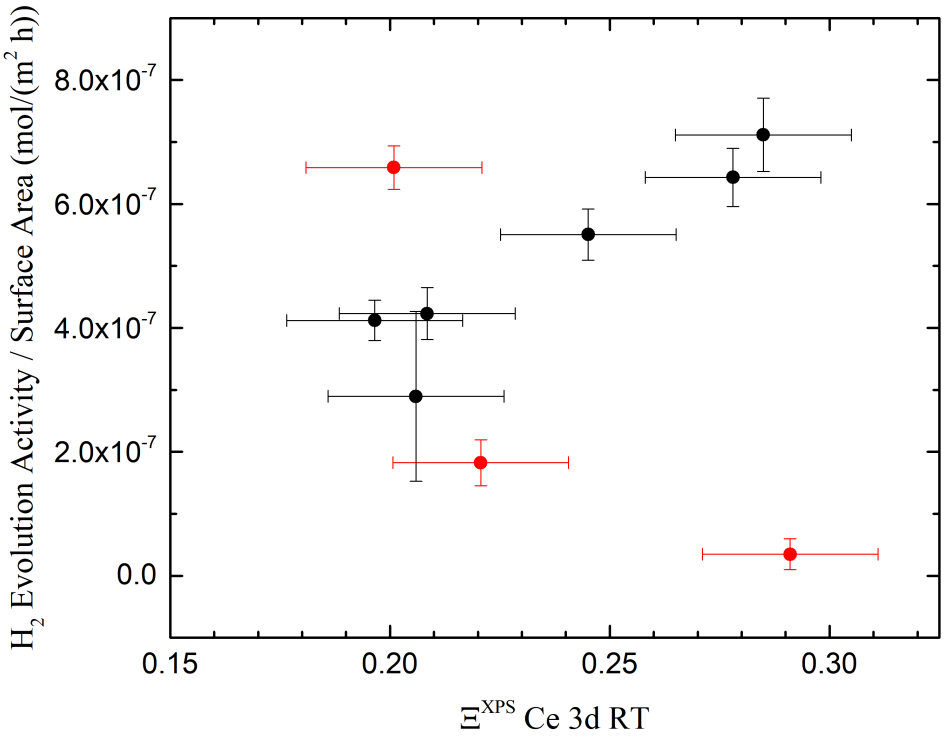

Figure 5.6.5 – H_2 evolution photocatalytic activity normalized by the surface area as a function of the Ξ^{XPS} values obtained from the XPS analysis of Ce 3d region (λ_{IMFP} = 8 Å) of the cerium oxide nanoparticles measured before the thermal treatment at 120 °C. The red circles correspond to the samples that present mesopores on the surface.

treatment at 120 °C increased the Ξ^{XPS} value at the surface of the nanoparticles, it shows that part of the O vacancies were filled with organic molecules that left the sample surface with the thermal energy. The remaining were available for the photocatalytic reaction. As mentioned in Chapter 2, defects such as O vacancies are one of the most reactive sites in metallic oxides and very important in the photocatalytic water splitting reaction acting as adsorption sites for the water molecule. However, these defects are potential traps that present a big probability to prevent the migration of charges through the recombination process. Therefore, an optimum amount of O vacancies present in the nanoparticles surface that maximize the reaction efficiency is expected to exist. Kong *et al.* [135] studied the effect of defects on the photocatalytic activity by synthesizing TiO_2 nanocrystals with tunable bulk/surface ratio of O vacancies. The samples were characterized by using TEM, XRD, BET, positron annihilation, and photocurrent measurements. The authors found that decreasing the relative concentration ratio of bulk defects to surface defects in TiO_2 nanocrystals improves the electron-hole pair separation efficiency, decreasing the recombination probability and improving the photocatalytic efficiency. It is in agreement with the results shown in Figure 5.6.5 where a high Ξ^{XPS} value improves the photocatalytic activity results. It is important to stress that it is valid for the Ξ^{XPS} values range used in this work and perhaps there is an optimum value for the Ξ^{XPS} different from

the maximum Ξ^{XPS} value possible. In fact, it occurs for other catalytic reactions, such as the CO oxidation, involving O vacancies at the surface of cerium oxide nanoparticles, as shown recently in [136]. However, it is possible to observe a completely different behaviour in the cerium oxide nanoparticles that present mesopores at the surface (red circles) in Figure 5.6.5. For these cerium oxide nanoparticles, an abrupt increase on the photocatalytic activity values is observed when decreasing the Ξ^{XPS} values. Again, there are several possible mathematical functions that can be adjusted in these 3 points and one possible function is the exponential one. Figure 5.6.6 shows a model proposed to explain this result. Nanoparticle A and B represent nanoparticles with and without the presence of mesopores. For both cases, there is a gradient of the O vacancy population from the surface to the bulk region of the sample (as observed from the XPS, XANES and XRD results). Since the mesopores have a typical size comparable with the nanoparticle size (see Figure 5.6.6), the region I in nanoparticle A is closer to the center of the nanoparticle than the region II of the nanoparticle B. By assuming that the O vacancies distribution through the depth occurs equally for both cases, there is a higher O vacancy density in the nanoparticle A than nanoparticle B. Therefore, an electron-hole pair created in the inner region of the nanoparticle diffuses through the nanoparticle to the surface region. For the nanoparticle A, there is a higher probability of the electron to be trapped by the O vacancies and suffer recombination, decreasing the photocatalytic activity. Then, a high O vacancy concentration in this case is not good for the photocatalytic activity. On the other hand, if the O vacancy population is very low in the nanoparticle surface (small Ξ^{XPS} value), an electron that is excited in the inner region diffuses to the surface and presents a small probability to be trapped and suffer recombination. Furthermore, since the inner region below the nanoparticle A surface is closer to the center of the nanoparticle than in the nanoparticle B, the distance diffused by the electron is smaller, that also decreases the probability of recombination and increases the photocatalytic activity. On the other hand, the nanoparticle B presents a small O vacancy concentration in the inner region of the nanoparticle, giving a small probability of electron-hole recombination. Consequently, the higher the O vacancy population at the surface the higher the photocatalytic activity as there are more active sites for the H_2O adsorption.

Figure 5.2.2 showed the dependence of the H_2 evolution photocatalytic activity normalized by the surface area with the band gap energy. Certainly, the smaller the band gap energy the higher the photocatalytic activity. Now it is important also to investigate the relative importance between the Ξ^{XPS} values in the cerium oxide surface and the direct band gap energies of the cerium oxide nanoparticles on the H_2 evolution photocatalytic activity. Figure 5.6.7 shows a graph of the H_2 evolution photocatalytic activity normalized by the surface area as a function of the Ξ^{XPS} values obtained from the XPS analysis of Ce 3d region ($\lambda_{IMFP} = 8$ Å) of the samples before the thermal treatment at 120 °C divided by the direct band gap energies. It is possible to observe the same mathemat-

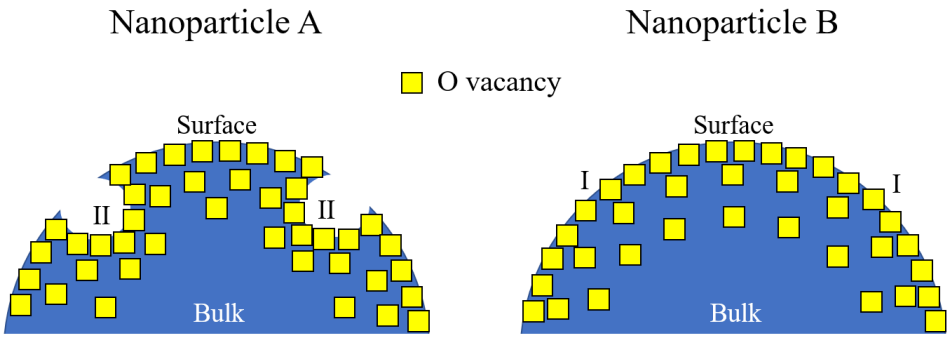

Figure 5.6.6 – Schematic representation nanoparticles with (Nanoparticle A) and without (Nanoparticle B) the presence of mesopores. The regions I and II as shown as well. The yellow squares represent the O vacancies.

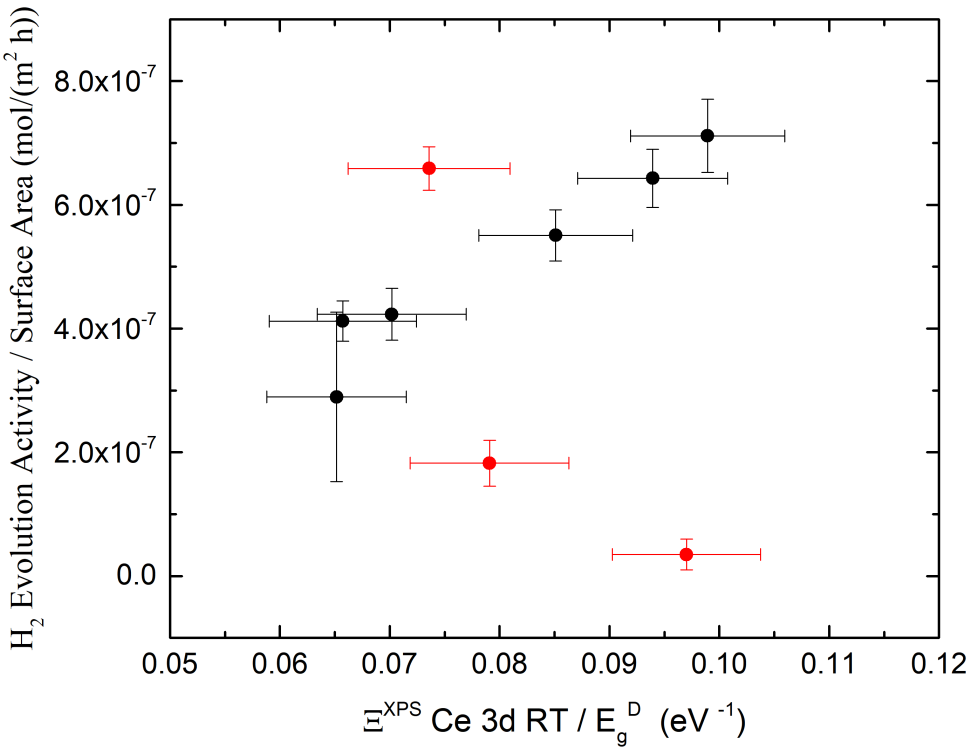

Figure 5.6.7 – H_2 evolution photocatalytic activity normalized by the surface area as a function of the Ξ^{XPS} values obtained from the XPS analysis of Ce 3d region ($\lambda_{IMFP} = 8$ Å) of the cerium oxide nanoparticles measured before the thermal treatment at 120 °C divided by the direct band gap energy for the cerium oxide nanoparticles. The red circles correspond to the samples that present mesopores on the surface.

ical behaviour presented in Figure 5.6.5. In the the cerium oxide nanoparticles that do not present mesopores at the surface (black circles), an approximately linear behaviour is observed where the higher the Ξ^{XPS} Ce 3d RT/E_g^D ratio, the higher the H_2 evolution photocatalytic activity normalized by the surface area. It shows the same importance of both E_g^D and Ξ^{XPS} Ce 3d RT values in the photocatalytic activity. For the cerium ox-

ide nanoparticles that present mesopores at the surface (red circles), the same previous mathematical behaviour is observed where the higher the Ξ^{XPS} Ce 3d RT/E_g^D ratio, the lower the H_2 evolution photocatalytic activity normalized by the surface area. Note that, in this case, it shows that the Ξ^{XPS} Ce 3d RT value plays a more important role for the photocatalytic activity than the band gap energies. That is, for cerium oxide nanoparticles with mesoporous at the surface the fundamental parameter to be controlled is the Ξ^{XPS} Ce 3d RT. It elucidates in great details the role played by different parameters during the H_2 evolution photocatalytic activity reaction. However, it is important to stress out that, since the photocatalyst properties are determined for complicated correlations between the synthesis parameters, there is no clear relation between a given synthesis parameter and the photocatalyst properties. The band gap energy dependence with the Ce 4f orbital occupation was shown in Section 5.4.2 but should be explained in details. Then, DFT calculations were employed with this purpose.

5.7 Density Functional Theory (DFT) Results

5.7.1 Cerium Oxide Bulk Results

In order to study the bulk electronic density of states (DOS) of the cerium oxide with the presence of O vacancies, the DFT calculations were performed using 48 atoms (16 Ce atoms and 32 O atoms) in the fluorite-type crystalline structure of CeO_2 with zero, one and two O vacancies. The lattice parameters obtained from the relaxation calculations for the cases with zero, one and two O vacancies are 5.413 Å, 5.440 Å and 5.464 Å, respectively. It is possible to observe that the lattice parameter value increases with the number of vacancies. This behaviour is well known for the cerium oxide and agrees with experimental results [122,124]. Moreover, since the CeO_2 is the cerium oxide fully oxidized case and the Ce_2O_3 is the cerium oxide fully reduced case, one O vacancy in the 48 atoms corresponds to a Ξ value of 0.125. Analogously, two O vacancies in the 48 atoms of cerium oxide corresponds to a Ξ value of 0.25. These values are in great agreement with the Ξ values of 0.117 and 0.221 obtained by Kim's equation [122] using the lattice parameter values obtained in the relaxation procedure. The electronic DOS is presented in Figure 5.7.1 for each case. The case with zero O vacancies presents a localized and unoccupied Ce 4f orbital. The band gap energy between the O 2p and Ce 4f states is around 1.55 eV for this case. As it is well known from the literature [112, 114, 137], this calculated band gap energy is usually underestimated if compared with the experimental values, that is around 3.0 eV. For the cases with one and two O vacancies it is possible to observe that the Fermi energy position shifts and the Ce 4f orbital becomes partially filled, where the case with two O vacancies present more occupied Ce 4f states than the case with one O vacancy. The band gap energy between the O 2p and Ce 4f electronic states for the cases

with one and two O vacancies is 1.55 eV and 1.70 eV, respectively. These results show that the presence of O vacancies increases the occupation of the Ce 4f orbital and the O 2p → Ce 4f band gap energy increases as well. It is in accordance to the XANES results presented in Figure 5.4.2. Even considering that the cerium oxide nanoparticles do not present a significant Ξ value in the bulk region, the occupation of the Ce 4f orbital changes between the different nanoparticles. This variation is related to the measured direct band gap energy of the cerium oxide nanoparticles, where the higher the direct band gap energy the higher the occupation of the Ce 4f orbital.

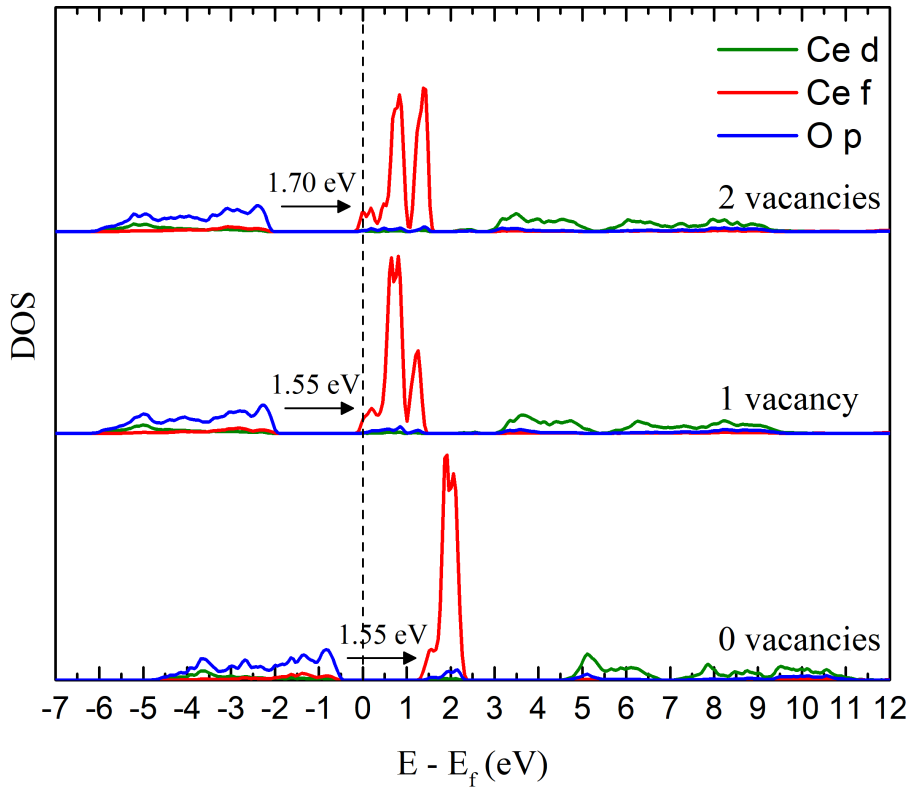

Figure 5.7.1 – Bulk electronic density of states (DOS) of cerium oxide for the cases with zero, one and two vacancies. The electronic orbitals of Ce and O atoms are indicated. The vertical dotted line indicates the Fermi energy position.

5.7.2 Cerium Oxide(111) Surface Results

In order to study the surface electronic density of states (DOS) of the cerium oxide with the presence of O vacancies, the DFT calculations were performed using 36 atoms (12 Ce atoms and 24 O atoms) in the fluorite-type crystalline structure of CeO_2, in the (111) orientation with zero, one and two O vacancies. The (111) orientation was chosen as it is a more stable one [117–119]. The electronic DOS for the cerium oxide (111) surface is presented in Figure 5.7.2 for each case. The case with zero O vacancies presents a localized and unoccupied Ce 4f orbital, very similar to the result obtained for the cerium oxide bulk. The band gap energy between the O 2p and Ce 4f electronic states is approximately 1.70

eV for this case, significantly greater than the band gap energy obtained for the bulk cerium oxide with zero vacancies, but still underestimating the experimental value. For the cases with one and two O vacancies it is possible to observe that the Fermi energy shifts and the Ce 4f orbital becomes partially filled, where the case with two O vacancies present more occupied Ce 4f states than the case with one O vacancy, as observed for the cerium oxide bulk as well. The band gap energy between the O 2p and Ce 4f electronic states for the cases with one and two O vacancies is 1.65 eV and 1.40 eV, respectively. These results show that the presence of O vacancies increases the occupation of the Ce 4f orbital and the O 2p $\rightarrow$ Ce 4f band gap energy decreases, which is the opposite trend obtained for the bulk calculations. Then, it is important to consider since the increase of the O vacancy population at the surface of the nanoparticles gives a secondary good effect of decreasing the band gap energy, then helping on the photocatalytic activity results. Moreover, it is possible to observe that the Ce f electronic states that coexist with the O p electronic states below the Fermi energy decrease when the O vacancies increase. This behaviour was observed in the UPS spectra of the cerium oxide nanoparticles, where the ratio of the two contributions that are associated with the O 2p orbitals hybridized with Ce 4f and Ce 5d orbitals varied between the different nanoparticles, indicating that the cerium oxide nanoparticles present a different amount of O vacancies (oxidation state) at the surface. However, even the cerium oxide nanoparticles presenting a different amount of O vacancies at the surface, the contribution corresponding to the localized Ce 4f orbital is not observed in the UPS spectra. It is explained by the low occupation of the Ce 4f electronic state, as shown in the DOS calculation, then making difficult the detection of the photoelectrons coming from this electronic level. Finally, it is clear that the presence of molecules (like H_2O) at the surface may change significantly the DOS results as observed in the literature for the cerium oxide case [138]. The next step is to consider it in the calculations and verify the influence of the H_2O molecule adsorbed at the surface in the DOS.

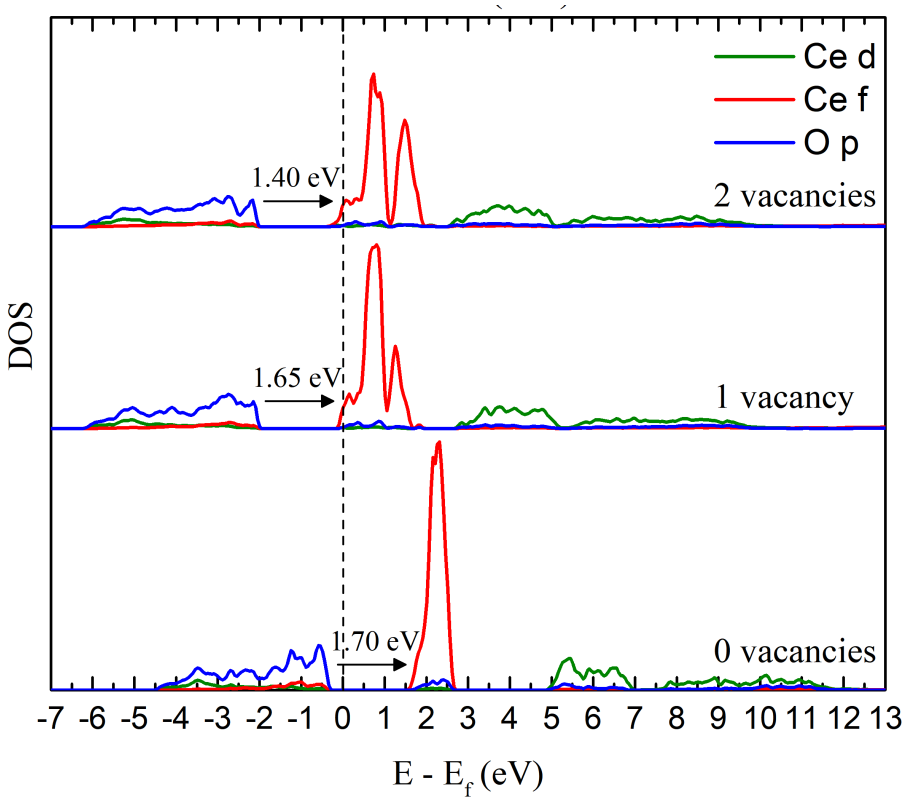

Figure 5.7.2 – Electronic density of states (DOS) of cerium oxide (111) surface for the cases with zero, one and two vacancies. The electronic orbitals of Ce and O atoms are indicated. The vertical dotted line indicates the Fermi energy position.

6 Conclusions and Perspectives

In this work, it was possible to tune the structural and electronic properties of cerium oxide nanoparticles in order to improve the efficiency of the H_2 production photocatalytic reaction. The influence of these properties in the photocatalytic activity was elucidated. The H_2 evolution photocatalytic activity of the synthesized nanoparticles was higher than the commercial cerium oxide standard, where the better case found reaches a H_2 evolution photocatalytic activity ten times higher than the commercial standard. In part, this improvement was obtained because the direct and indirect band gap energies of the synthesized cerium oxide nanoparticles was lower than those values obtained for the commercial standard. It was possible to observe that, in general, the lower the direct and indirect band gap energies, the higher the H_2 evolution photocatalytic activity. Furthermore, it was observed that the occupation of the Ce 4f orbital and the structural disorder of the cerium oxide nanoparticles present a direct relation with the direct and indirect band gap energies, where the lower the Ce 4f orbital occupation or the higher the structural disorder, the lower the band gap energy of the cerium oxide nanoparticles.

Moreover, it was possible to conclude that the O vacancy population at the surface of the cerium oxide nanoparticles synthesized play a major role in the H_2 evolution photocatalytic activity. For the nanoparticles that present only micropores in the structure, it was observed that the higher the O vacancy population at the surface the higher the H_2 evolution photocatalytic activity. On the other hand, for the nanoparticles that present micropores and mesopores in the structure, the opposite behaviour was observed. The lower the O vacancy population at the surface the higher the H_2 evolution photocatalytic activity. In special, the O vacancy population plays a major role in the H_2 evolution photocatalytic activity, being more important than the band gap energies for the nanoparticles with the presence of mesopores. These results elucidate the main properties of the cerium oxide nanoparticles that can improve effectively the H_2 production photocatalytic activity and shown that the cerium oxide nanoparticles synthesized are very promising to this reaction.

The future work is planned considering the study of the influence of the H_2O molecules in the DOS by DFT calculations, which is important to consider for a more realistic case. Also, the results of H_2 evolution photocatalytic activity are very promising when compared to the typical values found in the literature obtained for light sources of higher power. Moreover, in this work, the simple case of cerium oxide nanoparticles with ethanol as sacrificial agent was used. In fact, it is possible to improve even more the results found, by using an optimized co-catalyst and sacrificial agent, which will be investigated in the future.

A Publications and Presentations

A.1 Published Articles

Thill, A. S., Kilian, A. S., Bernardi, F. (2017). Key role played by metallic nanoparticles on the ceria reduction. *The Journal of Physical Chemistry C*, 121(45), 25323-25332.

Della Mea, G. B., Matte, L. P., Thill, A. S., Lobato, F. O., Benvenutti, E. V., Arenas, L. T., Jürgensen, A., Hergenröder, R., Poletto, F., Bernardi, F. (2017). Tuning the oxygen vacancy population of cerium oxide (CeO2-x, $0 < x < 0.5$) nanoparticles. *Applied Surface Science*, 422, 1102-1112.

Bohn, D. R., Lobato, F. O., Thill, A. S., Steffens, L., Raabe, M., Donida, B., Vargas, C. R., Moura, D. J., Bernardi, F., Poletto, F. (2018). Artificial cerium-based proenzymes confined in lyotropic liquid crystals: synthetic strategy and on-demand activation. *Journal of Materials Chemistry B*, 6, 4920-4928.

A.2 Congress Attendance and Presentations

Thill, A. S.; Lobato, F. O. ; Poletto, F. ; Teixeira, S. R. ; Bernardi, F. . Investigation of cerium oxide nanoparticles applied to the photocatalytic water splitting reaction. In: XVI Encontro da SBPMat, 2017, Gramado. Investigation of cerium oxide nanoparticles applied to the photocatalytic water splitting reaction., 2017.

Matte, L. P. ; Thill, A. S. ; Lobato, F. O. ; Poletto, F. ; Bernardi, F. . Characterization of Cu/CeO2 nanoparticles applied to the CO oxidation reaction.. In: XVI Encontro da SBPMat, 2017, Gramado. Characterization of Cu/CeO2 nanoparticles applied to the CO oxidation reaction., 2017.

Thill, A. S.; Kilian, A. S. ; Bernardi, F. . Elucidating the influence of metallic nanoparticles on the CeO2 reduction properties.. In: XVI Encontro da SBPMat, 2017, Gramado. Elucidating the influence of metallic nanoparticles on the CeO2 reduction properties., 2017.

Bibliography

[1] `https://www.iea.org/publications/freepublications/publication/KeyWorld2017.pdf`. Accessed: June 6^{th}, 2018.

[2] NOCERA, D. G. On the future of global energy. *Daedalus*, v. 135, n. 4, p. 112–115, 2006.

[3] TWIDELL, J.; WEIR, T. *Renewable energy resources*. Routledge, 2015.

[4] ROSEN, M. A.; KOOHI-FAYEGH, S. The prospects for hydrogen as an energy carrier: an overview of hydrogen energy and hydrogen energy systems. *Energy, Ecology and Environment*, v. 1, n. 1, p. 10–29, 2016.

[5] ABBOTT, D. Keeping the energy debate clean: How do we supply the world's energy needs? *Proceedings of the IEEE*, v. 98, n. 1, p. 42–66, 2010.

[6] NOCERA, D. G. Fast food energy. *Energy & Environmental Science*, v. 3, n. 8, p. 993–995, 2010.

[7] HOLLADAY, J. D.; HU, J.; KING, D. L.; WANG, Y. An overview of hydrogen production technologies. *Catalysis Today*, v. 139, n. 4, p. 244–260, 2009.

[8] MIDILLI, A.; DINCER, I. Hydrogen as a renewable and sustainable solution in reducing global fossil fuel consumption. *International Journal of Hydrogen Energy*, v. 33, n. 16, p. 4209–4222, 2008.

[9] TURNER, J. A. Sustainable hydrogen production. *Science*, Washington, v. 305, n. 5686, p. 972–974, 2004.

[10] BALAT, M. Potential importance of hydrogen as a future solution to environmental and transportation problems. *International Journal of Hydrogen Energy*, v. 33, n. 15, p. 4013–4029, 2008.

[11] ZÜTTEL, A. Materials for hydrogen storage. *Materials Today*, v. 6, n. 9, p. 24–33, 2003.

[12] GREGORY, D. P. The hydrogen economy. *Scientific American*, v. 228, n. 1, p. 13–21, 1973.

[13] SCHLAPBACH, L.; ZÜTTEL, A. Hydrogen-storage materials for mobile applications. In: *Materials for Sustainable Energy: A Collection of Peer-Reviewed Research and Review Articles from Nature Publishing Group*. World Scientific, 2011. p. 265–270.

[14] YAMAKATA, A.; ISHIBASHI, T.-A.; ONISHI, H. Kinetics of the photocatalytic water-splitting reaction on TiO2 and Pt/TiO2 studied by time-resolved infrared absorption spectroscopy. *Journal of Molecular Catalysis A: Chemical*, v. 199, n. 1-2, p. 85–94, 2003.

[15] DOMEN, K.; NAITO, S.; SOMA, M.; ONISHI, T.; TAMARU, K. Photocatalytic decomposition of water vapour on an NiO-SrTiO3 catalyst. *Journal of the Chemical Society, Chemical Communications*, , n. 12, p. 543–544, 1980.

[16] YE, J.; ZOU, Z.; MATSUSHITA, A. A novel series of water splitting photocatalysts NiM2O6 (M= Nb, Ta) active under visible light. *International Journal of Hydrogen Energy*, v. 28, n. 6, p. 651–655, 2003.

[17] PRIMO, A.; MARINO, T.; CORMA, A.; MOLINARI, R.; GARCIA, H. Efficient visible-light photocatalytic water splitting by minute amounts of gold supported on nanoparticulate CeO2 obtained by a biopolymer templating method. *Journal of the American Chemical Society*, Washington, v. 133, n. 18, p. 6930–6933, 2011.

[18] TROVARELLI, A. Catalytic properties of ceria and CeO2-containing materials. *Catalysis Reviews*, v. 38, n. 4, p. 439–520, 1996.

[19] MURRAY, E. P.; TSAI, T.; BARNETT, S. A. A direct-methane fuel cell with a ceria-based anode. *Nature*, London, v. 400, n. 6745, p. 649, 1999.

[20] MANSILLA, C. Structure, microstructure and optical properties of cerium oxide thin films prepared by electron beam evaporation assisted with ion beams. *Solid State Sciences*, v. 11, n. 8, p. 1456–1464, 2009.

[21] THILL, A. S.; KILIAN, A. S.; BERNARDI, F. Key role played by metallic nanoparticles on the ceria reduction. *The Journal of Physical Chemistry C*, v. 121, n. 45, p. 25323–25332, 2017.

[22] DELLA MEA, G. B.; MATTE, L. P.; THILL, A. S.; LOBATO, F. O.; BENVENUTTI, E. V.; ARENAS, L. T.; JÜRGENSEN, A.; HERGENRÖDER, R.; POLETTO, F.; BERNARDI, F. Tuning the oxygen vacancy population of cerium oxide (CeO2-x, $0 < x < 0.5$) nanoparticles. *Applied Surface Science*, v. 422, p. 1102–1112, 2017.

[23] `http://www.environment.gov.au/climate-change/climate-science-data/climate-science/greenhouse-effect`. Accessed: June 6^{th}, 2018.

[24] COLLINS, M.; AN, S.-I.; CAI, W.; GANACHAUD, A.; GUILYARDI, E.; JIN, F.-F.; JOCHUM, M.; LENGAIGNE, M.; POWER, S.; TIMMERMANN, A. et al. The impact of global warming on the tropical pacific ocean and el niño. *Nature Geoscience*, v. 3, n. 6, p. 391, 2010.

[25] MCDONALD, M. E.; HERSHEY, A. E.; MILLER, M. C. Global warming impacts on lake trout in arctic lakes. *Limnology and Oceanography*, v. 41, n. 5, p. 1102–1108, 1996.

[26] CHOU, C.; CHEN, C.-A.; TAN, P.-H.; CHEN, K. T. Mechanisms for global warming impacts on precipitation frequency and intensity. *Journal of Climate*, v. 25, n. 9, p. 3291–3306, 2012.

[27] STOCKER, T. *Climate change 2013: the physical science basis: Working group i contribution to the fifth assessment report of the intergovernmental panel on climate change*. Cambridge University Press, 2014.

[28] HOFFERT, M. I.; CALDEIRA, K.; JAIN, A. K.; HAITES, E. F.; HARVEY, L. D. D.; POTTER, S. D.; SCHLESINGER, M. E.; SCHNEIDER, S. H.; WATTS, R. G.; WIGLEY, T. M. L. et al. Energy implications of future stabilization of atmospheric CO2 content. *Nature*, London, v. 395, n. 6705, p. 881, 1998.

[29] FOSTER, R.; GHASSEMI, M.; COTA, A. *Solar energy: renewable energy and the environment*. CRC Press, 2009.

[30] FUJISHIMA, A.; HONDA, K. Electrochemical photolysis of water at a semiconductor electrode. *Nature*, London, v. 238, n. 5358, p. 37, 1972.

[31] MOLINARI, R.; MARINO, T.; ARGURIO, P. Photocatalytic membrane reactors for hydrogen production from water. *International Journal of Hydrogen Energy*, v. 39, n. 14, p. 7247–7261, 2014.

[32] KUDO, A.; MISEKI, Y. Heterogeneous photocatalyst materials for water splitting. *Chemical Society Reviews*, v. 38, n. 1, p. 253–278, 2009.

[33] HARRIMAN, A.; GRATZEL, M. Energy resources through photochemistry and catalysis. *Academic Press, New York*, p. 163, 1983.

[34] PLESKOV, Y. V.; GUREVICH, Y. Y. Semiconductor photoelectrochemistry. 1 1986.

[35] MECHERIKUNNEL, A. T.; RICHMOND, J. Spectral distribution of solar radiation. *NASA Technical Report*, 1980.

[36] KIM, J.; HWANG, D. W.; KIM, H. G.; BAE, S. W.; LEE, J. S.; LI, W.; OH, S. H. Highly efficient overall water splitting through optimization of preparation and operation conditions of layered perovskite photocatalysts. *Topics in Catalysis*, v. 35, n. 3-4, p. 295–303, 2005.

[37] KUDO, A.; KATO, H.; NAKAGAWA, S. Water splitting into H2 and O2 on new Sr2M2O7 (M= Nb and Ta) photocatalysts with layered perovskite structures: factors affecting the photocatalytic activity. *The Journal of Physical Chemistry B*, v. 104, n. 3, p. 571–575, 2000.

[38] IWASE, A.; KATO, H.; KUDO, A. Nanosized Au particles as an efficient cocatalyst for photocatalytic overall water splitting. *Catalysis Letters*, v. 108, n. 1-2, p. 7–10, 2006.

[39] MISEKI, Y.; KATO, H.; KUDO, A. Water splitting into H2 and O2 over Ba5Nb4O15 photocatalysts with layered perovskite structure prepared by polymerizable complex method. *Chemistry Letters*, v. 35, n. 9, p. 1052–1053, 2006.

[40] SAYAMA, K.; ARAKAWA, H. Effect of Na2CO3 addition on photocatalytic decomposition of liquid water over various semiconductor catalysis. *Journal of Photochemistry and Photobiology A: Chemistry*, v. 77, n. 2-3, p. 243–247, 1994.

[41] KATO, H.; KUDO, A. New tantalate photocatalysts for water decomposition into H2 and O2. *Chemical Physics Letters*, Amsterdam, v. 295, n. 5-6, p. 487–492, 1998.

[42] SATO, J.; KOBAYASHI, H.; INOUE, Y. Photocatalytic activity for water decomposition of indates with octahedrally coordinated d10 configuration. II. roles of geometric and electronic structures. *The Journal of Physical Chemistry B*, v. 107, n. 31, p. 7970–7975, 2003.

[43] IKARASHI, K.; SATO, J.; KOBAYASHI, H.; SAITO, N.; NISHIYAMA, H.; INOUE, Y. Photocatalysis for water decomposition by RuO2-dispersed ZnGa2O4 with d10 configuration. *The Journal of Physical Chemistry B*, v. 106, n. 35, p. 9048–9053, 2002.

[44] YANAGIDA, T.; SAKATA, Y.; IMAMURA, H. Photocatalytic decomposition of H2O into H2 and O2 over Ga2O3 loaded with NiO. *Chemistry Letters*, v. 33, n. 6, p. 726–727, 2004.

[45] REDDY, J. K.; SURESH, G.; HYMAVATHI, C. H.; KUMARI, V. D.; SUBRAHMANYAM, M. Ce (III) species supported zeolites as novel photocatalysts for hydrogen production from water. *Catalysis Today*, v. 141, n. 1-2, p. 89–93, 2009.

[46] NI, M.; LEUNG, M. K. H.; LEUNG, D. Y. C.; SUMATHY, K. A review and recent developments in photocatalytic water-splitting using TiO2 for hydrogen production. *Renewable and Sustainable Energy Reviews*, v. 11, n. 3, p. 401–425, 2007.

[47] ABE, R.; SAYAMA, K.; ARAKAWA, H. Significant effect of iodide addition on water splitting into H2 and O2 over Pt-loaded TiO2 photocatalyst: suppression of

backward reaction. *Chemical Physics Letters*, Amsterdam, v. 371, n. 3-4, p. 360–364, 2003.

[48] CHOI, W.; TERMIN, A.; HOFFMANN, M. R. The role of metal ion dopants in quantum-sized TiO2: correlation between photoreactivity and charge carrier recombination dynamics. *The Journal of Physical Chemistry*, v. 98, n. 51, p. 13669–13679, 1994.

[49] TU, W.; ZHOU, Y.; ZOU, Z. Photocatalytic conversion of CO2 into renewable hydrocarbon fuels: state-of-the-art accomplishment, challenges, and prospects. *Advanced Materials*, v. 26, n. 27, p. 4607–4626, 2014.

[50] KAWAI, T.; SAKATA, T. Hydrogen evolution from water using solid carbon and light energy. *Nature*, London, v. 282, n. 5736, p. 283, 1979.

[51] KAWAI, T.; SAKATA, T. Conversion of carbohydrate into hydrogen fuel by a photocatalytic process. *Nature*, London, v. 286, n. 5772, p. 474, 1980.

[52] KAWAI, T.; SAKATA, T. Photocatalytic hydrogen production from water by the decomposition of poly-vinylchloride, protein, algae, dead insects, and excrement. *Chemistry Letters*, v. 10, n. 1, p. 81–84, 1981.

[53] CAMPBELL, C. T.; PEDEN, C. H. F. Oxygen vacancies and catalysis on ceria surfaces. *Science*, Washington, v. 309, n. 5735, p. 713–714, 2005.

[54] YAO, H. C.; YAO, Y. F. Y. Ceria in automotive exhaust catalysts: I. oxygen storage. *Journal of Catalysis*, v. 86, n. 2, p. 254–265, 1984.

[55] MATTE, L. P.; KILIAN, A. S.; LUZA, L.; ALVES, M. C. M.; MORAIS, J.; BAPTISTA, D. L.; DUPONT, J.; BERNARDI, F. Influence of the CeO2 support on the reduction properties of Cu/CeO2 and Ni/CeO2 nanoparticles. *The Journal of Physical Chemistry C*, v. 119, n. 47, p. 26459–26470, 2015.

[56] DE FIGUEIREDO, W. T. *Elucidation of catalytic events at atomic level in CuxNi1-x/CeO2 (0<x<1) nanoparticles applied to the reverse water-gas shift (RWGS) reaction.* 2017. Dissertação (Mestrado em Física) - 2017.

[57] MELCHIONNA, M.; FORNASIERO, P. The role of ceria-based nanostructured materials in energy applications. *Materials Today*, v. 17, n. 7, p. 349–357, 2014.

[58] SUN, C.; LI, H.; CHEN, L. Nanostructured ceria-based materials: synthesis, properties, and applications. *Energy & Environmental Science*, v. 5, n. 9, p. 8475–8505, 2012.

[59] CHUEH, W. C.; FALTER, C.; ABBOTT, M.; SCIPIO, D.; FURLER, P.; HAILE, S. M.; STEINFELD, A. High-flux solar-driven thermochemical dissociation of CO2 and H2O using nonstoichiometric ceria. *Science*, Washington, v. 330, n. 6012, p. 1797–1801, 2010.

[60] ISSARAPANACHEEWIN, S.; WETCHAKUN, K.; PHANICHPHANT, S.; KANGWANSUPAMONKON, W.; WETCHAKUN, N. A novel CeO2/Bi2WO6 composite with highly enhanced photocatalytic activity. *Materials Letters*, v. 156, p. 28–31, 2015.

[61] MAGESH, G.; VISWANATHAN, B.; VISWANATH, R. P.; VARADARAJAN, T. K. Photocatalytic behavior of CeO2-TiO2 system for the degradation of methylene blue. *Indian Journal of Chemistry*, v. 48A, p. 480–488, 2009.

[62] ABDULLAH, H.; KHAN, M. R.; PUDUKUDY, M.; YAAKOB, Z.; ISMAIL, N. A. CeO2-TiO2 as a visible light active catalyst for the photoreduction of CO2 to methanol. *Journal of Rare Earths*, v. 33, n. 11, p. 1155–1161, 2015.

[63] HARANI, R.; HOGARTH, C. A. Optical absorption of cerium phosphate glasses. *Journal of Materials Science Letters*, v. 4, n. 4, p. 399–402, 1985.

[64] SATHYAMURTHY, S.; LEONARD, K. J.; DABESTANI, R. T.; PARANTHAMAN, M. P. Reverse micellar synthesis of cerium oxide nanoparticles. *Nanotechnology*, v. 16, n. 9, p. 1960, 2005.

[65] LI, W.; XIE, S.; LI, M.; OUYANG, X.; CUI, G.; LU, X.; TONG, Y. CdS/CeOx heterostructured nanowires for photocatalytic hydrogen production. *Journal of Materials Chemistry A*, v. 1, n. 13, p. 4190–4193, 2013.

[66] CHUNG, K.-H.; PARK, D.-C. Water photolysis reaction on cerium oxide photocatalysts. *Catalysis Today*, v. 30, n. 1-3, p. 157–162, 1996.

[67] SHINDE, A.; LI, G.; ZHOU, L.; GUEVARRA, D.; SURAM, S. K.; TOMA, F. M.; YAN, Q.; HABER, J. A.; NEATON, J. B.; GREGOIRE, J. M. The role of the CeO2/BiVO4 interface in optimized Fe-Ce oxide coatings for solar fuels photoanodes. *Journal of Materials Chemistry A*, v. 4, n. 37, p. 14356–14363, 2016.

[68] KATO, H.; KUDO, A. Photocatalytic reduction of nitrate ions over tantalate photocatalysts. *Physical Chemistry Chemical Physics*, v. 4, n. 12, p. 2833–2838, 2002.

[69] SAYAMA, K.; ARAKAWA, H. Effect of carbonate salt addition on the photocatalytic decomposition of liquid water over Pt-TiO2 catalyst. *Journal of the Chemical Society, Faraday Transactions*, v. 93, n. 8, p. 1647–1654, 1997.

[70] LU, X.; ZHAI, T.; CUI, H.; SHI, J.; XIE, S.; HUANG, Y.; LIANG, C.; TONG, Y. Redox cycles promoting photocatalytic hydrogen evolution of CeO2 nanorods. *Journal of Materials Chemistry*, v. 21, n. 15, p. 5569–5572, 2011.

[71] NIEMANTSVERDRIET, J. W. *Spectroscopy in catalysis: An introduction, third, completely revised and enlarged edition.* WILEY-VCH Verlag GmbH & Co. KGaA, Weinheim, 2007.

[72] CULLITY, B. D. *Elements of x-ray diffraction; second edition.* Ed. Addinson-Wesley Publishing Company, Inc., 1978.

[73] DINNEBIER, R. E.; BILLINGE, S. J. L. E. *Powder diffraction: theory and practice.* Royal Society of Chemistry, 2008.

[74] `https://physics.nist.gov/cgi-bin/Xcom/xcom2`. Accessed: June 6^{th}, 2018.

[75] BRUNDLE, C. R.; BAKER, A. D. *Electron spectroscopy: Theory, techniques and applications.* Academic Press, 1977. v. 1.

[76] WAGNER, C. D.; RIGGS, W. M.; DAVIS, L. E.; MOULDER, J. F.; MUILENBERG, G. E. *Handbook of x-ray photoelectron spectroscopy: a reference book of standard data for use in x-ray photoelectron spectroscopy.* Perkin-Elmer, 1979.

[77] TANUMA, S.; POWELL, C. J.; PENN, D. R. Calculations of electron inelastic mean free paths. V. Data for 14 organic compounds over the 50-2000 eV range. *Surface and Interface Analysis*, v. 21, n. 3, p. 165–176, 1994.

[78] WATTS, J. F.; WOLSTENHOLME, J. *An introduction to surface analysis by XPS and AES.* WILEY-VCH, 2003.

[79] KONINGSBERGER, D. C.; PRINS, R. *X-ray absorption: principles, applications, techniques of EXAFS, SEXAFS, and XANES.* Wiley-Interscience, 1988.

[80] SHRIVASTAVA, B. D. X-ray absorption fine structure (XAFS) spectroscopy using synchrotron radiation. *Journal of Physics: Conference Series*, v. 365, n. 1, p. 012002, 2012.

[81] CODLING, K.; GUDAT, W.; KOCH, E. E.; KOTANI, A.; LYNCH, D. W.; ROWE, E. M.; SONNTAG, B. F.; TOYOZAWA, Y. *Synchrotron radiation: techniques and applications.* Springer Science & Business Media, 2013. v. 10.

[82] MOBILIO, S.; BOSCHERINI, F.; MENEGHINI, C. *Synchrotron radiation: Basics, methods and applications.* Springer, 2016.

[83] BUNKER, G. *Introduction to XAFS: a practical guide to x-ray absorption fine structure spectroscopy.* Cambridge University Press, 2010.

[84] HOHENBERG, P.; KOHN, W. Inhomogeneous electron gas. *Physical Review*, New York, v. 136, n. 3B, p. B864, 1964.

[85] KOHN, W.; SHAM, L. J. Self-consistent equations including exchange and correlation effects. *Physical Review*, New York, v. 140, n. 4A, p. A1133, 1965.

[86] VIANA, J. D. M.; FAZZIO, A.; CANUTO, S. *Teoria quântica de moléculas e sólidos: Simulaçao computacional*. São Paulo, Editora Livraria da Física, 2004.

[87] WIGNER, E. *Trans. Faraday Soc.*, v. 34, p. 678, 1938.

[88] ANISIMOV, V. I.; ARYASETIAWAN, F.; LICHTENSTEIN, A. I. First-principles calculations of the electronic structure and spectra of strongly correlated systems: the LDA+U method. *Journal of Physics: Condensed Matter*, Bristol, v. 9, n. 4, p. 767, 1997.

[89] LIECHTENSTEIN, A. I.; ANISIMOV, V. I.; ZAANEN, J. Density-functional theory and strong interactions: Orbital ordering in mott-hubbard insulators. *Physical Review B*, v. 52, n. 8, p. R5467, 1995.

[90] DUDAREV, S. L.; BOTTON, G. A.; SAVRASOV, S. Y.; HUMPHREYS, C. J.; SUTTON, A. P. Electron-energy-loss spectra and the structural stability of nickel oxide: An LSDA+U study. *Physical Review B*, v. 57, n. 3, p. 1505, 1998.

[91] ROUQUEROL, J.; AVNIR, D.; FAIRBRIDGE, C. W.; EVERETT, D. H.; HAYNES, J. M.; PERNICONE, N.; RAMSAY, J. D. F.; SING, K. S. W.; UNGER, K. K. Recommendations for the characterization of porous solids (technical report). *Pure and Applied Chemistry*, Boca Raton, v. 66, n. 8, p. 1739–1758, 1994.

[92] FIGUEROA, S. J. A.; MAURICIO, J. C.; MURARI, J.; BENIZ, D. B.; PITON, J. R.; SLEPICKA, H. H.; DE SOUSA, M. F.; ESPÍNDOLA, A. M.; LEVINSKY, A. P. S. Upgrades to the XAFS2 beamline control system and to the endstation at the LNLS. *Journal of Physics: Conference Series*, v. 712, n. 1, p. 012022, 2016.

[93] TAUC, J.; GRIGOROVICI, R.; VANCU, A. Optical properties and electronic structure of amorphous germanium. *Physica Status Solidi (B)*, v. 15, n. 2, p. 627–637, 1966.

[94] TAUC, J. *Optical properties of solids by F. Abeles*. American Elsevier, 1972.

[95] DAVIS, E. A.; MOTT, N. F. Conduction in non-crystalline systems V. conductivity, optical absorption and photoconductivity in amorphous semiconductors. *Philosophical Magazine*, v. 22, n. 179, p. 0903–0922, 1970.

[96] YOUNG, R. A. *The rietveld method, International Union of Crystallography monographs on crystallography*. International Union of Crystallography, 1995. v. 5.

[97] MCCUSKER, L. B.; VON DREELE, R. B.; COX, D. E.; LOUËR, D.; SCARDI, P. Rietveld refinement guidelines. *Journal of Applied Crystallography*, v. 32, n. 1, p. 36–50, 1999.

[98] THOMPSON, P.; COX, D. E.; HASTINGS, J. B. Rietveld refinement of debye–scherrer synchrotron x-ray data from Al2O3. *Journal of Applied Crystallography*, v. 20, n. 2, p. 79–83, 1987.

[99] RODRÍQUEZ-CARVAJAL, J.; ROISNEL, T. Line broadening analysis using fullprof*: determination of microstructural properties. *Materials Science Forum*, v. 443, p. 123–126, 2004.

[100] ITOH, T.; MORI, M.; INUKAI, M.; NITANI, H.; YAMAMOTO, T.; MIYANAGA, T.; IGAWA, N.; KITAMURA, N.; ISHIDA, N.; IDEMOTO, Y. Effect of annealing on crystal and local structures of doped zirconia using experimental and computational methods. *The Journal of Physical Chemistry C*, v. 119, n. 16, p. 8447–8458, 2015.

[101] NEWVILLE, M. IFEFFIT: interactive XAFS analysis and FEFF fitting. *Journal of Synchrotron Radiation*, Copenhagen, v. 8, n. 2, p. 322–324, 2001.

[102] TAKAHASHI, Y.; SAKAMI, H.; NOMURA, M. Determination of the oxidation state of cerium in rocks by Ce LIII-edge x-ray absorption near-edge structure spectroscopy. *Analytica Chimica Acta*, v. 468, n. 2, p. 345–354, 2002.

[103] GOMILŠEK, J. P.; KODRE, A.; BUKOVEC, N.; ŠKOFIC, I. K. Atomic effects in EXAFS structural analysis of mixed Ce oxide thin films. *Acta Chimica Slovenica*, v. 51, p. 23–32, 2004.

[104] ZABINSKY, S. I.; REHR, J. J.; ANKUDINOV, A.; ALBERS, R. C.; ELLER, M. J. Multiple-scattering calculations of x-ray-absorption spectra. *Physical Review B*, v. 52, n. 4, p. 2995, 1995.

[105] KOTANI, A.; JO, T.; PARLEBAS, J. C. Many-body effects in core-level spectroscopy of rare-earth compounds. *Advances in Physics*, London, v. 37, n. 1, p. 37–85, 1988.

[106] SCHIERBAUM, K.-D. Ordered ultra-thin cerium oxide overlayers on Pt (111) single crystal surfaces studied by LEED and XPS. *Surface Science*, v. 399, n. 1, p. 29–38, 1998.

[107] BURROUGHS, P.; HAMNETT, A.; ORCHARD, A. F.; THORNTON, G. Satellite structure in the x-ray photoelectron spectra of some binary and mixed oxides of lanthanum and cerium. *Journal of the Chemical Society, Dalton Transactions*, , n. 17, p. 1686–1698, 1976.

[108] SHIRLEY, D. A. High-resolution x-ray photoemission spectrum of the valence bands of gold. *Physical Review B*, v. 5, n. 12, p. 4709, 1972.

[109] ZHANG, C.; GRASS, M. E.; YU, Y.; GASKELL, K. J.; DECALUWE, S. C.; CHANG, R.; JACKSON, G. S.; HUSSAIN, Z.; BLUHM, H.; EICHHORN, B. W. et al. Multielement activity mapping and potential mapping in solid oxide electrochemical cells through the use of operando XPS. *ACS Catalysis*, v. 2, n. 11, p. 2297–2304, 2012.

[110] GIANNOZZI, P.; BARONI, S.; BONINI, N.; CALANDRA, M.; CAR, R.; CAVAZZONI, C.; CERESOLI, D.; CHIAROTTI, G. L.; COCOCCIONI, M.; DABO, I. et al. QUANTUM ESPRESSO: a modular and open-source software project for quantum simulations of materials. *Journal of Physics: Condensed Matter*, Bristol, v. 21, n. 39, p. 395502, 2009.

[111] KRESSE, G.; JOUBERT, D. From ultrasoft pseudopotentials to the projector augmented-wave method. *Physical Review B*, v. 59, n. 3, p. 1758, 1999.

[112] CASTLETON, C. W. M.; KULLGREN, J.; HERMANSSON, K. Tuning LDA+U for electron localization and structure at oxygen vacancies in ceria. *The Journal of Chemical Physics*, v. 127, n. 24, p. 244704, 2007.

[113] FABRIS, S.; DE GIRONCOLI, S.; BARONI, S.; VICARIO, G.; BALDUCCI, G. Taming multiple valency with density functionals: a case study of defective ceria. *Physical Review B*, v. 71, n. 4, p. 041102, 2005.

[114] LOSCHEN, C.; CARRASCO, J.; NEYMAN, K. M.; ILLAS, F. First-principles LDA+U and GGA+U study of cerium oxides: Dependence on the effective U parameter. *Physical Review B*, v. 75, n. 3, p. 035115, 2007.

[115] LU, D.; LIU, P. Rationalization of the hubbard U parameter in CeOx from first principles: Unveiling the role of local structure in screening. *The Journal of Chemical Physics*, v. 140, n. 8, p. 084101, 2014.

[116] COCOCCIONI, M.; DE GIRONCOLI, S. Linear response approach to the calculation of the effective interaction parameters in the LDA+U method. *Physical Review B*, v. 71, n. 3, p. 035105, 2005.

[117] SAYLE, T. X. T.; PARKER, S. C.; CATLOW, C. R. A. The role of oxygen vacancies on ceria surfaces in the oxidation of carbon monoxide. *Surface Science*, v. 316, n. 3, p. 329–336, 1994.

[118] SKORODUMOVA, N. V.; BAUDIN, M.; HERMANSSON, K. Surface properties of CeO2 from first principles. *Physical Review B*, v. 69, n. 7, p. 075401, 2004.

[119] NOLAN, M.; GRIGOLEIT, S.; SAYLE, D. C.; PARKER, S. C.; WATSON, G. W. Density functional theory studies of the structure and electronic structure of pure and defective low index surfaces of ceria. *Surface Science*, v. 576, n. 1-3, p. 217–229, 2005.

[120] SAYAMA, K.; ARAKAWA, H. Photocatalytic decomposition of water and photocatalytic reduction of carbon dioxide over zirconia catalyst. *The Journal of Physical Chemistry*, v. 97, n. 3, p. 531–533, 1993.

[121] LANGFORD, J. I.; WILSON, A. J. C. Scherrer after sixty years: a survey and some new results in the determination of crystallite size. *Journal of Applied Crystallography*, v. 11, n. 2, p. 102–113, 1978.

[122] MOGENSEN, M.; SAMMES, N. M.; TOMPSETT, G. A. Physical, chemical and electrochemical properties of pure and doped ceria. *Solid State Ionics*, Amsterdam, v. 129, n. 1-4, p. 63–94, 2000.

[123] BUNKER, G. Application of the ratio method of EXAFS analysis to disordered systems. *Nuclear Instruments and Methods in Physics Research*, v. 207, n. 3, p. 437–444, 1983.

[124] KOSSOY, A.; FRENKEL, A. I.; FELDMAN, Y.; WACHTEL, E.; MILNER, A.; LUBOMIRSKY, I. The origin of elastic anomalies in thin films of oxygen deficient ceria, CeO2-x. *Solid State Ionics*, Amsterdam, v. 181, n. 33-34, p. 1473–1477, 2010.

[125] CODY, G. D.; TIEDJE, T.; ABELES, B.; BROOKS, B.; GOLDSTEIN, Y. Disorder and the optical-absorption edge of hydrogenated amorphous silicon. *Physical Review Letters*, New York, v. 47, n. 20, p. 1480, 1981.

[126] ANSARI, A. A. Optical and structural properties of sol-gel derived nanostructured CeO2 film. *Journal of Semiconductors*, v. 31, n. 5, p. 053001, 2010.

[127] KAVIYARASU, K.; MANIKANDAN, E.; NURU, Z. Y.; MAAZA, M. Investigation on the structural properties of CeO2 nanofibers via CTAB surfactant. *Materials Letters*, v. 160, p. 61–63, 2015.

[128] YAN, B.; ZHU, H. Controlled synthesis of CeO2 nanoparticles using novel amphiphilic cerium complex precursors. *Journal of Nanoparticle Research*, v. 10, n. 8, p. 1279–1285, 2008.

[129] BESTE, A.; MULLINS, D. R.; OVERBURY, S. H.; HARRISON, R. J. Adsorption and dissociation of methanol on the fully oxidized and partially reduced (111) cerium oxide surface: Dependence on the configuration of the cerium 4f electrons. *Surface Science*, v. 602, n. 1, p. 162–175, 2008.

[130] SKORODUMOVA, N. V.; SIMAK, S. I.; LUNDQVIST, B. I.; ABRIKOSOV, I. A.; JOHANSSON, B. Quantum origin of the oxygen storage capability of ceria. *Physical Review Letters*, Woodbury, v. 89, n. 16, p. 166601, 2002.

[131] PFAU, A.; SCHIERBAUM, K. D. The electronic structure of stoichiometric and reduced CeO2 surfaces: an XPS, UPS and HREELS study. *Surface Science*, v. 321, n. 1-2, p. 71–80, 1994.

[132] KOELLING, D. D.; BORING, A. M.; WOOD, J. H. The electronic structure of CeO2 and PrO2. *Solid State Communications*, Oxford, v. 47, n. 4, p. 227–232, 1983.

[133] WUILLOUD, E.; DELLEY, B.; SCHNEIDER, W.-D.; BAER, Y. Spectroscopic evidence for localized and extended f-symmetry states in CeO2. *Physical Review Letters*, Woodbury, v. 53, n. 2, p. 202–205, 1984.

[134] ALLEN, J. W. Valence fluctuations in narrow band oxides. *Journal of Magnetism and Magnetic Materials*, Amsterdam, v. 47, p. 168–174, 1985.

[135] KONG, M.; LI, Y.; CHEN, X.; TIAN, T.; FANG, P.; ZHENG, F.; ZHAO, X. Tuning the relative concentration ratio of bulk defects to surface defects in TiO2 nanocrystals leads to high photocatalytic efficiency. *Journal of the American Chemical Society*, Washington, v. 133, n. 41, p. 16414–16417, 2011.

[136] SAYLE, T. X. T.; CADDEO, F.; ZHANG, X.; SAKTHIVEL, T.; DAS, S.; SEAL, S.; PTASINSKA, S.; SAYLE, D. C. Structure–activity map of ceria nanoparticles, nanocubes, and mesoporous architectures. *Chemistry of Materials*, v. 28, n. 20, p. 7287–7295, 2016.

[137] JIANG, Y.; ADAMS, J. B.; VAN SCHILFGAARDE, M. Density-functional calculation of CeO2 surfaces and prediction of effects of oxygen partial pressure and temperature on stabilities. *The Journal of Chemical Physics*, v. 123, n. 6, p. 064701, 2005.

[138] CHEN, H.-T.; CHOI, Y. M.; LIU, M.; LIN, M. C. A theoretical study of surface reduction mechanisms of CeO2 (111) and (110) by H2. *Chem Phys Chem*, v. 8, n. 6, p. 849–855, 2007.